RTTOV-13

SCIENCE AND VALIDATION REPORT

Roger Saunders[1], James Hocking[1], Emma Turner[1], Stephan Havemann[1], Alan Geer[2], Cristina Lupu[2], Jerôme Vidot[3], Philippe Chambon[3], Christina Köpken-Watts[4], Leonhard Scheck[4], Olaf Stiller[4], Christina Stumpf[4], Eva Borbas[5]

Affiliations:

[1]Met Office, U.K.

[2]European Centre for Medium Range Weather Forecasts

[3]MétéoFrance

[4]Deutscher Wetterdienst

[5]University of Wisconsin

This documentation was developed within the context of the EUMETSAT Satellite Application Facility on Numerical Weather Prediction (NWP SAF), under the Cooperation Agreement dated 7 December, 2016, between EUMETSAT and the Met Office, UK, by one or more partners within the NWP SAF. The partners in the NWP SAF are the Met Office, ECMWF, DWD and Météo France.

Change record			
Version	Date	Author / changed by	Remarks
1.0	12/11/2020	R W Saunders	Version 1.0 released to users

Table of contents

1. Introduction

The purpose of this report is to document the scientific aspects of the latest version of the NWP SAF fast radiative transfer model, referred to hereafter as RTTOV v13, which are different from the previous model RTTOV v12 and present the results of the validation tests comparing the two versions of RTTOV which have been carried out. The enhancements to this version, released in November 2020, have been made under the auspices of the EUMETSAT NWP-SAF.

The RTTOV-13 software is available at no charge to users on request from the NWP SAF web site. Note the licence agreement first has to be completed on the web site here. RTTOV v13 documentation, including the latest version of this document can be viewed on the NWP SAF web site at: https://nwp-saf.eumetsat.int/site/software/rttov/documentation/ which may be updated from time to time. Technical documentation about the software and how to run it can be found in the RTTOV v13 user's guide which can also be downloaded from the link above and is provided as part of the distribution file to users.

The baseline document for the original version of RTTOV is available from ECWMF as Eyre (1991) and the basis of the original model is described in Eyre and Woolf (1988). This was updated for RTTOV v5 (Saunders *et. al.* 1999a, Saunders *et. al.,* 1999b) and for RTTOV v6, RTTOV v7, RTTOV v8, RTTOV v9 (Matricardi *et. al.,* 2004), RTTOV v10 and RTTOV v11 with the respective science and validation reports for each version hereafter referred to as R7REP2002, R8REP2006, R9REP2008, R10REP2010, R11REP2013 and R12REP2017 respectively some are available from the NWP SAF web site at the link above and the links to the individual reports are given in the references section of this report. A more recent peer review paper giving an overview of RTTOV is in Saunders *et. al.* (2018) to which new users of RTTOV are referred to. The changes described here only relate to the scientific differences from RTTOV v12. A complete list of scientific and technical differences between RTTOV v12 and v13 is given in the RTTOV v13 user guide.

This document also describes comparisons and validations of the output values from this new version of the model by comparing with previous versions, other models and observations. In general only aspects related to new and improved science are presented in this report but some results are presented of the overall performance of the new RTTOV package. Many of the details of the new science are given in other papers/reports which are referenced in this document and so only a summary is presented here in order to keep this document manageable in size. Section 2 describes the new datasets used for validation of RTTOV, section 3 the individual scientific changes made in RTTOV v13 and the changes they make to the simulations. Section 4 describes the overall performance of the new model for a limited number of satellite instruments. Section 5 gives a brief summary.

2. Use of new profile datasets for validation

Since RTTOV v11, satellite instrument coefficients have been specified on 54 levels (101 for hyperspectral IR instruments). A training set of 83 atmospheric profiles covering a diverse range of global atmospheric conditions (Matricardi, 2008) were selected from a large database of profiles on 91 levels generated by the experimental suite (cycle 30R2) of the ECMWF forecasting system, as described in Chevallier et al. (2006). The 81st, 82nd and 83rd profiles are the minimum, maximum and mean, respectively, of the initial database. The profiles were interpolated to 54 fixed pressures between 0.005 and 1050 hPa using a formula to optimise placement of the levels resulting in smoothly varying Jacobians (Strow et al. 2003, Equation 19). For RTTOV v12, the 83 profiles of CO_2, CH_4 and N_2O were improved to cover the 1970-2020 period (see R12REP2017).

Validation of the accuracy of the RTTOV coefficients against the underlying line-by-line models is typically performed using the same 83 diverse profiles used to calculate the coefficients (see on the NWPSAF website the dedicated webpage, i.e. https://nwp-saf.eumetsat.int/site/software/rttov/download/coefficients/comparison-with-lbl-simulations/ for all instruments supported by RTTOV). However, recent studies have employed a much larger dataset of 25,000 profiles to independently verify results for certain instruments (see https://nwp-saf.eumetsat.int/site/software/atmospheric-profile-data/). Barbosa-Silveira *et al.* (2020) presents the validation for some historic instruments: IRIS-D, SIRS-B, MRIR, HRIS, MSU, SSM/T-2, SSM/I, SMMR and SSMI/S, and Hocking *et al.* (2021) includes the results for ATMS and IASI presented here. The dataset, described in Eresmaa and McNally (2014), is a selection from the short-range forecasting of the IFS outputs over one year and comprises five subsets of 5,000, each one selected to contain maximum diversity of either: temperature (t), specific humidity (q), ozone (o3), cloud condensate (ccol) and precipitation (rcol). The vertical resolution was originally on 137 levels but has been interpolated to the corresponding 54 (101) levels in order to compare with the RTTOV coefficient being tested. Only the temperature (Figure 2.1), water vapour (Figure 2.2), and ozone (Figure 2.3) profiles plotted below were used in the evaluations described above.

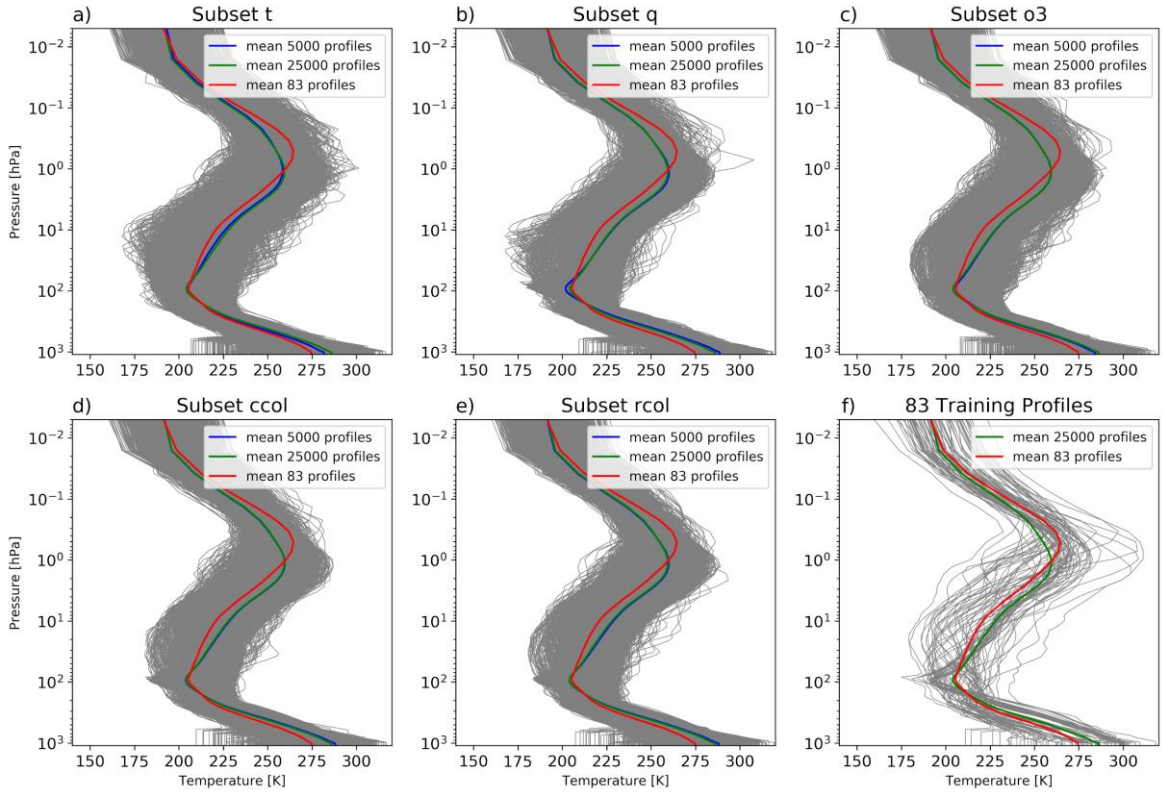

Figure 2.1: a)-e) 25,000 profiles of temperature in five subsets of 5,000. Each subset displays maximum variability of each of the variables; t, q, o3, cool and rcol. f) temperature profiles for the 83 diverse profile set used to create RTTOV coefficients. The mean profile is shown for each subset of 5,000 (blue line), all 25,000 profiles (green line) and the 83 profile set (red line).

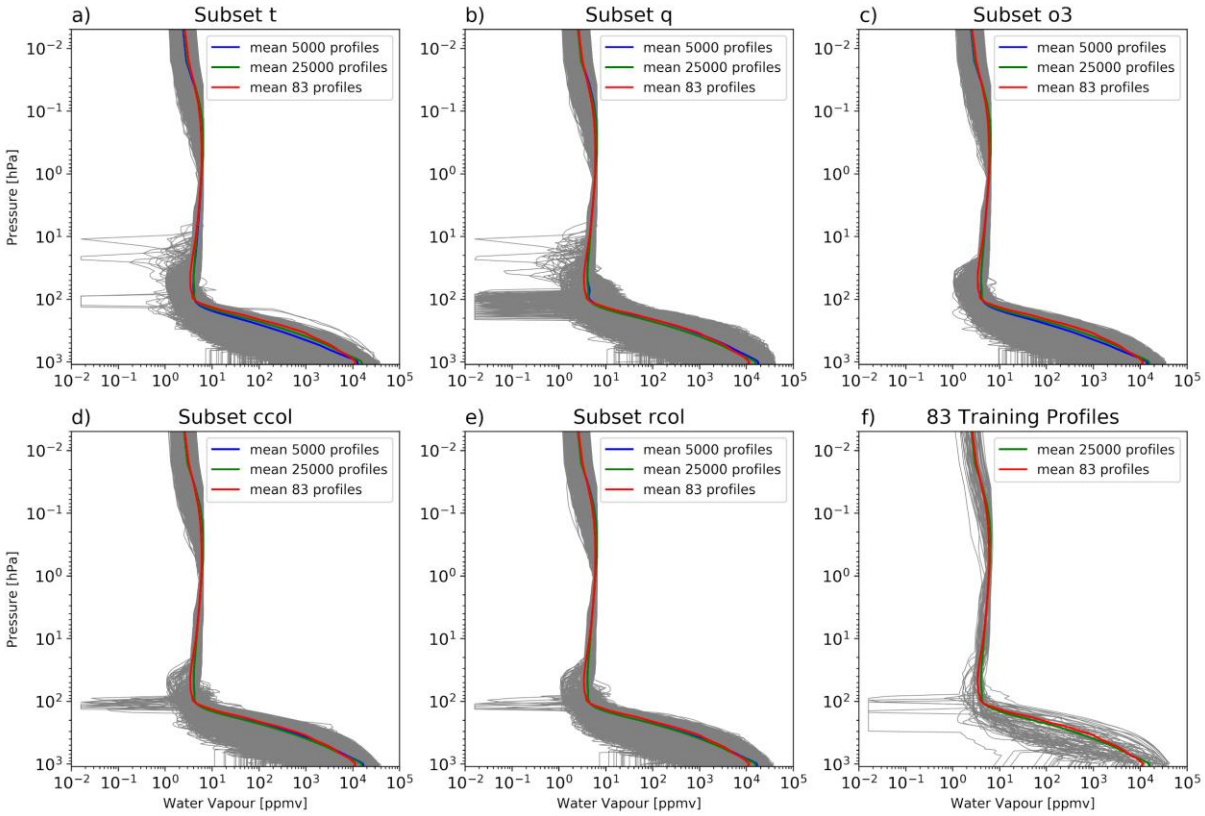

Figure 2.2: Same as Figure 2.1 but showing water vapour profiles.

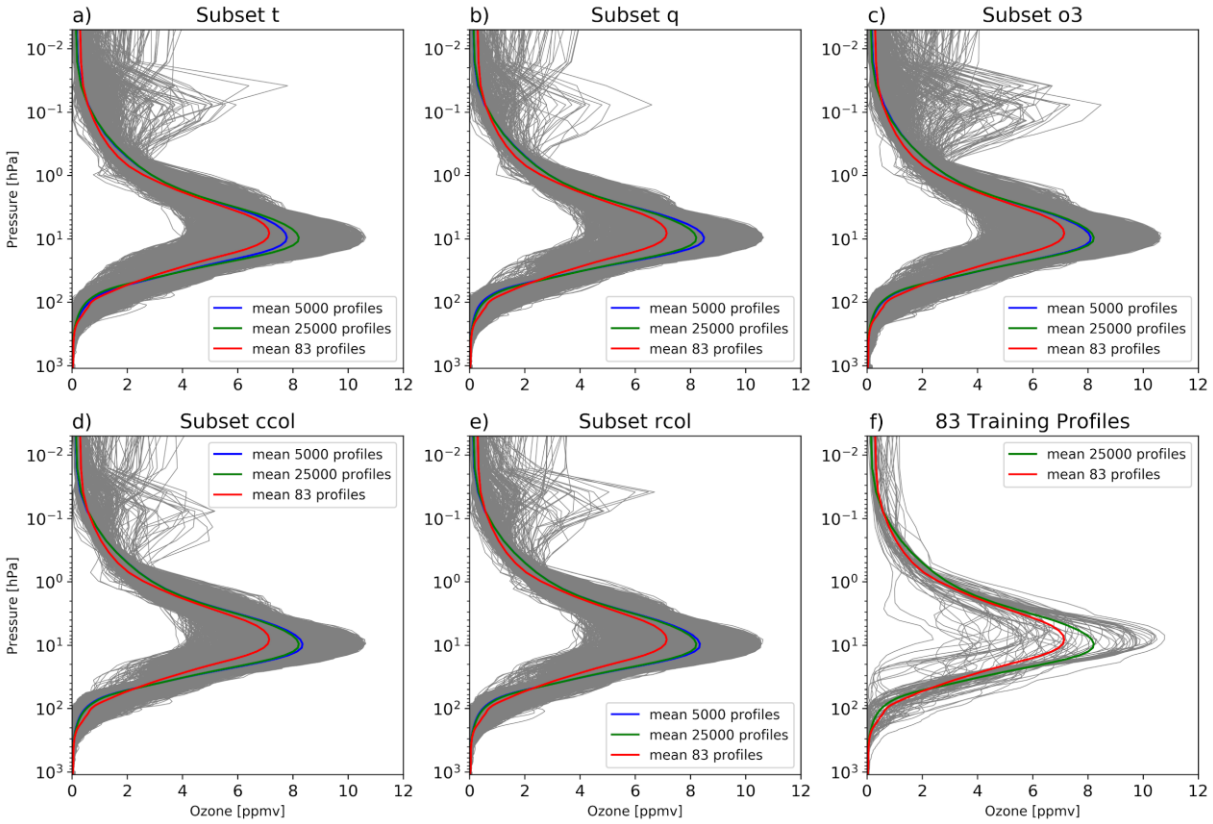

Figure 2.3: Same as Figure 2.1 but showing ozone profiles.

3. Scientific Changes from RTTOV v12 to RTTOV v13

The main scientific changes from RTTOV v12 to RTTOV v13 are listed here:

- Improvements to infrared line-by-line models and associated spectroscopic datasets from which the RTTOV coefficients are computed
- New predictors of layer optical depth allowing more accurate simulations and easier addition of new gases
- Extension of spectrum to cover far infrared and higher frequency microwave to support new instruments such as ICI and FORUM
- Improved treatment of cloud absorption for microwave radiance simulations
- Improved treatment of scattering from water, ice clouds and aerosols in visible and infrared radiances

- New infrared surface emissivity atlas
- Improved treatment of scattering from surfaces
- Updates to MFASIS visible cloud scattering parameterisation
- Improved treatment of Rayleigh scattering
- Updates to simulations of principal components (HT-FRTC & PC-RTTOV)
- Updated version of RTTOV-SCATT

Each sub-section below gives more details on each of these components and references as required for the full details.

3.1 Updates to Line by Line Models

3.1.1 Infrared line-by-line models

The LBLRTM model used for generating the visible to infrared RTTOV v13 coefficients was updated to the version LBLRTM v12.8 (see http://rtweb.aer.com/lblrtm_whats_new.html) whereas RTTOV v12 used LBLRTM v12.2. This implied two major changes in the underlying spectroscopy, (1) the AER spectral database v3.5 based on updated HITRAN2012 (instead of HITRAN2008) and (2) the continuum MT-CKD 3.2 (instead of MT-CKD 2.5.2). The AER v3.5 updated the CO_2 line coupling and HITRAN2012 updated line parameters of many molecules (such as H_2O, CH_4, CO_2, etc..). Figure 3.1.1 shows the IR LBL transmittance difference between LBLRTM v12.8 and v12.2 at $\Delta\nu$=0.001 cm^{-1} between 175 and 3300 cm^{-1}. The different colour lines correspond to 3 pressure levels used for the calculation of the transmittance from considered top of atmosphere (0.005 hPa) to level. In Figure 3.1.1(A) is showing the difference for all molecules including the line absorption and continuum. Most of the differences are explained by the water vapour line parameters update (see Fig. 3.1.1(B)).

No changes were found for ozone (Fig. 3.1.1(C)) whereas the water vapour continuum was updated in the FIR and above 1800 cm^{-1}. It should be noted that RTTOV v12 can also use coefficient files generated with LBLRTM v12.8.

For the visible and near infrared spectral region Figure 3.1.2 shows the transmittance differences from 1013 hPa to space for all the gases, only the mixed gases and the water vapour continuum. Both the water vapour lines and continuum are the main source of the differences due to updates in the spectroscopy in HITRAN2012 and the new continuum model MT-CKD 3.2.

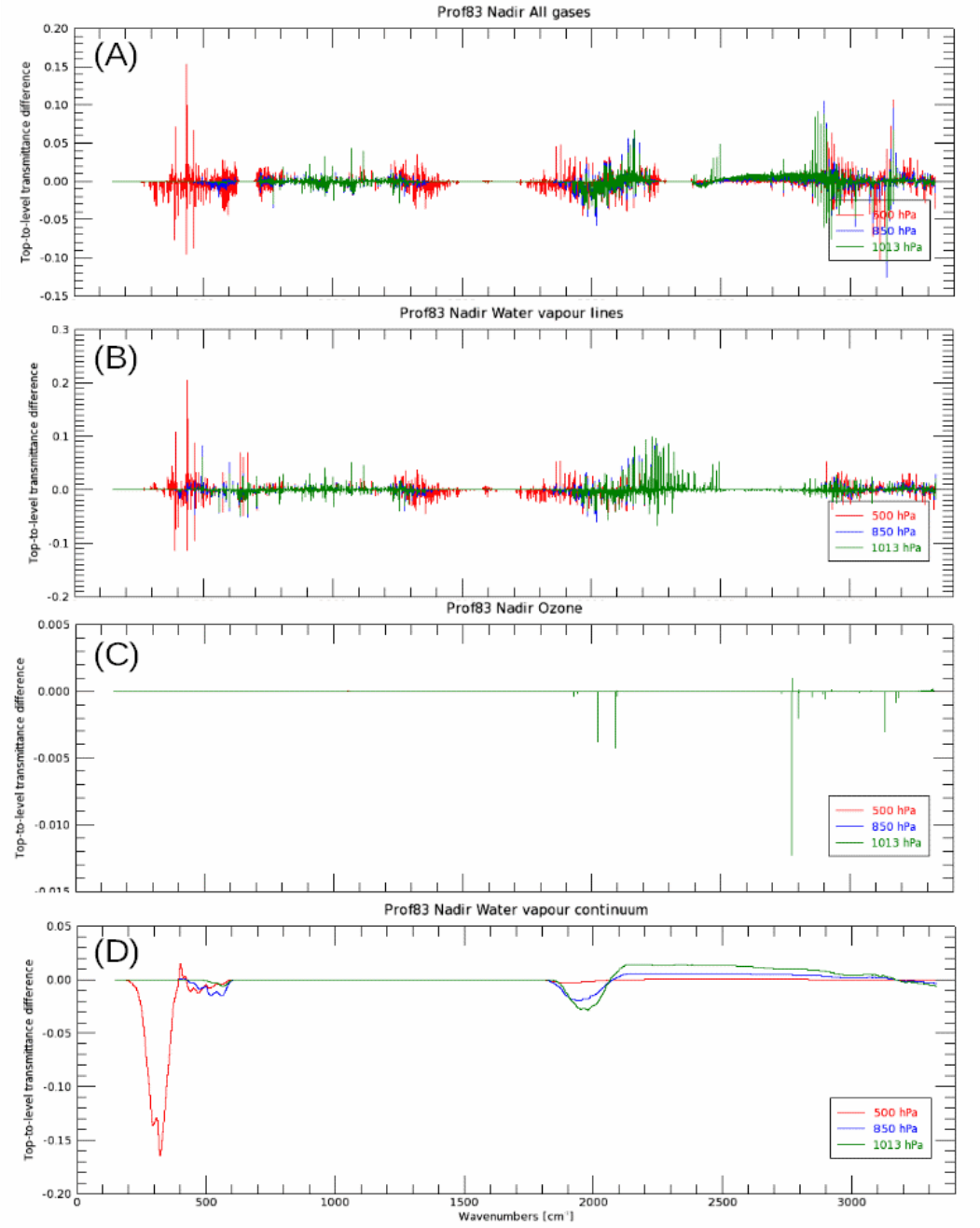

Figure 3.1.1: Top-to-level infrared transmittances difference for RTTOV profile 83 between LBLRTM v12.8 and v12.2, at level 500, 850, and 1013 hPa: (A) for all molecules, (B) for water vapour lines,(C) for Ozone, (D) for water vapour continuum.

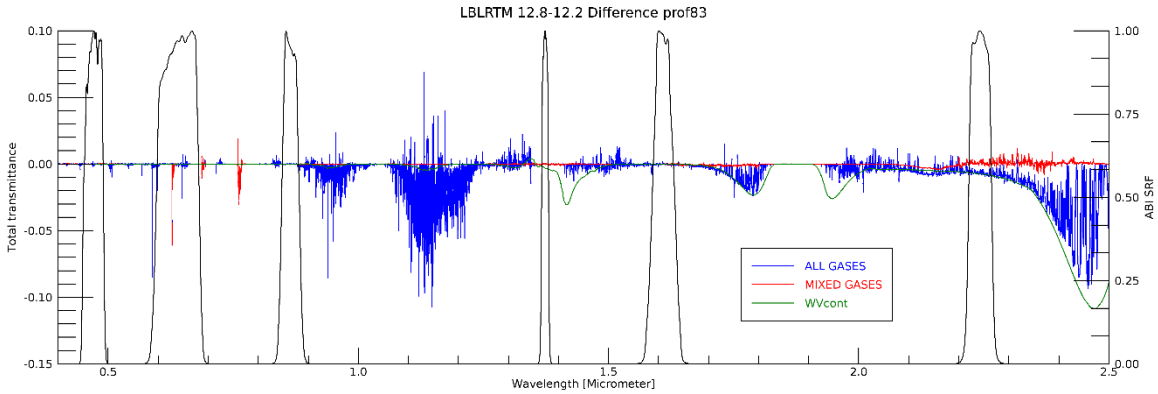

Figure 3.1.2 Visible and near-infrared transmittance differences for profile 83 between LBLRTM v12.8 and v12.2, at level 1013 hPa for all gases, for mixed gases, and for water vapour continuum. The ABI channel spectral response functions are also plotted (see y-axis right for scale).

3.1.2 Microwave line-by-line models and use of improved SRFs

The microwave spectroscopy used in the AMUSTRAN line-by-line code is a modified version of MPM89 (Liebe 1989) and has not altered since the release of RTTOV v12. The full configuration is documented in Turner *et al.* (2019a). An exception to the standard configuration is implemented in the most recent Ice Cloud Imager (ICI) coefficients, which include updated water vapour and ozone spectroscopy based on a review of the most up-to-date research (Turner and Saunders, 2019b). The spectroscopy has been updated to reflect ICI's unique spectral coverage, which extends beyond the 200 GHz maximum frequency of most MW instruments into the sub-millimetre up to 664 GHz, where the atmosphere is far more opaque. Ozone has also been made independently variable rather than including it in the fixed gases like other MW coefficients, due to its increased influence at higher frequencies.

Currently all standard RTTOV MW coefficients provided are calculated using a top hat (boxcar) spectral response function (SRF), i.e. all frequencies within a channel's bandwidth are assumed to have equal influence, which is often not the case in reality. Although real MW instrument spectral response functions are routinely measured, they have historically not been easy to obtain to incorporate into the line-by-line calculation and subsequent RTTOV coefficients. However, in recent years demand for MW SRFs by the community has increased, as their omission can be a source of error of several tenths of a degree depending on how much the real 'shape' of the channel deviates from the assumed top hat (Duncan *et al.* 2019). There is also the added risk of RFI in exposed frequencies that measure outside of protected bands.

A limited number of RTTOV MW coefficients are now available that incorporate the real SRF measured pre-launch. These include ATMS on Suomi-NPP (JPSS-0) and NOAA-20, GMI on GPM, AMSU-A on NOAA-19, MHS on NOAA-18, NOAA-19, MetOp-A, MetOp-B and

MetOp-C, and the TEMPEST-D cubesat. A schematic of how SRF data is applied to a channel is shown in Figure 3.1.3.

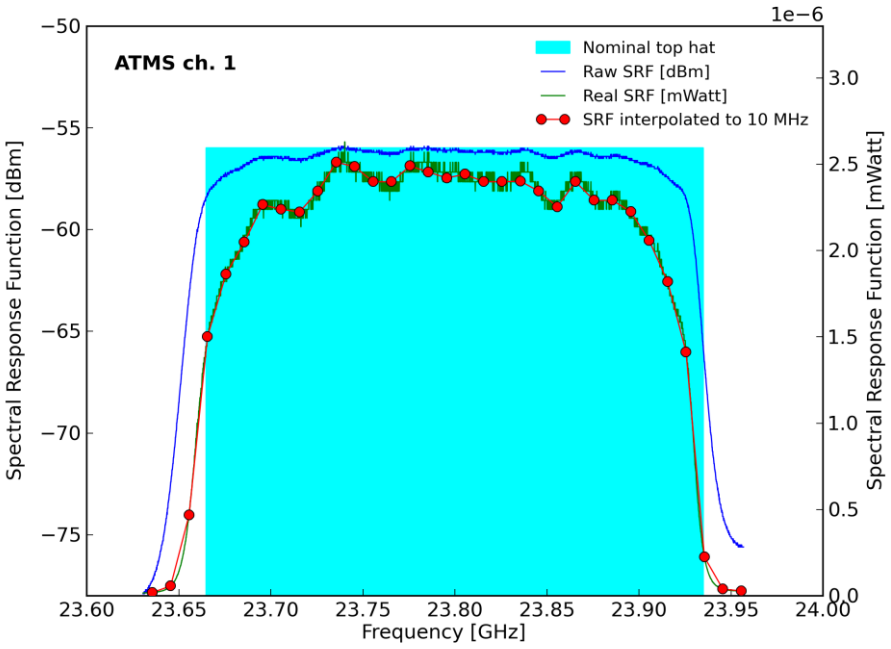

Figure 3.1.3. Schematic of processed SRF (green line), raw un-processed SRF (blue line) and nominal top hat function (shaded cyan) for channel 1 of the ATMS instrument on NOAA-20. The SRF is interpolated to 10 MHz (red dots) which is the pre-determined spectral resolution required for this channel. Original SRF data is from NOAA GSFC (source Ed Kim).

The SRF is first processed by applying a cut-off to either side of each channel by manual inspection, which eliminates the noise floor. It is then interpolated to the optimum spectral resolution which has already been pre-specified for the channel. Most SRFs are measured in decibels (dB) which needs to be converted ahead of the calculation. Finally, the original transmittance is weighted by the spectral response at each frequency and normalised by its sum to give the averaged transmittance for the channel as:

$$\overline{\tau_{ch}} = \frac{\sum_\nu \tau_\nu R_\nu}{\sum_\nu R_\nu}$$

where τ is the transmittance and R is the SRF at frequency ν.

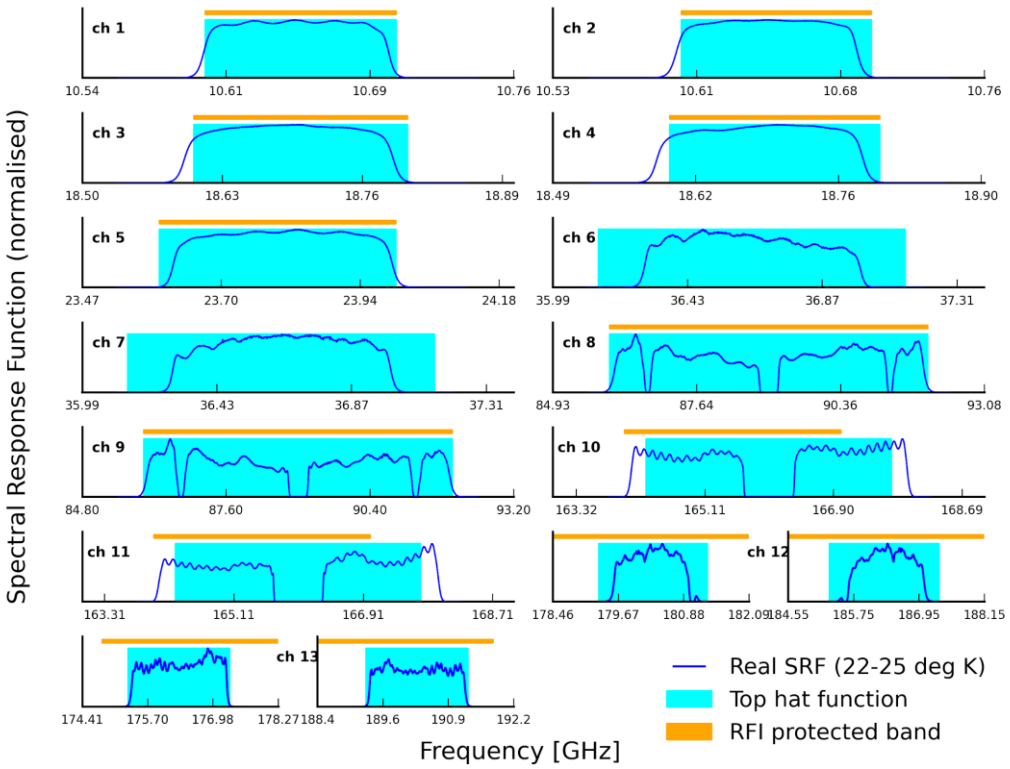

Figure 3.1.4. Measured normalised spectral response functions for GMI (blue) (source is GMI calibration handbook) compared with the nominal top hat function (cyan). Spectral coverage of current RFI protected bands (orange) are also shown.

Figure 3.1.4 shows an example of real SRFs compared with the top hat functions specified by the nominal channel central frequencies and bandwidth for the GMI instrument on GPM. Though there appear to be significant differences for some of the channels the effect on simulated brightness temperatures depends primarily on the features of the spectral region. In practice it is only channels 10-12 that are affected by up to 0.25 (±0.13) K, due to the influence of the 183.31 GHz water vapour line (Figure 3.1.5).

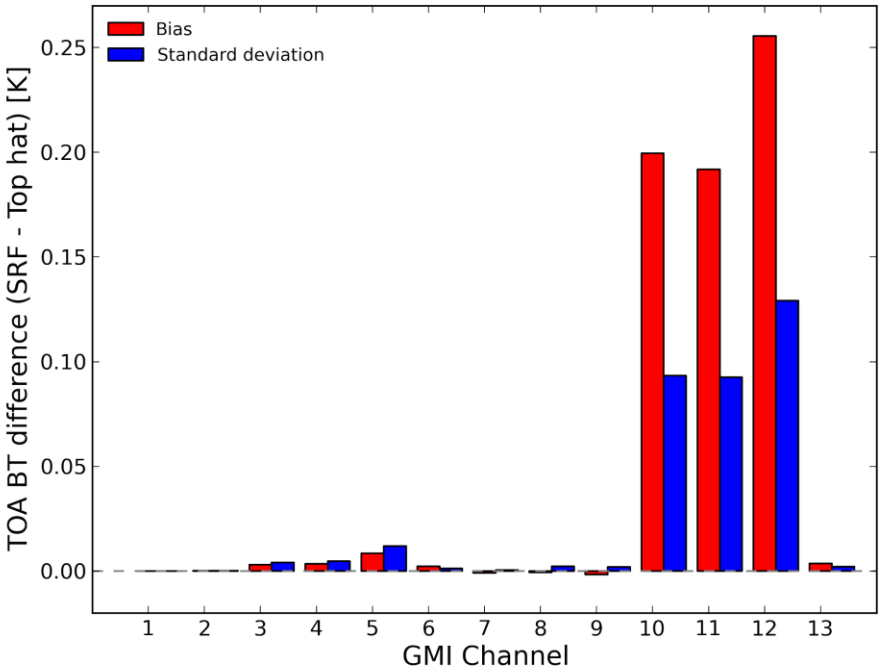

Figure 3.1.5. Mean and standard deviation of the difference between measured and top hat spectral response functions for all GMI channels over the 83 diverse profiles dataset. TOA brightness temperatures are calculated by AMSUTRAN. The satellite zenith angle is set to 53 degrees to match the fixed geometry of the conical scanner of the instrument.

3.2 New optical depth parameterisation

3.2.1 Implementation

The current optical depth parameterisation in RTTOV is based on the methods in McMillin and Fleming (1976) and Eyre and Woolf (1988) and is described in Saunders *et al.* (2018). A linear regression is used to predict layer absorption optical depths due to different gases in the atmosphere. The parameterisation predicts optical depths due to water vapour, optionally other variable gases (see below), and finally due to “mixed gases” which comprises climatological concentrations of all other radiatively significant atmospheric constituents. Any gases included among the mixed gases cannot subsequently be varied in the RTTOV simulations. The independent variables, or predictors, are quantities derived from the input atmospheric profile variables: pressure, temperature, gas concentrations, and the local zenith angle of the radiation path.

Three sets of predictors are implemented, named after the RTTOV versions in which they were introduced. The "v7 predictors" (Saunders *et al.*, 1999) predict infrared and microwave

optical depths due to mixed gases, water vapour and optionally O_3. They were designed primarily for satellites in low Earth orbit (LEO) and as such support training for satellite zenith angles up to about 64° (the training is done for 6 evenly spaced secants from 1 to 2.25). The v8 predictors (R8REP2006) employed separate regressions for water vapour lines and water vapour continuum and added CO_2 as an optional variable gas. The v9 predictors (Matricardi, 2008) added N_2O, CO and CH_4 (and later, in RTTOV v12, SO_2) as optional variable gases, and for short-wave IR channels they were designed to support training for zenith angles up to 85° (the training is done for 14 zenith angles, up to a maximum secant of 12) in order to support solar radiation. In RTTOV v11, the v9 predictors were applied to the simulation of visible channels, and for geostationary (GEO) sensors the training was extended to the full 14 secants for all channels.

RTTOV is trained using accurate line-by-line (LBL) radiative transfer models which are used to generate transmittances at high spectral resolution for a set of training profiles. In the visible and infrared, LBLRTM is used (see Section 3.1.1), while in the microwave the AMSUTRAN model is used (see Section 3.1.2). The parameterisation is computed on a set of layers bounded by a fixed set of pressure levels. Coefficients for most sensors are available on a set of 54 pressure levels, while additional coefficients on 101 levels are available for hyperspectral IR sounders.

It is important to note that the predicted optical depths are “polychromatic” in that they are for satellite channels of finite spectral width. These are computed by integrating the high spectral resolution LBL transmittances over the channel spectral responses. This means that summing the individual optical depths due to each gas may not yield the total layer optical depth due to all gases combined. To address this, the parameterisation follows McMillin *et al.* (1995) by predicting “effective” optical depths which are obtained from ratios of channel-integrated transmittances as illustrated in equation 3.2.1 for the case of variable water vapour and ozone.

$$\tau_j^{total} = \tau_j^{mixed} \cdot \frac{\tau_j^{mixed+wv}}{\tau_j^{mixed}} \cdot \frac{\tau_j^{mixed+wv+o3}}{\tau_j^{mixed+wv}} \text{, for } j = 1, n \qquad (3.2.1)$$

where j is the level number, n is the number of levels (typically 54 or 101 as noted above), and τ_j is the channel-integrated transmittance from space to level j. Effective optical depths computed from the transmittance ratios on the right-hand side of equation 3.2.1 are predicted by the parameterisation so that after summing the predicted optical depths due to each gas, τ_j^{total} (which is identical to $\tau_j^{mixed+wv+o3}$) is obtained as required.

There are some disadvantages to this effective optical depth approach. It is sensitive to the order of the gases in the sequence of ratios which means it may be necessary to change this order on a per-channel basis. It is necessary to take steps to handle numerical issues

caused by very small transmittances in the denominators. Finally, adding new variable gases can be a difficult process as it may require cross-gas predictors (e.g. predictors involving the concentration of one gas may be required when calculating the effective optical depth for another gas) and, ultimately, there is a practical limit to the number of variable gases this approach can support.

It is desirable to rationalise the three sets of predictors into a single predictor set that satisfies the following requirements:

- Can be trained over the full range of zenith angles supported by RTTOV (i.e. up to 85°) for all wavelengths to fully support GEO sensors and solar-affected channels.
- Support for any combination of trace gases (in principle).
- Makes it easier to introduce new variable gases compared to the current predictors.

RTTOV v13 introduces a new optical depth parameterisation following McMillin *et al.* (2006). In this formulation, the channel-integrated layer optical depths are predicted for mixed gases and for each variable gas independently. The error due to summing polychromatic optical depths is accounted for by an additional correction term. The transmittance calculation for the case of variable water vapour and ozone is illustrated in equation 3.2.2.

$$\tau_j^{total} = \tau_j^{mixed} \cdot \tau_j^{wv} \cdot \tau_j^{o3} \cdot \tau_j^{c}, \text{for } j = 1, n \qquad (3.2.2)$$

where τ_j^c is the correction term. Since the transmittances for each gas are predicted separately, they are independent and as such there are no cross-gas predictors (as described above). The predictors used for the correction term for a given channel depend upon the gases which contribute to the optical depth in that particular layer. For most gases, if any channel-integrated gas layer optical depth among the training profile set exceeds 0.005 then predictors for that gas are included in the correction term. With variable CH_4 the forward model radiances and the methane Jacobians were improved by only including the CH_4 predictors in the correction term if any optical depth on any level among the training profile set exceeds 0.01. The mixed gas correction term predictors are always included in the correction term. The application of these optical depth thresholds not only brings performance benefits (excluding calculations for gases which have no impact), but more importantly significantly reduces the occurrence of spurious sensitivities to particular gases in the Jacobians. In this way the number of predictors for the correction term with non-zero coefficients varies layer-by-layer and channel-by-channel.

In the training the correction term is calculated as shown in equation 3.2.3.

$$\tau_j^c = \frac{\tau_j^{total}}{\hat{\tau}_j^{mixed} \hat{\tau}_j^{wv} \hat{\tau}_j^{o3}}, \text{for } j = 1, n \qquad (3.2.3)$$

where $\hat{t}_j$ is the parameterised transmittance. By using the parameterised transmittances rather than the channel-integrated LBL transmittances, the correction term also mitigates errors in the individual gas optical depth regressions.

This parameterisation uses a new set of predictors (referred to as "v13 predictors") which were derived from the v9 predictors through a combination of stepwise regression and trial and error. The new predictors are given in full in Tables 3.2.1 to 3.2.4.

The training profiles and fixed pressure levels remain the same as for the existing parameterisation. An Ordinary Least Squares linear regression is carried out both for the individual gas optical depths and then for the correction term. In the regression, training optical depths are omitted for layers where the transmittance due to the gas in question from space down to the layer is less than 3×10^{-6} (i.e. where the layer is invisible to the satellite due to absorption by the intervening atmosphere). In order to reduce the influence of layers among the training profiles that are optically deep in the atmosphere and hence have limited impact on the top of atmosphere radiance, all predictor values and training optical depths input to the regression are weighted by the square root of the product of the transmittances from space to the levels bounding the layer. Finally, where any individual predicted gas layer optical depth is less than zero, it is set to zero before the correction term regression is computed. Similarly, where the total layer optical depth (including the correction term) is less than zero, this is also set to zero.

$p_{\delta p}(l) = p(l+1)(p(l+1) - p(l))$	$p_{\delta p}(0) = p(1)(p(2) - p(1))$	
$T(l) = \frac{1}{2}(T^{\text{prof}}(l) + T^{\text{prof}}(l+1))$	$T^*(l) = \frac{1}{2}(T^{\text{ref}}(l) + T^{\text{ref}}(l+1))$	$\delta T(l) = T(l) - T^*(l)$
$G(l) = \frac{1}{2}(G^{\text{prof}}(l) + G^{\text{prof}}(l+1))$	$G^*(l) = \frac{1}{2}(G^{\text{ref}}(l) + G^{\text{ref}}(l+1))$	
$T_r(l) = T(l)/T^*(l)$	$T_w(l) = \frac{\sum_{i=1}^{l} p_{\delta p}(l-1)T(l)}{\sum_{i=1}^{l} p_{\delta p}(l-1)T^*(l)}$	
$G_r(l) = G(l)/G^*(l)$	$G_w(l) = \frac{\sum_{i=1}^{l} p_{\delta p}(l-1)G(l)}{\sum_{i=1}^{l} p_{\delta p}(l-1)G^*(l)}$	$G_{wt}(l) = \frac{\sum_{i=1}^{l} p_{\delta p}(l-1)T(l)G(l)}{\sum_{i=1}^{l} p_{\delta p}(l-1)T^*(l)G^*(l)}$

All quantities defined in the table above are on layers (aside from $p_{\delta p}(0)$).

$p(l)$ is the pressure (hPa) at level l. These are usually the pre-specified pressures of the 54 or 101 levels used for RTTOV coefficients.

$T^{\text{prof}}(l)$ is the temperature (K) at level l of the input profile.

$T^{\text{ref}}(l)$ is the temperature (K) at level l of the reference profile which is the mean over the training profile set.

$G \in \{W, O3, CO2, N2O, CO, CH4, SO2\}$ represents gas concentration (ppmv over dry air).

$G^{\text{prof}}(l)$ are the gas concentrations at level l of the input profile.

$G^{\text{ref}}(l)$ are the gas concentrations at level l of the reference profile which is the mean over the training profile set.

Table 3.2.1: quantities used in the v13 predictor calculations listed in tables 3.2.2 - 3.2.4

Predictor	Mixed gases	H_2O lines	H_2O continuum
1	$\sec(\theta)$	$(\sec(\theta)W_r)^2$	$\sec(\theta)W_r^2/T_r$
2	$\sec^2(\theta)$	$\sec(\theta)W_w$	$\sec(\theta)W_r/T_r$
3	$\sec(\theta)T_r$	$(\sec(\theta)W_w)^2$	$\sec(\theta)W_r^2/T_r^4$
4	$\sec(\theta)T_r^2$	$\sec(\theta)W_r\delta T$	$\sec(\theta)W_r/T_r^2$
5	T_r	$\sqrt{\sec(\theta)W_r}$	-
6	T_r^2	$\sqrt[4]{\sec(\theta)W_r}$	-
7	$\sec(\theta)T_w$	$\sec(\theta)W_r$	-
8	$\sec(\theta)T_r^3$	$(\sec(\theta)W_w)^{1.5}$	-
9	$\sec(\theta)\sqrt{\sec(\theta)T_r}$	$(\sec(\theta)W_r)^{1.5}$	-
10	1	$(\sec(\theta)W_r)^{1.5}\delta T$	-
11	-	$\sqrt{\sec(\theta)W_r}\delta T$	-
12	-	$(\sec(\theta)W_w)^{1.25}$	-
13	-	$\sec(\theta)W_r^2/W_w$	-
14	-	$\sqrt{\sec(\theta)W_r}W_r/W_{wt}$	-
15	-	$\sec(\theta)\sqrt{W_w}$	-
Optical depth	1-9	1-13 / 1-14*	1-4
Correction term	2, 3, 4, 10	2, 4, 5, 6, 15	-†

* 1-13 for $\nu <= 1095cm^{-1}$ or $2320 < \nu <= 2570cm^{-1}$, otherwise 1-14, where ν is the channel central wavenumber

† No correction term predictors for H_2O continuum.

Table 3.2.2: Mixed gas and water vapour predictors and predictor lists for optical depth and correction term in the new parameterisation. θ is the zenith angle.

Predictor	O_3	CO_2	N_2O
1	$\sec(\theta)O3_r$	$\sec(\theta)CO2_r$	$\sec(\theta)N2O_r$
2	$\sqrt{\sec(\theta)O3_r}$	T_r^2	$\sqrt{\sec(\theta)N2O_r}$
3	$\sec(\theta)O3_r\delta T$	$\sec(\theta)T_r$	$\sec(\theta)N2O_r\delta T$
4	$\sec(\theta)O3_r/O3_w$	$\sec(\theta)T_r^2$	$(\sec(\theta)N2O_r)^2$
5	$(\sec(\theta)O3_r)^2$	T_r	$N2O_r\delta T$
6	$\sec(\theta)O3_r^2O3_w$	$\sec(\theta)T_w$	$\sqrt[4]{\sec(\theta)N2O_r}$
7	$\sqrt{\sec(\theta)O3_r}O3_r/O3_w$	$(\sec(\theta)CO2_w)^2$	$\sec(\theta)N2O_w$
8	$\sec(\theta)O3_rO3_w$	$\sec(\theta)T_w\sqrt{T_r}$	$\sec(\theta)N2O_{wt}$
9	$(\sec(\theta)O3_w)^{1.75}$	$\sqrt{\sec(\theta)CO2_r}$	$\sqrt{\sec(\theta)N2O_r}N2O_r/N2O_w$
10	$\sec(\theta)O3_r\sqrt{\sec(\theta)O3_w}$	T_r^3	$(\sec(\theta)N2O_{wt})^2$
11	$(\sec(\theta)O3_w)^2$	$\sec(\theta)T_r^3$	$(\sec(\theta)N2O_{wt})^3$
12	$\sqrt{\sec(\theta)}O3_w^2\delta T$	$\sqrt{\sec(\theta)}T_r^2T_w^3$	$\sec^2(\theta)N2O_{wt}\delta T$
13	$\sec(\theta)O3_w$	$T_r^2T_w^2$	-
14	-	$\sec(\theta)CO2_w$	-
Optical depth	1-12	1-13	1-12
Correction term	13	14, 8, 9	7, 8, 10, 11, 12

Table 3.2.3: O_3, CO_2 and N_2O predictors and predictor lists for optical depth and correction term in the new parameterisation. θ is the zenith angle.

Predictor	CO	CH_4	SO_2
1	$\sec(\theta)CO_r$	$\sec(\theta)CH4_r$	$(\sec(\theta)SO2_r)^2$
2	$\sqrt{\sec(\theta)CO_r}$	$\sqrt{\sec(\theta)CH4_r}$	$\sec(\theta)SO2_w$
3	$\sec(\theta)CO_r\delta T$	$\sec(\theta)CH4_r\delta T$	$(\sec(\theta)SO2_w)^2$
4	$(\sec(\theta)CO_r)^2$	$(\sec(\theta)CH4_r)^2$	$\sec(\theta)SO2_r\delta T$
5	$\sqrt{\sec(\theta)CO_r}\delta T$	$CH4_r\delta T$	$\sqrt{\sec(\theta)SO2_r}$
6	$\sqrt[4]{\sec(\theta)CO_r}$	$\sqrt[4]{\sec(\theta)CH4_r}$	$\sqrt[4]{\sec(\theta)SO2_r}$
7	$\sec(\theta)CO_r\delta T\lvert\delta T\rvert$	$\sec(\theta)CH4_{wt}$	$\sec(\theta)SO2_r$
8	$\sec(\theta)CO_r^2/CO_w$	$CH4_{wt}$	$\sqrt{\sec(\theta)SO2_r}SO2_r/SO2_{wt}$
9	$\sqrt{\sec(\theta)CO_r}CO_r/CO_w$	$(\sec(\theta)CH4_w)^2$	$(\sec(\theta)SO2_w)^{1.5}$
10	$\sec(\theta)CO_r^2/\sqrt{CO_w}$	$\sec(\theta)CH4_w$	$(\sec(\theta)SO2_r)^{1.5}$
11	$(\sec(\theta)CO_w)^{0.4}$	$\sqrt{\sec(\theta)CH4_r}CH4_r/CH4_w$	$(\sec(\theta)SO2_r)^{1.5}\delta T$
12	$\sqrt[4]{\sec(\theta)CO_{wt}}$	$(\sec(\theta)CH4_w)^{1.25}$	$\sqrt{\sec(\theta)SO2_r}\delta T$
13	$\sec^2(\theta)CO_rCO_w$	-	$(\sec(\theta)SO2_w)^{1.25}$
14	$\sec(\theta)CO_w$	-	$\sec(\theta)SO2_r^2/SO2_w$
15	$\sec(\theta)CO_{wt}$	-	$\sec(\theta)\sqrt{SO2_w}$
16	$(\sec(\theta)CO_w)^2$	-	-
Optical depth	1-13	1-11	1-14
Correction term	12, 14, 15, 16	7, 9, 10, 12	2, 4, 5, 6, 15

Table 3.2.4: CO, CH_4 and SO_2 predictors and predictor lists for optical depth and correction term in the new parameterisation. θ is the zenith angle.

3.2.2 Validation

Figure 3.2.1 shows mean and standard deviation of differences between RTTOV ATMS brightness temperatures and brightness temperatures computed from the channel-integrated line-by-line transmittances for 25,000 diverse independent profiles and over the 6 secants used for training RTTOV coefficients. The surface emissivity is set to 1. The plot compares differences for the existing v7 predictors and the new v13 predictors. Generally, the new predictors perform as well as the v7 predictors: there is a sign of a slight degradation in accuracy in channels 17 and 22 (respectively at the edge and near the centre of the 183 GHz water vapour line), but the differences in bias and standard deviation for the v7 and v13 predictors are well below 0.1K in all channels.

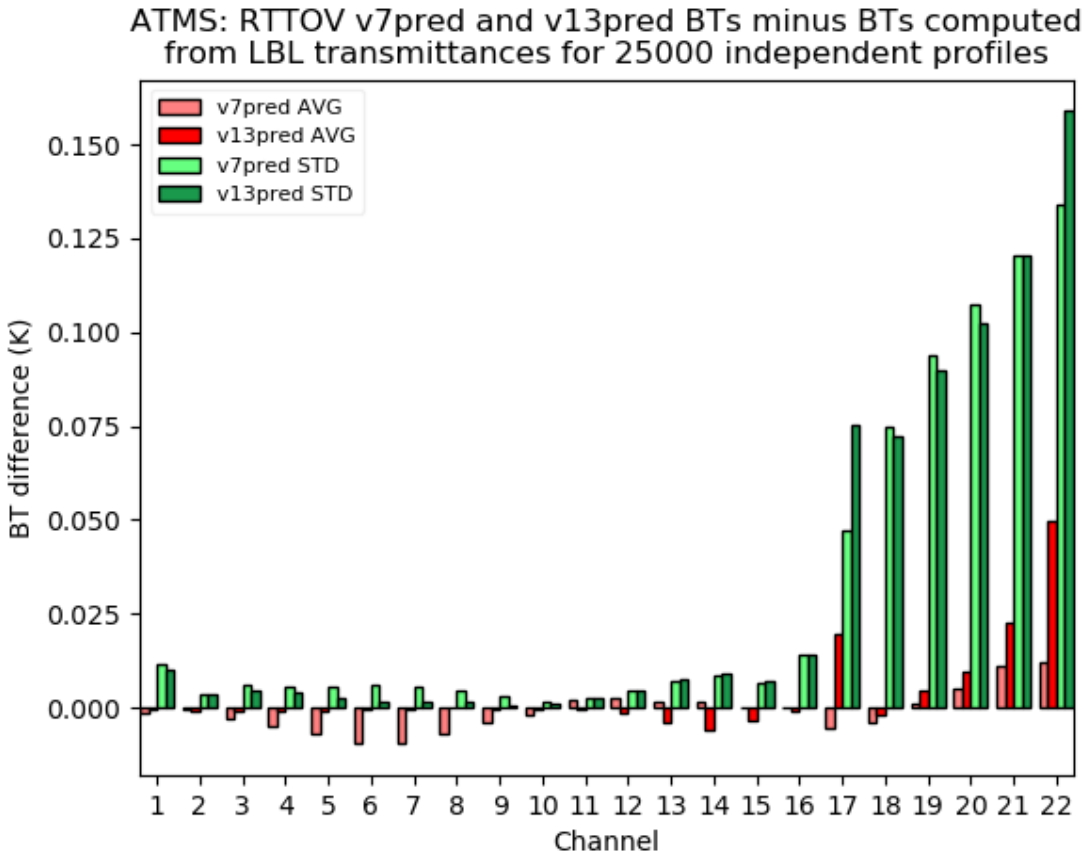

Figure 3.2.1 shows ATMS brightness temperature differences between RTTOV and the line-by-line channel-integrated transmittances over 25000 independent profiles and 6 secants. RTTOV BTs are computed using v7 predictors and v13 predictors.

Figures 3.2.2 - 3.2.4 show plots of the fit of RTTOV radiances to radiances calculated from the channel-integrated LBL transmittances used to train RTTOV over 6 secants (zenith angles up to ~64°). These are the differences which the optical depth parameterisation is seeking to minimise since this is how the top-of-atmosphere radiances are calculated within RTTOV (i.e. by a single integration of the radiative transfer equation using channel-integrated transmittances). The simulations for IR channels use a surface emissivity of 1. For the visible/near-IR channels, a surface BRDF of 0.3/π is used and a variety of satellite and solar zenith angles are simulated, each time with a relative azimuth angle of 180°.

Figure 3.2.2 shows plots for the GOES-16 ABI IR channels for the v7, v8, v9 (O_3+CO_2) and v13 (O_3+CO_2) predictors. Note that the v9 and v13 predictor coefficients are trained over the full range of zenith angles (up to ~85°) since this is a geostationary sensor, but the performance of the v13 predictors is nearly as good as the v7 predictors (only trained for zenith angles up to ~64°). The v8 and v9 predictors have large biases in the water vapour channels (6-7µm) and the CO_2 channel (13µm). The new predictors, like the v7 predictors, exhibit low biases in all channels. Standard deviations are also improved compared to the v9 predictors.

Figure 3.2.3 shows plots for the GOES-16 ABI visible/near-IR channels for the v9 and v13 predictors (both O_3+CO_2). Again, the v13 predictors compare favourably with the v9 predictors, with a substantial reduction in differences at 1.37µm. Although there is strong water vapour absorption at 1.37µm, the training profile set includes some dry profiles for which this channel is surface-sensitive. It is from these cases that we see the impact of the optical depth prediction.

Figure 3.2.4 shows plots for the IASI 101L coefficients based on v9 (O_3+CO_2) and v13 (O_3+CO_2) predictors. Once again, the v13 predictors compare favourably to the older parameterisation. Biases are eliminated across the spectrum, and the standard deviation is reduced in many regions.

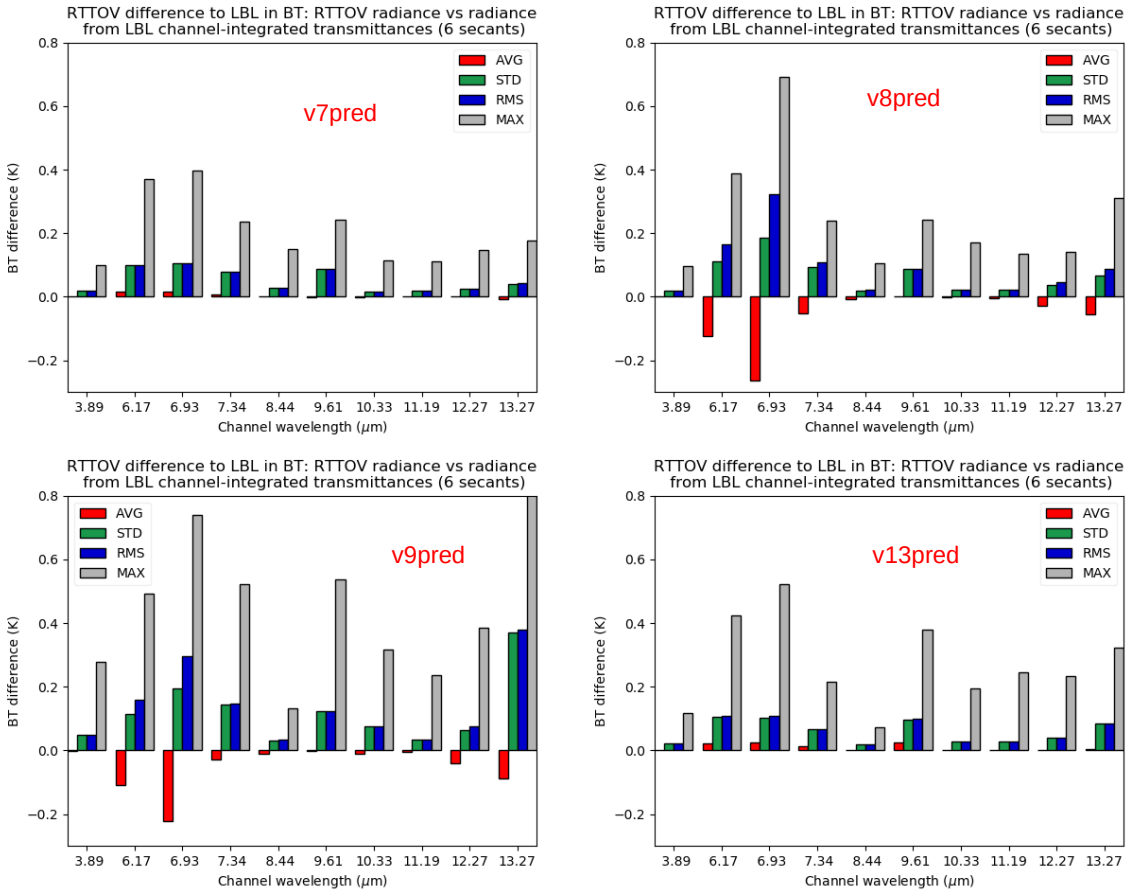

Figure 3.2.2 showing fit of RTTOV to radiances calculated from channel-integrated LBL transmittances for GOES-16 ABI IR channels for the v7 (top left), v8 (top right), v9 (O_3+CO_2, bottom left) and v13 (O_3+CO_2, bottom right) predictors. The maximum difference with the v9 predictors for the CO_2 channel (13.27μm) is ~1.6K.

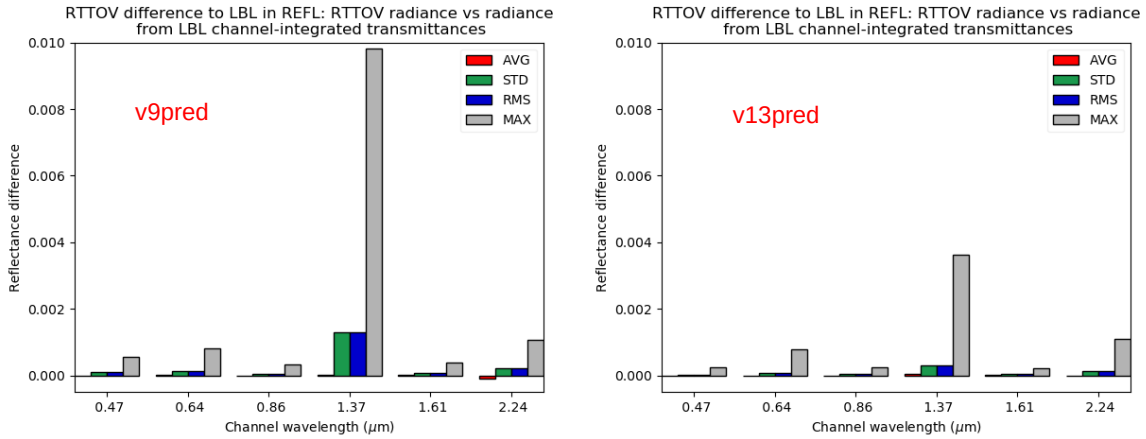

Figure 3.2.3 showing fit of RTTOV to radiances calculated from channel-integrated LBL transmittances for GOES-16 ABI visible/near-IR channels for the v9 (O_3+CO_2, left) and v13 (O_3+CO_2, right) predictors.

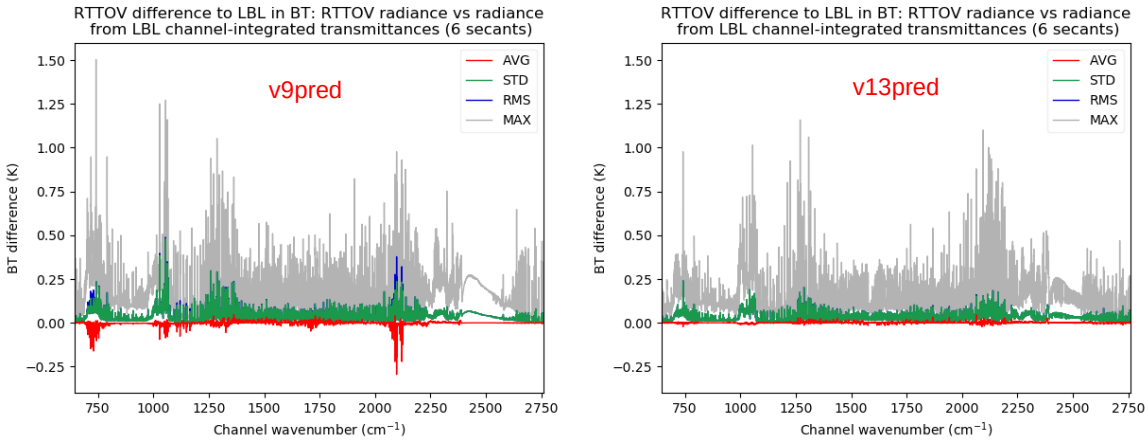

Figure 3.2.4 showing fit of RTTOV to radiances calculated from channel-integrated LBL transmittances for IASI channels for the v9 (O_3+CO_2, left) and v13 (O_3+CO_2, right) predictors.

3.2.3 Variable SO_2

SO_2 has proved challenging for the optical depth regression as concentrations can vary by several orders of magnitude from typical background anthropogenic values to extremely large concentrations due to volcanic activity. When SO_2 was added as a variable gas in RTTOV v12, the water vapour predictors were used as water vapour also exhibits large variability. However, the accuracy of the SO_2 optical depth prediction for high (volcanic) concentrations was substantially lower than that for “clean” (non-volcanic) profiles or other trace gases (R12REP2017). In RTTOV v13, the water vapour predictors have again been used for SO_2, and while the accuracy is improved compared to the v9 predictors, the errors for high volcanic concentrations remain larger than for the other gases.

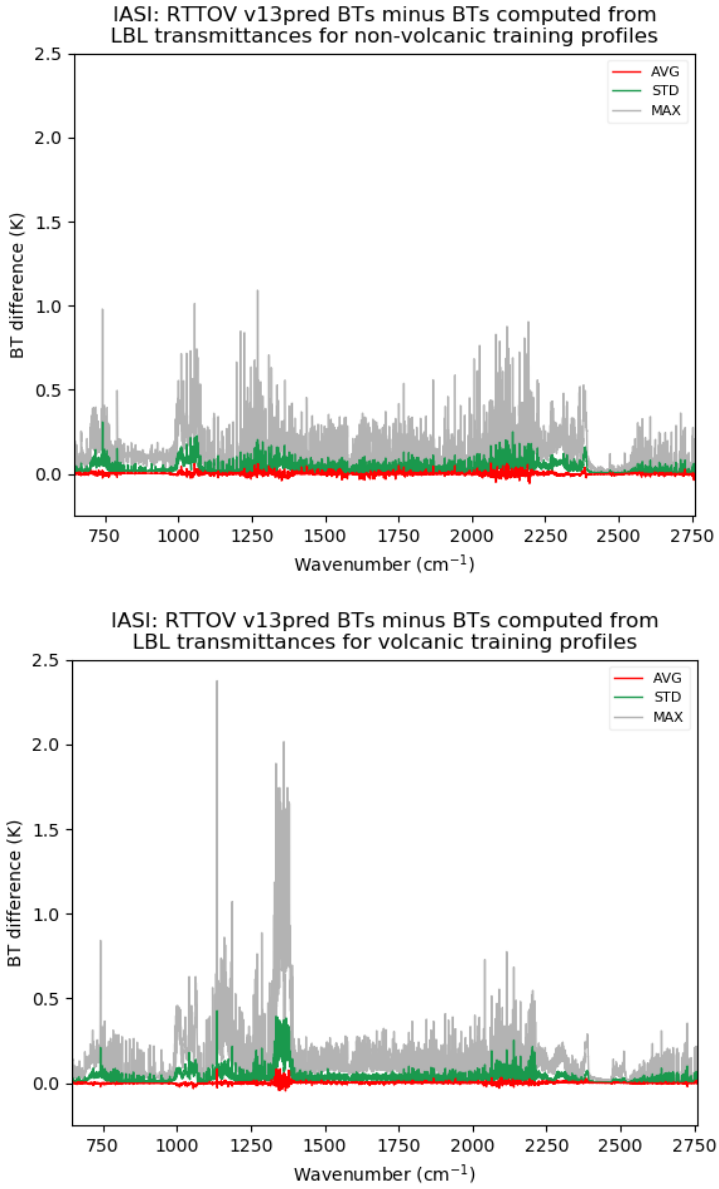

Figure 3.2.5: showing statistics of differences in IASI BTs between RTTOV v13 predictor 7gas coefficients and those computed from the channel-integrated line-by-line transmittances for the training profiles over 6 secants. The top panel restricts the comparison to the non-volcanic training profiles, the bottom panel includes only the volcanic cases. (NB the line-by-line transmittances and RTTOV coefficients used in these plots are based on LBLRTM v12.2).

Figure 3.2.5 shows plots of the fit of RTTOV to radiances calculated from the channel-integrated line-by-line transmittances used to train RTTOV for the IASI "7gas" coefficient file (i.e. coefficients enabling all supported variable gases). The figure shows separately the

differences for the non-volcanic training profiles and the differences for the volcanic cases. Brightness temperatures are computed assuming a surface emissivity of 1 over the 6 zenith angles used to train coefficients (up to ~64°). Errors for the non-volcanic cases are similar in magnitude to the O_3+CO_2 IASI coefficients in Figure 3.2.4 and the errors for the volcanic cases, while larger than the clear case in the SO_2 bands, compare favourably with the lower panel of Figure 11 in R12REP2017 showing the volcanic cases for the v9 predictors.

Figure 3.2.6 shows plots of the fit of RTTOV to channel-integrated line-by-line radiances for 52 independent profiles for IASI "6gas" (all variable trace gases excluding SO_2) and "7gas" v13 predictor coefficients, and the 6gas v9 predictor coefficients. This profile dataset includes variable O_3 and CO_2, but all other trace gases use the fixed RTTOV background profiles. The statistics are again calculated over 6 zenith angles with a surface emissivity of 1.

The statistics for the v13 predictor files compare well with those for the v9 predictors. Moreover, the errors are very similar for the two v13 predictor coefficient files: the performance of the 7gas file for non-SO_2 simulations is very close to that of the 6gas file. It is therefore planned only to provide 7gas coefficient files for v13 predictors and not to produce 6gas files unless specifically requested by users.

3.3 Cloud liquid water absorption for microwave simulations

3.3.1 Water permittivity parameterisations

RTTOV has for a long time included a parameterisation of cloud liquid water (CLW) absorption which can optionally be used for non-scattering (clear sky) microwave simulations. The original implementation which computes optical depths from the input CLW mass mixing ratio follows Liebe (1989). A key part of the calculation is the parameterisation of liquid water permittivity. Recent studies (e.g. Lonitz and Geer, 2018) have shown that the Liebe parameterisation does not represent super-cooled clouds well. Nor was the parameterisation designed for frequencies above 200GHz which are important for new sensors (Metop-SG ICI). Two new parameterisations, Rosenkranz (2015) and Turner, Kneifel, and Cadeddu (2016) or TKC, have been implemented as options alongside the Liebe permittivity parameterisation. The Rosenkranz parameterisation is intended to be valid for frequencies up to 1THz, while TKC is valid up to 500GHz.

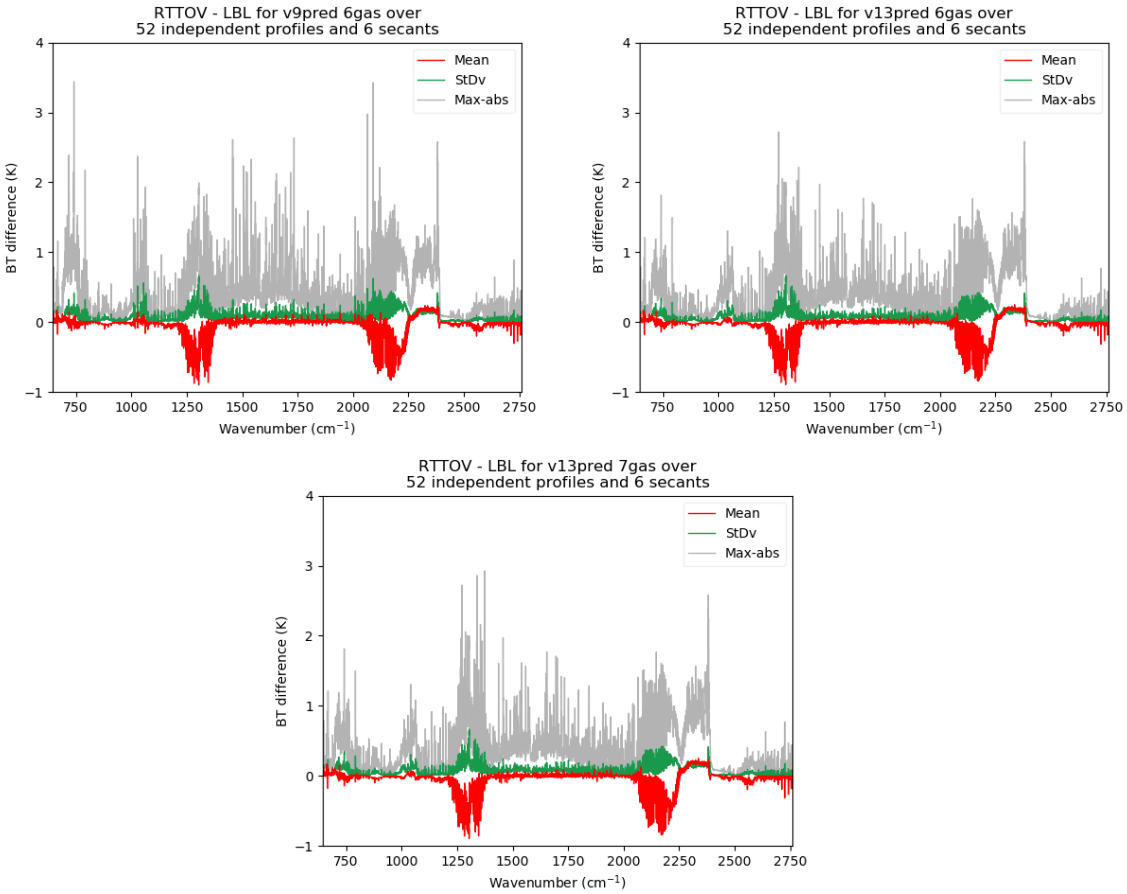

Figure 3.2.6: comparing RTTOV with channel-integrated line-by-line radiances for a 52 profile independent profile dataset over 6 secants with unit surface emissivity. Clockwise from top-left: v9 predictor 6gas coefficients (all variable trace gases except SO_2), v13 predictor 6gas coefficients, v13 predictor 7gas coefficients (all variable gases including SO_2). (NB the line-by-line transmittances and RTTOV coefficients used in these plots are based on LBLRTM v12.2).

The Rosenkranz parameterisation expresses the relative permittivity $\varepsilon(\nu)$ at frequency ν (GHz) as a sum of the static dielectric constant $\varepsilon_s = \varepsilon(0)$ and contributions from two nominal spectral bands broadly representing the dominant influence of two different modes of motion of the molecular dipole moments under the influence of an electric field:

$$\varepsilon = \varepsilon_s - \Delta_R\big(1 - F_R(\nu)\big) - \Delta_B\big(1 - F_B(\nu)\big)$$

The subscript R corresponds to the reorientation mode whereby a hydrogen bond is broken and reformed with another molecule. The subscript B corresponds to intermolecular vibrational bending. Other vibrational modes are noted, but their influence is largely confined to frequencies above 1THz (i.e. beyond the intended range of the parameterisation) and they are therefore not considered. The Δ parameters represent the amplitude of each band

in the model, while the complex shape factors $F(\nu)$ satisfy $F(0) = 1$ and $F(\infty) = 0$. The components of the parameterisation are as follows, in which T is the temperature (°C) and $\theta = \frac{300}{T+273.15}$:

$$\varepsilon_s = -43.7527\theta^{0.05} + 299.504\theta^{1.47} - 399.364\theta^{2.11} + 221.327\theta^{2.31}$$

$$\Delta_R = 80.69715\exp\left(-\frac{T}{226.45}\right)$$

$$\gamma_R = 1164.023\exp\left(-\frac{651.4728}{T+133.07}\right)$$

$$F_R(\nu) = \frac{\gamma_R}{\gamma_R + i\nu}$$

$$\Delta_B = 4.008724\exp\left(-\frac{T}{103.05}\right)$$

$$\nu_1 = 10.46012 + 0.1454962T + 0.063267156T^2 + 0.00093786645T^3$$

$$z_1 = (-0.75 + i)\nu_1 \qquad z_2 = -4500 + 2000i$$

$$F_B(\nu) = \frac{\log\left(\frac{z_2 - i\nu}{z_1 - i\nu}\right)}{2\log\left(\frac{z_2}{z_1}\right)} + \frac{\log\left(\frac{z_2^* - i\nu}{z_1^* - i\nu}\right)}{2\log\left(\frac{z_2^*}{z_1^*}\right)}$$

The TKC parameterisation follows a double-Debye model:

$$\varepsilon_s = s_0 + s_1T + s_2T^2 + s_3T^3$$

$$\Delta_i = a_i\exp(-b_iT) \qquad \tau_i = c_i\exp\left(\frac{d_i}{T + t_c}\right)$$

$$A_i = \frac{\tau_i^2\Delta_i}{1 + (2\pi\nu\tau_i)^2} \qquad B_i = \frac{\tau_i\Delta_i}{1 + (2\pi\nu\tau_i)^2}$$

$$\varepsilon' = \varepsilon_s - (2\pi\nu)^2\sum_{i=1}^{2} A_i \qquad \varepsilon'' = (2\pi\nu)\sum_{i=1}^{2} B_i$$

$$\varepsilon = \varepsilon' + i\varepsilon''$$

where T is the temperature (°C), ν is the frequency (Hz) and the fitted coefficients s_j, a_i, b_i and t_c are given in Table 3.3.1.

$a_1 = 81.11$	$a_2 = 2.025$	$s_0 = 87.914$	$t_c = 134.2$
$b_1 = 4.434 \times 10^{-3}$	$b_2 = 1.073 \times 10^{-2}$	$s_1 = -0.40440$	
$c_1 = 1.302 \times 10^{-13}$	$c_2 = 1.012 \times 10^{-14}$	$s_2 = 9.5873 \times 10^{-4}$	
$d_1 = 662.7$	$d_2 = 608.9$	$s_3 = -1.3280 \times 10^{-6}$	

Table 3.3.1: coefficients used in the TKC liquid water permittivity parameterisation.

Figure 3.3.1 shows plots comparing the absorption coefficient (strictly speaking, the quantity plotted is proportional to the absorption coefficient) for the three parameterisations implemented in RTTOV at temperatures of 0°C and -40°C. At the higher temperature, the parameterisations are very similar for frequencies up to around 250GHz, beyond which they diverge. However, for the supercooled case the parameterisations begin to differ substantially at frequencies well below 100GHz.

These two new permittivity parameterisations have also been implemented in the RTTOV-SCATT hydrotable generation code (see Section 3.11), and the Rosenkranz option was selected for the cloud liquid water and rain hydrometeor types when generating the default hydrotables based on results of all-sky assimilation experiments conducted at ECMWF (Lonitz and Geer, 2018). As such, Rosenkranz is also the recommended option for the MW CLW absorption calculations.

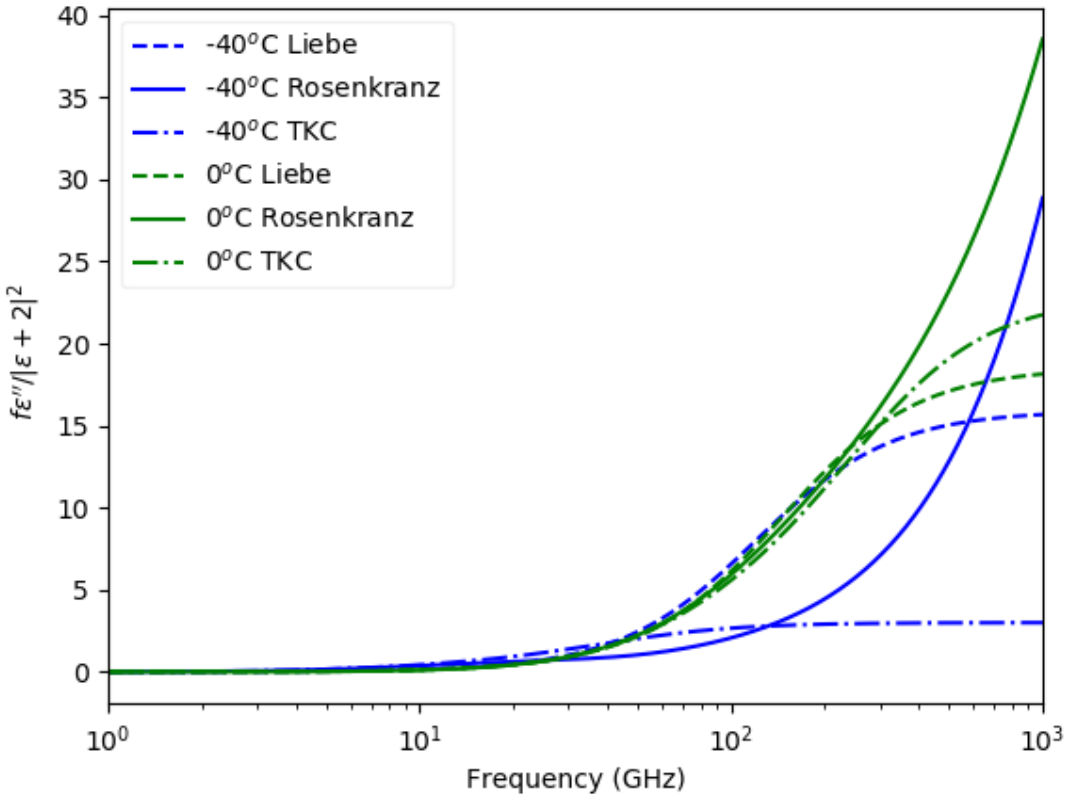

Figure 3.3.1 comparing the absorption coefficient against frequency at two temperatures for the 3 liquid water permittivity parameterisations implemented in RTTOV. The quantity plotted on the y-axis is proportional to the absorption coefficient: f is the frequency, and $\varepsilon = \varepsilon' - i\varepsilon''$ is the permittivity.

3.3.2 MW CLW absorption calculations on input pressure levels

For historical reasons, the CLW parameterisation in RTTOV has been performed on the gas optical depth coefficient pressure levels, involving the interpolation of the input CLW profile onto the levels used for the gas optical depth coefficients. In fact, the CLW optical depth calculation is separate from the gas optical depth parameterisation, and so there is no need for this interpolation. On the contrary, it is better to avoid interpolation of input profiles where possible since this inevitably introduces errors by displacing the cloud in the vertical to some extent. In RTTOV v12.2 an option was introduced to enable the CLW calculation on the user input pressure levels.

Figure 3.3.2 illustrates the impact of the CLW calculations on coefficient vs user levels for two MHS channels. Although mostly the differences are small, for certain profiles they can reach several Kelvin (up to ~4K differences at 89GHz, and up to ~6K at 157GHz) indicating that this could have a significant impact on simulations. As such, the new option to carry out

the calculations on user levels was recommended to users in RTTOV v12.2, and in RTTOV v13 the option has been removed so that all CLW calculations are now done on user levels.

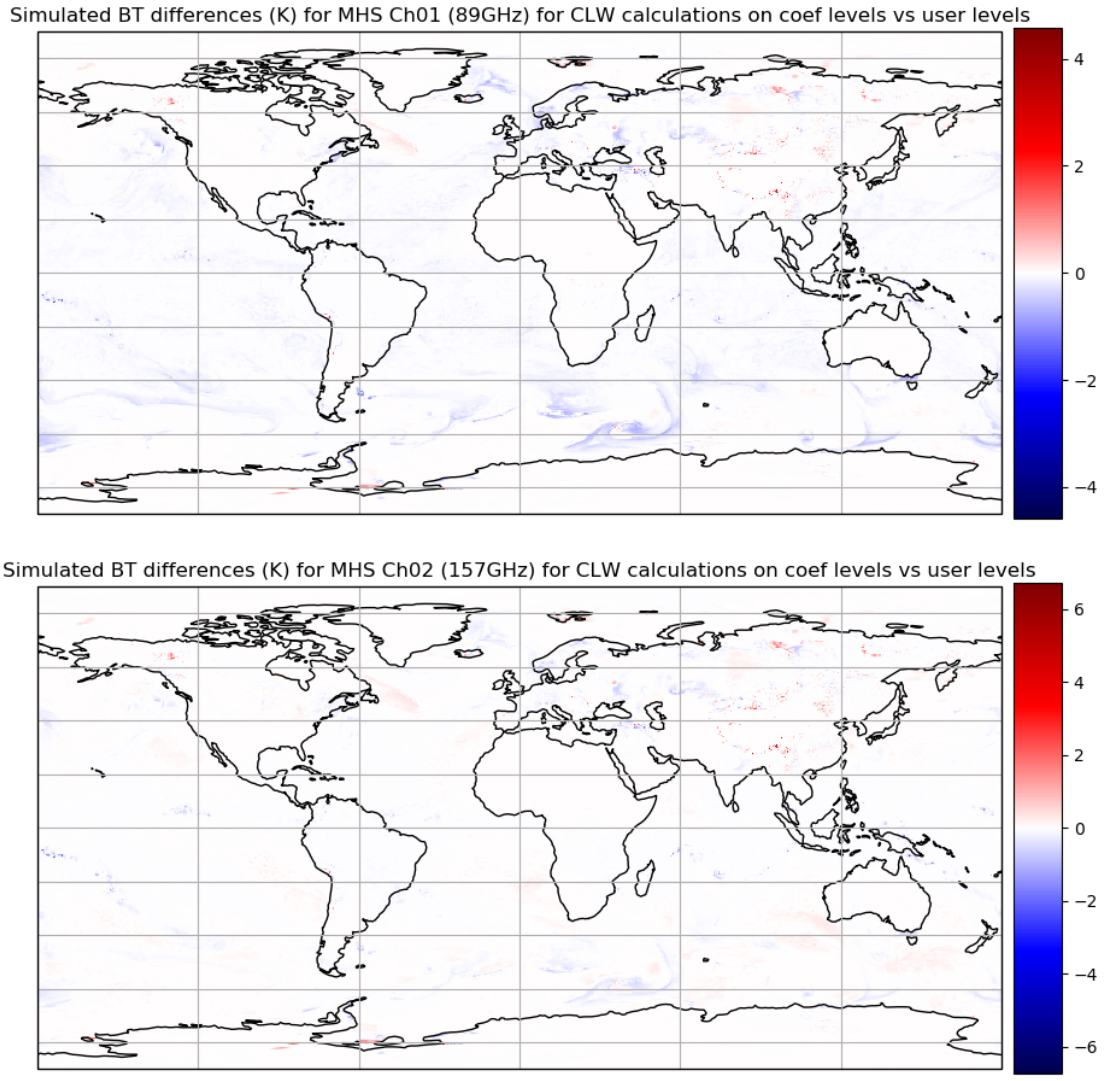

Figure 3.3.2: Maps showing differences in simulated brightness temperatures for MHS channels 1 and 2 for MW CLW absorption calculations on coefficient levels vs user levels.

3.4 Cloud optical properties for visible/IR scattering simulations

RTTOV provides pre-defined optical properties for cloud liquid and ice water scattering simulations in the visible and IR. In earlier versions, the only cloud liquid water properties available were based on the OPAC dataset (Hess *et al*, 1998). RTTOV v12.2 introduced an additional set of properties expressed in terms of particle size ("CLW Deff" properties, see section 3.4.1.2 below). RTTOV v13 updates both sets of cloud liquid water properties with

new refractive index data (section 3.4.1.1). Both sets of cloud liquid water properties can be used with all solvers in RTTOV. With the initial implementation of the CLW Deff properties, users had to provide their own cloud particle size data. RTTOV v13 introduces a new parameterisation for the cloud liquid water droplet size (section 3.4.1.3).

For ice clouds, the Baum dataset (Baum *et al*, 2011) expresses the optical properties in terms of particle size. These can be used with all solvers in RTTOV. RTTOV also provides parameterisations of the Baran ice optical property database (Baran *et al*, 2014; Vidot *et al*, 2015). RTTOV v12.3 introduced an updated parameterisation of the Baran database which has improved spectral consistency (section 3.4.2). The Baran properties can be used with all solvers in RTTOV except for MFASIS.

3.4.1 Water cloud

3.4.1.1 Liquid water refractive index for the OPAC cloud liquid water optical properties

The pre-existing cloud liquid water optical properties are taken from the OPAC database (Hess et al, 1998). The refractive index data used in the OPAC dataset comes from Hale and Querry (1973), but the data are stored at reduced spectral resolution compared to the original, and as such miss some spectral features in the original Hale and Querry data.

Segelstein (1981) updated the Hale and Querry refractive index dataset with more recent data and provides the refractive indices at higher spectral resolution. This has been used to update the OPAC cloud liquid water optical properties provided for use with RTTOV.

Figure 3.4.1 shows the real and imaginary parts of the OPAC reduced resolution Hale and Querry refractive indices, the original Hale and Querry dataset, and the Segelstein indices. It is clear that the reduced OPAC dataset is missing spectral features, for example, in the ranges 1-2um, 2.5-3um, and near 5um. The plots also show that the Segelstein dataset includes spectral features not captured in the original Hale and Querry data, for example in the near-IR.

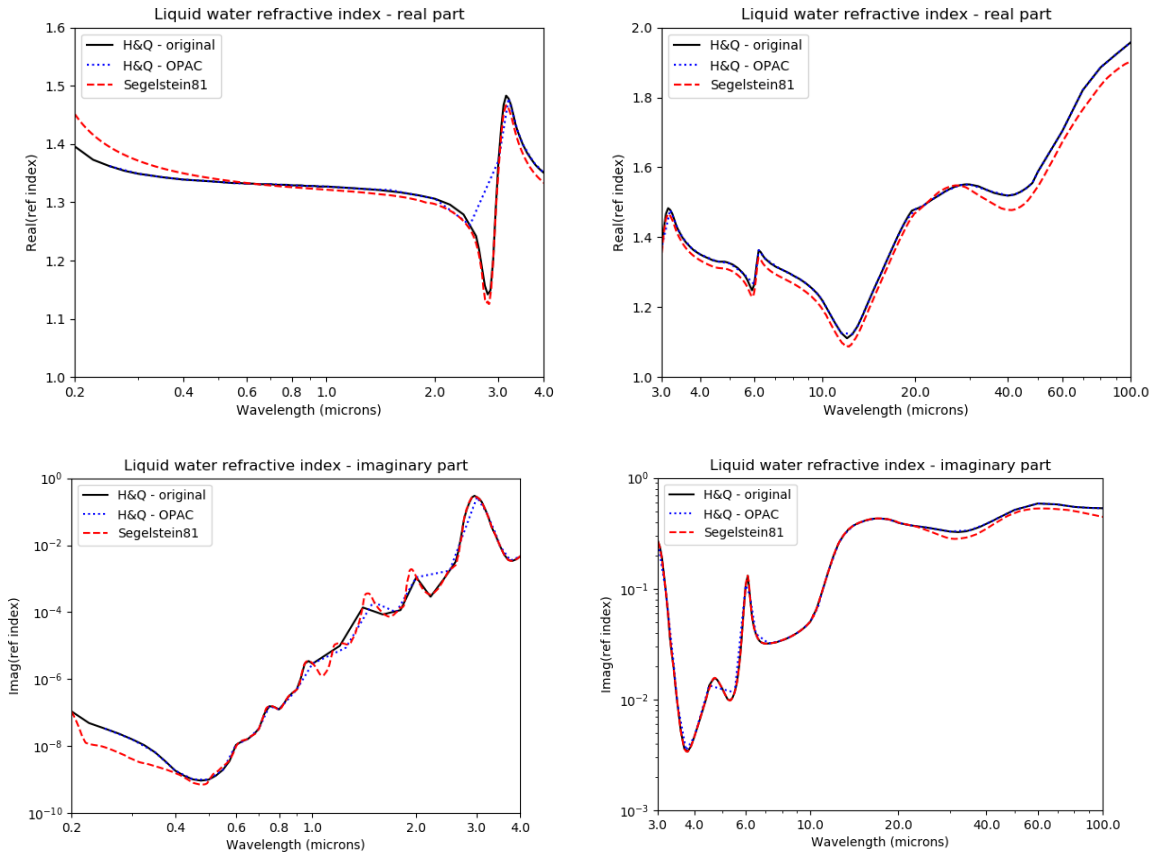

Figure 3.4.1 comparing liquid water refractive index datasets: the real and imaginary parts are shown in the top and bottom panels respectively. The left hand panels focus on the visible to the short-wave IR, while the right hand panels show the thermal IR.

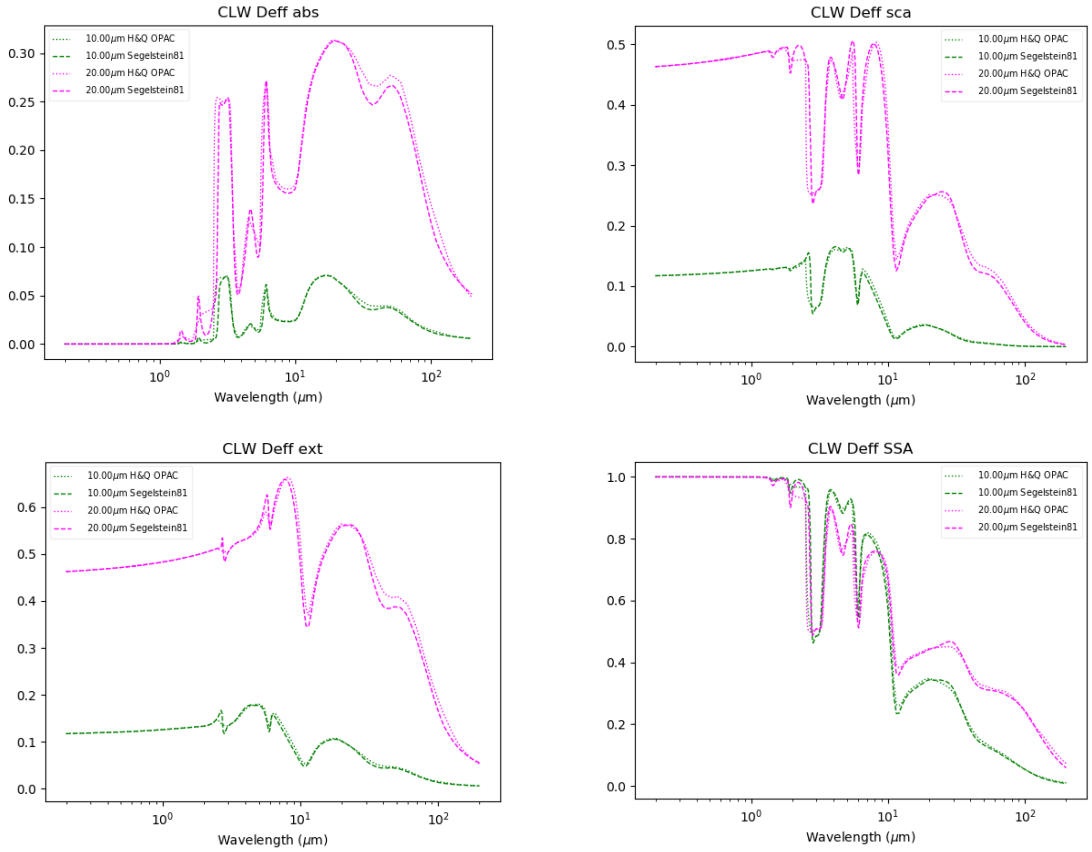

Figure 3.4.2 comparing cloud optical properties (clockwise from top left: absorption coefficient, scattering coefficient, single-scattering albedo, extinction coefficient) for the CLW Deff properties for two particle sizes for the OPAC Hale and Querry refractive indices and the Segelstein indices.

Figure 3.4.2 shows the CLW Deff Mie optical properties (see below) for 2 particle sizes for the OPAC Hale and Querry refractive index dataset and the Segelstein dataset. Plots for the OPAC properties are very similar, corresponding to the modal diameter specified for each OPAC particle type as specified in Hess *et al* (1998).

3.4.1.2 New optical properties expressed in terms of particle size

A new set of cloud liquid water optical properties explicitly defined in terms of particle size was desirable for use with the MFASIS fast visible cloud solver (section 3.9), as the model parameterises top of atmosphere reflectances in terms of particle size (among other parameters). In addition, such properties are useful where NWP models have two-moment cloud schemes such that the effective particle size is an explicit variable that may be retrieved/assimilated. The properties implemented are based on the size distribution assumed by the Mie optical properties in the libRadtran software (Emde *et al.*, 2016). These optical properties were first produced for RTTOV v12.2 using the OPAC refractive index

dataset mentioned above. For RTTOV v13, this has been replaced by the Segelstein (1981) dataset which is consistent with both the updated RTTOV "OPAC" optical properties and the libRadtran Mie properties.

Following the libRadtran Mie properties, a gamma distribution is used for the particle number density:

$$n(r) = ar^{\alpha}\exp(-br)$$

where the parameter α is set to 7, and b is determined according to $r_{\text{eff}} = \frac{\alpha+3}{b}$. The value of r_{eff} takes 24 values from 1-26μm (1-8μm in steps of 0.5μm, and 10-26μm in steps of 2μm). The value of a is determined such that the size distribution is normalised (i.e. $\int n(r)dr = 1\text{cm}^{-3}$). For each r_{eff} the normalised size distribution is computed. The range of values of r for the size distribution is initially between $r_{\min} = 0.2\mu\text{m}$ and $r_{\max} = 52\mu\text{m}$ for each r_{eff}. Depending on r_{eff}, this can yield very small values of $n(r)$ in the lower and upper tails which do not contribute significantly to the optical properties integrated over the size distribution. To exclude these tails and focus the calculations on the radii of interest, $r_{\min}$ is increased and $r_{\max}$ is reduced so that $n(r) > 10^{-8}$ for all values of r.

The size distribution is computed for radius values $r_i = r_{\min} \times \left(10^f\right)^{(i-1)}$, $i = 1, m$, where m is the smallest integer such that $r_m \geq r_{max}$ and where f is set to 0.001 for most sensors, but for hyperspectral IR sensors with many channels it is set to 0.005 to avoid excessive run-times. The finer grid is important for visible and near-IR channels, but is not required for longer wavelengths. This follows what has been done for the pre-existing OPAC aerosol and OPAC cloud liquid water optical properties.

The liquid water content (LWC) is calculated by first computing the total volume of spherical water droplets integrated over the size distribution, and then multiplying this by the density of water ρ (assumed 1 g/cm^3):

$$LWC = \frac{4\pi}{3}\rho\int_{rmin}^{rmax} r^3 n(r)\, dr$$

The absorption and scattering coefficients for each sensor channel are then computed and integrated over the size distribution according to Mie theory using the existing routines used for calculating aerosol and cloud liquid water Mie properties. These values are divided by the LWC to give the coefficients per unit liquid water content.

Within RTTOV the optical properties for each sensor channel are interpolated according to the specified effective diameter ($D_{\text{eff}} = 2r_{\text{eff}}$) for the given layer, and these are multiplied by the input layer cloud liquid water content and the layer thickness to obtain the layer cloud optical depth.

3.4.1.3 Parameterisation of CLW D_{eff}

In the initial implementation of the new optical properties in RTTOV v12.2 users had to provide the input D_{eff} (particle effective diameter) values explicitly. In RTTOV v13 a parameterisation for CLW D_{eff} has been implemented so explicit input of values is now optional. This is similar in principle to the existing parameterisations available in RTTOV for ice optical properties that are expressed in terms of particle size.

The parameterisation is based on Martin *et al.* (1994) in which the particle effective diameter in microns is given by:

$$D_{\text{eff}} = 2 \times 10^6 \left(\frac{3\text{LWC}}{4\pi k n_{tot} \rho_w} \right)^{\frac{1}{3}}$$

where LWC is the cloud liquid water concentration (kg/m^3), *k* is 0.67 for continental clouds and 0.80 for maritime clouds (no units), n_{tot} is the cloud particle number density (cm^{-3}) and ρ_w is the density of water (taken as 1000 kg/m^3). The continental and maritime values of n_{tot} are parameterised in terms of aerosol concentration in the layer immediately below the cloud. For simplicity, the values used in RTTOV are 100 cm^{-3} and 300 cm^{-3} for maritime and continental clouds respectively which correspond approximately to the mid-points of the two ranges in Figure 8c of Martin *et al.* This parameterisation was explicitly determined for warm stratocumulus clouds and as such may be limited in its applicability in convective regimes, for example. Users are advised to provide cloud particle size information consistent with their NWP model assumptions where possible, but this parameterisation provides a reasonable estimate in the absence of better information.

Computed D_{eff} smaller than 10μm are reset to 10μm as smaller values are unrealistic and the parameterisation is prone to giving very small values for the diameter at low cloud concentrations (Leonhard Scheck, personal communication).

Figure 3.4.3 shows histograms of observations and cloudy simulations covering day and night cases for several MSG-4 SEVIRI channels. The atmospheric and surface variables are from Met Office NWP fields taken from short-range forecasts valid close to the observation times. In particular, for the cloud, NWP model fields of cloud liquid water, cloud ice water and cloud fraction are used. The Chou-scaling fast scattering solver is used for thermal radiation and the DOM solver with 8 streams is used for solar radiation. For visible/near-IR channels only pixels with solar zenith angles below 85° are included, and the Rayleigh single-scattering approximation was used (see section 3.8). For channel 4 (3.9µm) only night-time pixels are included (solar zenith angle greater than 90°). For the thermal IR channels, both day and night pixels are included. The plots show histograms for the OPAC and D_{eff} properties based on the OPAC Hale and Querry refractive indices and the Segelstein indices.

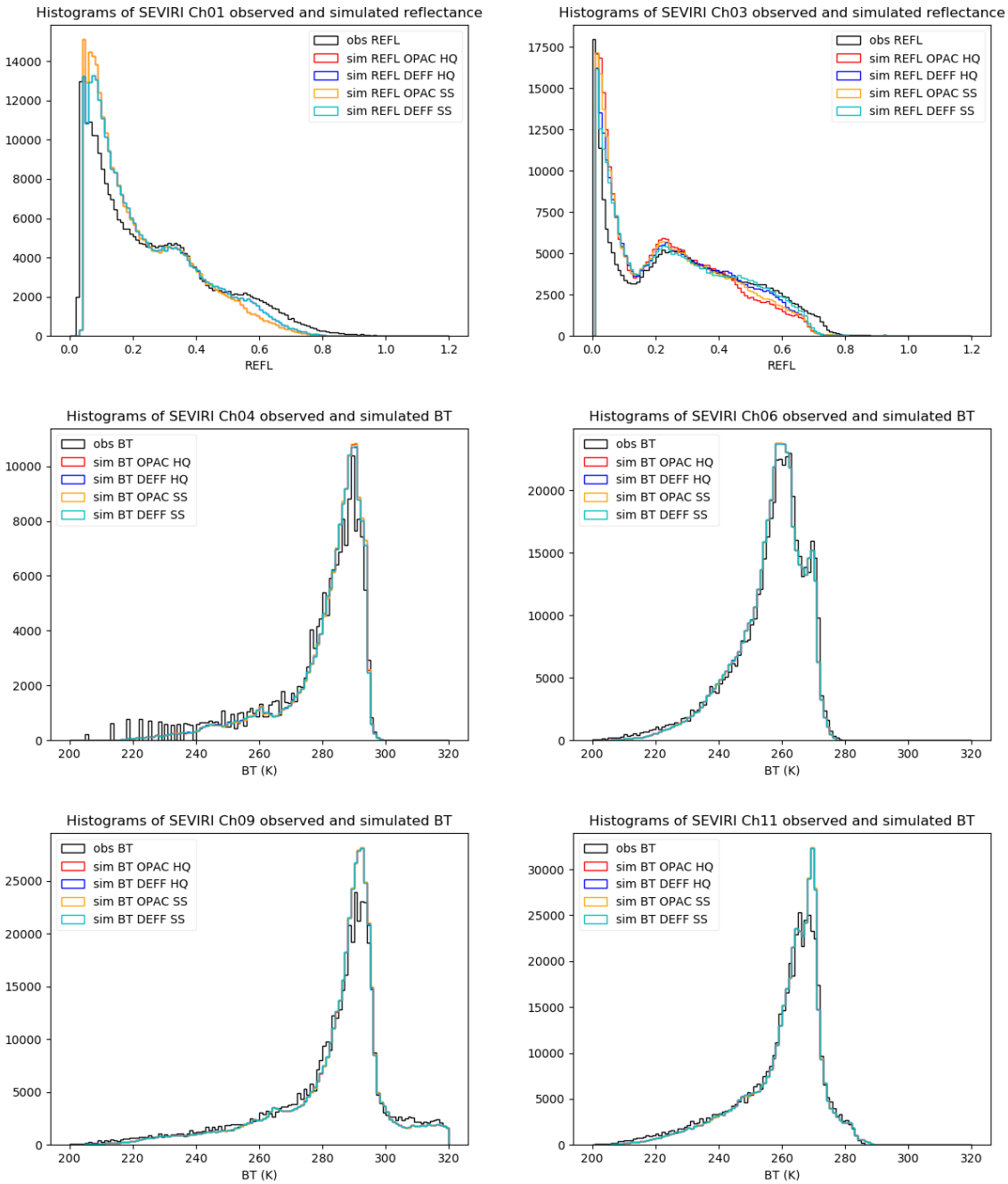

Figure 3.4.3: Histograms of observations and cloudy simulations for 6 MSG-4 SEVIRI channels. The histograms compare the OPAC and D_{eff} CLW properties computed using the OPAC Hale and Querry (HQ) and Segelstein (SS) refractive index datasets.

For the OPAC case, the stratiform continental and stratiform maritime liquid cloud types were used depending on the surface type, while for the Deff properties, the new CLW Deff

parameterisation was used. In all cases the Baran 2018 properties were used for ice cloud. In most channels the new refractive index dataset makes little difference, but some impact of the Segelstein dataset can be observed at 1.6μm. The new CLW Deff parameterisation appears to yield reasonable results, and in fact for most IR channels there is little difference in the histograms between the OPAC and Deff properties. The benefit of displaying the data in histograms is that it avoids penalising the radiative transfer calculations where the model cloud fields do not match the reality. Assuming the NWP model has a broadly realistic distribution of clouds over the whole Earth disc, then we see that, especially in the IR channels, the simulations are producing the same distributions of brightness temperatures as seen in the observations which indicates that the radiative transfer is performing well.

One can also examine the differences between the simulated and observed brightness temperatures and reflectances directly. These are shown in Figure 3.4.4 which plots the mean and standard deviation of the simulated minus observed differences against total cloud optical depth (COD). Here the COD is calculated from the simulations using the OPAC CLW properties based on the Segelstein refractive index dataset, and it includes the total optical depth due to both liquid and ice cloud. The pixels are assigned to COD bins of width 5 i.e. pixels are assigned to one of 11 bins according to whether the COD is in the range 0-5, 5-10, …, or 50-55. RTTOV clips total optical depths greater than 50 to 50 so the final bin “50-55” includes COD values of 50 and above. The mean and standard deviations are then calculated for each bin and are plotted against the mid-point of the bins. In the three thermal IR channels we see little difference between the two sets of optical properties, nor with the updated refractive index dataset. In channel 4 (3.9 microns) there is a small indication that the CLW Deff properties have a smaller bias, but again the updated refractive indices are having a minimal impact at this wavelength. In channel 1 (0.6 micron) we see a much larger difference between the OPAC and Deff properties, but again minimal impact of the updated refractive indices. Finally, in channel 3 (1.6 microns) we see the impact of the updated refractive indices: there is a small increase in the standard deviation with the Segelstein dataset. However, the biases are reduced for the OPAC properties, while they are somewhat increased overall for the CLW Deff properties. It should be borne in mind that, as noted above, these statistics include the errors due to mismatches between the model and cloud fields which can yield substantial differences that are unrelated to the accuracy of the radiative transfer itself.

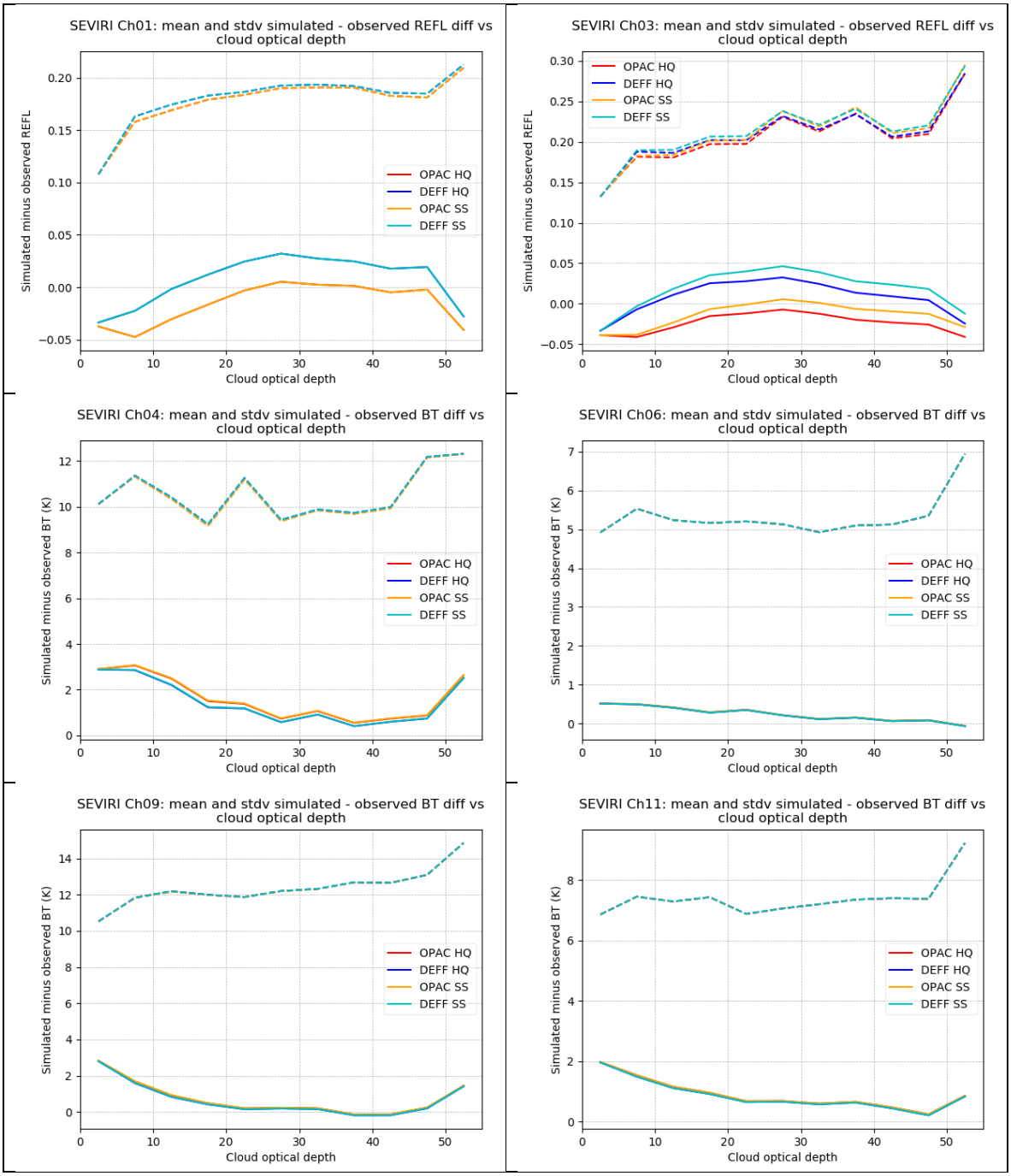

Figure 3.4.4: mean (solid lines) and standard deviation (dashed lines) of simulations minus observations for the same channels and simulations shown in Figure 3.4.3. The statistics are plotted against total cloud optical depth where the mean and standard deviation are computed for pixels falling within cloud optical depth bins of width 5.

3.4.2 Ice cloud

A new more spectrally consistent ice cloud optical properties database has been implemented in RTTOV for parameterization of the Baran model (named Baran2018 model). In 2014, a first database of optical properties (absorption and scattering coefficients, single scattering albedos and asymmetry parameters) of the Baran ensemble model of ice crystals were parametrized for RTTOV (Baran *et. al.*, 2014; Vidot *et al.*, 2015). However this database was found to be spectrally inconsistent between the visible/near infrared and the infrared spectral domains. On the Figures 3.4.4 and 3.4.5 are shown in blue the mean (full line) and the standard deviation (dashed line) of the absorption coefficient (Fig. 3.4.4) and of the scattering coefficient (Fig. 3.4.5). At 3 µm, a discrepancy is seen in both absorption and scattering coefficient. This is explained by the fact that the ensemble model of Baran is based on a Mass-Dimensional relationship of ice crystals defined as $M=aD^2$ where a=0.0257 in the Baran2014 model. However, the absorption and scattering coefficients were weighted by a single value in the IR part of the database in order to reproduce a value of a=0.05 to be more consistent with aircraft observations without recalculating the database. But the VIS/NIR part of the database was not weighted leading to this discrepancy. In 2018, the full database was regenerated with a=0.05 for all wavelengths and was extended to the far infrared up to 120 µm. This new database is more spectrally consistent (see the red lines of Figs 3.4.4 and 3.4.5) with lower absorption and scattering coefficients in the VIS/NIR spectral domains.

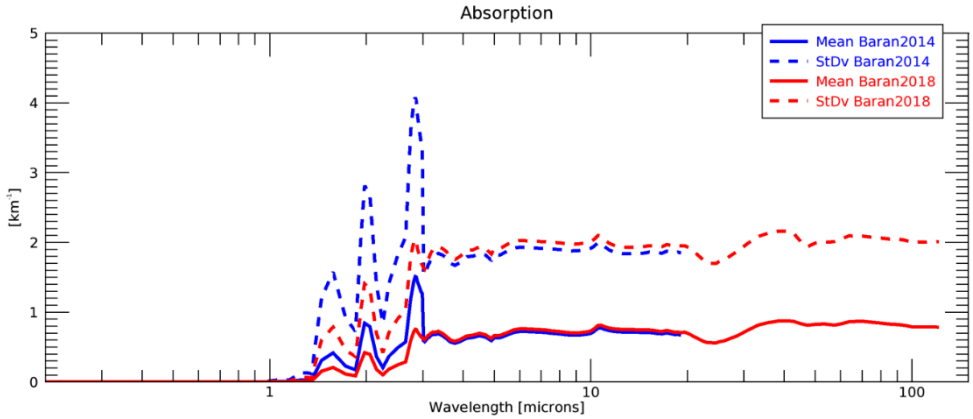

Figure 3.4.4: Mean (full lines) and standard deviation (dashed lines) of the spectral absorption coefficients (in km^{-1}) from the two Baran databases.

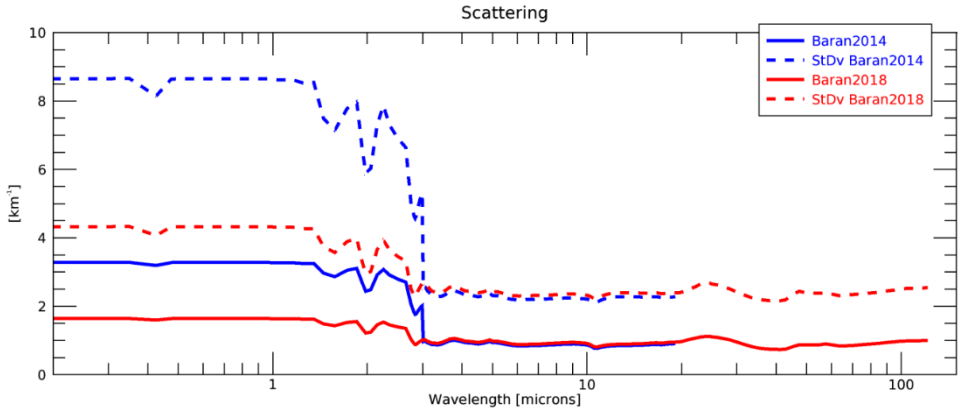

Figure 3.4.5: Mean (full lines) and standard deviation (dashed lines) of the spectral scattering coefficients (in km^{-1}) from the two Baran databases.

3.5 Aerosol optical properties for visible/IR scattering simulations

3.5.1 CAMS aerosol types[1]

A new set of aerosol optical properties based on the CAMS (Copernicus Atmosphere Monitoring Service) aerosol species (Bozzo *et al.*, 2020) have been implemented for use with RTTOV for visible/IR scattering simulations. These are provided in a new set of aerosol optical property files that may be used instead of the pre-existing files containing optical properties based on the OPAC components (Hess *et al*, 1998) plus some additional species.

The optical properties are computed from Mie theory. Properties for 9 CAMS species are implemented: full details of the refractive indices and parameters for the size distributions are given in Bozzo et al (2020), a brief overview is given here:

Index 1 - Black carbon (hydrophobic)
Refractive index: fixed refractive index at all wavelengths
Size distribution: log-normal

Index 2-4 - Dust size bins 1-3 (hydrophobic)
Refractive index: Woodward (2001)
Size distribution: log-normal over all three size bins

Index 5 - Sulphates (hydrophilic)
Refractive index: Lacis et al (GACP, http://gacp.giss.nasa.gov/datasets/)

[1] *J. Hocking would like to acknowledge Alessio Bozzo (then at ECMWF) who provided much assistance in clarifying the definitions of the CAMS particle types to ensure consistency between the RTTOV and operational CAMS implementations.*

Size distribution: log-normal
Note: The optical properties are calculated for ammonia sulphate $(NH4)_2SO_4$ while CAMS/IFS advects SO_4 aerosol. To account for this the mass factor used in calculating the particle number density from the input mass ratio in kg/kg is scaled by the ratio of the two molecular weights: $(NH_4)_2SO_4/SO_4$=132/96.

Index 6-8 - Sea salt size bins 1-3 (hydrophilic)
Refractive index: OPAC SSAM
Size distribution: bi-modal log-normal over all three size bins

Index 9 - Organic matter (hydrophilic)
This is a weighted mixture of three OPAC components.
Refractive index: OPAC SOOT, INSO, WASO
Size distribution: log-normal for each component

For all species RTTOV expects dry aerosol mixing ratio in kg/kg, except for sea salt for which it is the mixing ratio at 80% relative humidity. This is consistent with CAMS outputs.

3.5.2 Custom optical property files

A new executable has been created to enable users to create their own custom aerosol optical property files in RTTOV. The full instructions for using the tool are given in the header of the source code and are copied into a separate help file included in the RTTOV distribution: *docs/readme_rttov_make_scaercoef.txt*. A summary of the tool is given here.

All optical properties are computed using Mie theory and users can specify an arbitrary number of particle types. The tool allows for hydrophobic and hydrophilic species: as for the OPAC and CAMS aerosol species, the properties are interpolated in relative humidity at run-time within RTTOV. The executable is driven by simple ASCII input files. The primary input file specifies the number of particle types, and then for each particle type the following information:

- a four-character name to identify the aerosol type
- the number of relative humidity values (1 for hydrophobic, >1 for hydrophilic)
- a list of the relative humidity values in the range 0-99% (simply 0 for hydrophobic)
- either: the conversion factor for computing particle number density from mass density
- or: the density of the aerosol so that the tool can compute the conversion factor
- and finally, for each relative humidity value, paths to files containing the refractive indices and size distribution data.

The refractive index data are provided via ASCII input files with a simple format. The imaginary parts k may be positive or negative and are treated as if they should be negative i.e. the value $-|k|$ is used.

The size distribution data are similarly provided via ASCII input files specifying the particle densities for a range of particle sizes. The size distribution should be normalised so that the integral is 1, but the tool can do this normalisation if requested.

The conversion factor is used within RTTOV in the calculation of aerosol number density from input mass mixing ratio. The factor is calculated as $\frac{4\pi}{3}\rho\int r^3 n(r)dr$ where ρ is the aerosol density, r is the particle radius, and $n(r)$ is the normalised size distribution. As indicated above the tool can compute this, but users may wish to compute it themselves: for example, the integral for some conversion factors for some OPAC species in Hess *et al.* (1998) is not carried out over the full range of radius values. The tool uses the size distribution for a relative humidity of 0% for hydrophilic species, so users may also wish to compute the factor separately if this is not appropriate for their application.

3.6 Updates to Lambertian surface option

Parameterisation of effective angle for Lambertian option

By default, RTTOV calculates top-of-atmosphere radiances assuming specular reflection at the surface. An option to treat surfaces as Lambertian reflectors was implemented in RTTOV v11. The details are in the RTTOV v11 Science and Validation Report (R11REP2013). The implementation follows Matzler (2005) in which the Lambertian scattering is modelled using an effective incidence angle of 55° for the downwelling transmittances instead of the usual viewing zenith angle used for specular reflection.

In fact, the original paper included a non-linear dependence of the effective angle with respect to optical depth, and Guedj et al (2010) provide a polynomial fit as follows:

$$\theta_{eff} = 1.029024 - 0.367866\,OD + 0.344010\,OD^2 - 0.219791\,OD^3 + 0.078976\,OD^4 - 0.014515\,OD^5 + 0.001061\,OD^6$$

where OD is the surface-space nadir optical depth and is restricted to lie in the range $0.05 \leq OD \leq 4.0$. This function is shown in Figure 3.6.1. Figure 3.6.2 shows the means and standard deviations of brightness temperature differences for AMSU-A calculated over the 83 profile set used for training RTTOV optical depth coefficients. The plot shows the differences when using the fixed and parameterised angles for the Lambertian surface option for three viewing zenith angles for a surface emissivity of 0.75.

It is worth noting that the fixed angle of 55° is equivalent to a relatively low total optical depth (0.2) or equivalently a transmittance of about 0.8. Channels such as 1 and 15 which have strong sensitivity to the surface due to generally high transmittances have small mean differences showing that on average the fixed angle is a good approximation for the parameterised angle, but they show relatively large variability indicating that for some profiles the fixed angle is not so representative of the parameterisation due to variability in

the total transmittance. Conversely, channel 4 for example has large mean differences indicating that the fixed angle is not representative in general while the standard deviation is small, because the transmittances tend to cluster around lower values. The differences due to using the parameterised angle can be significant – up to 1K mean differences in channel 4 at nadir for this surface emissivity, for example.

The option to choose between the fixed and parameterised effective incidence angles is now available in RTTOV.

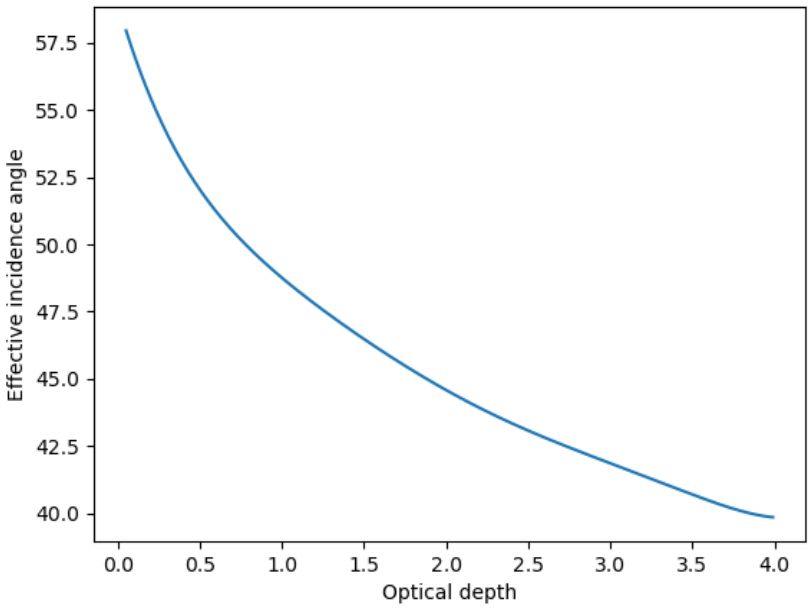

Figure 3.6.1: Effective incidence angle for Lambertian reflection as a function of optical depth.

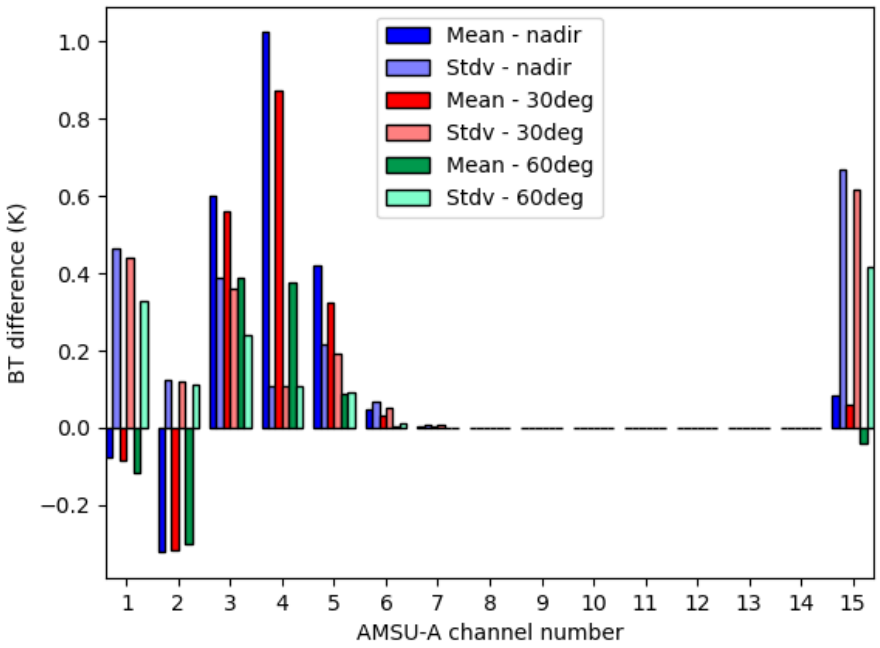

Figure 3.6.2: BT differences for fixed vs parameterised incidence angle for Lambertian surface option for AMSU-A for 3 viewing angles and a surface emissivity of 0.75. The mean and standard deviation are computed for the 83 diverse profiles used for training RTTOV optical depth coefficients.

Specularity parameter

Many surfaces are neither fully specular, nor fully Lambertian, but exhibit properties some way between the two. To address this a new specularity variable was introduced in RTTOV v12.3. This user-supplied parameter lies between 0 and 1, and is used to calculate a simple weighted average of the specular and Lambertian downwelling radiances:

$$L_{down} = sL_{spec} + (1 - s)L_{lamb}$$

where L_{down}, L_{spec} and L_{lamb} are the final, specular and Lambertian downwelling radiances and s is the specularity. Thus, a value of 1 represents fully specular reflection and a value of 0 represents fully Lambertian reflection. Initially this was implemented as a profile variable such that one value was applied for all channels simulated for a given profile. It was requested to enable the specification of specularity for each channel, as it may vary with frequency. This is implemented in RTTOV v13.

3.7 New sunglint BRDF model

A sunglint BRDF model based on Yoshimori et al (1995) was introduced in RTTOV v9 for solar radiation (Matricardi, 2003). This is a two-dimensional wave model in which the water

surface is regarded as a collection of small mirror-like facets each randomly tilted with respect to the local horizon, the orientation of the facets being constantly modified by the wind. The fraction of solar radiance reflected by the wind-roughened water surface is computed assuming that the slopes of the facets obey a two-dimensional Gaussian random process whose spectrum is specified by a parameterisation. The total variance of the slope of the facet is obtained from the frequency spectrum of the surface wave and the inverse function of the dispersive relation of the full-gravity-capillary wave. The shadowing of the facets on the backsides of the waves and deep in the troughs between waves is considered.

In the original implementation the wave spectrum parameterisation was taken from the Joint North Sea Wave Project (JONSWAP) model (Hasselmann *et al*., 1973). A new option has been introduced which uses the wave spectrum parameterisation presented in Elfouhaily *et al.* (1997). This parameterisation was selected as it significantly improved the fit to observations as illustrated in Figure 3.7.1 which shows histograms of simulated minus observed SEVIRI reflectances for the two parameterisations. The simulations used atmospheric and surface variables from Met Office NWP model fields taken from short-range forecasts valid close to the observation times. Only clear-sky (i.e. cloud-screened), sun-glint-affected pixels were included in the comparisons. The bias and standard deviation are significantly reduced with the new model.

The wave spectrum parameterisation depends on the 10m wind speed (u_{10}), the wind fetch (w_f), and the angle between the upwind direction and the viewing direction (φ). The wind speed is set to a minimum value of 0.6ms^{-1} to ensure the parameterisation gives a positive wave spectrum.

Ultimately the Yoshimori parameterisation requires the mean square slope in the upwind direction (mss_x) and in the crosswind direction (mss_y). These are given by:

$$\mathrm{mss}_x = \int_0^{\infty} \int_{-\pi}^{\pi} k^3 \cos^2 \varphi \Psi(k,\varphi)\, d\varphi\, dk$$

$$\mathrm{mss}_y = \int_0^{\infty} \int_{-\pi}^{\pi} k^3 \sin^2 \varphi \Psi(k,\varphi)\, d\varphi\, dk$$

where k is the wavenumber and the directional wave frequency spectrum is given by:

$$\Psi(k,\varphi) = \frac{1}{2\pi} k^{-4} [B_l + B_h][1 + \Delta(k)\cos(2\varphi)]$$

Here B_l and B_h represent contributions from low and high frequencies respectively, and $\Delta(k)$ is the spreading function accounting for dispersion. In order to compute these three quantities, a range of additional variables are computed as follows:

The nondimensional wind fetch X:

$$X = k_0 w_f, \qquad k_0 = \frac{g}{u_{10}^2}$$

where g is the acceleration due to gravity. The relationship between the inverse-wave-age Ω_c and wind fetch:

$$\Omega_c = 0.84 \tanh\left\{\left(\frac{X}{X_0}\right)^{0.4}\right\}^{-0.75}, \qquad X_0 = 2.2 \times 10^4$$

The wavenumber k_p at which the spectral peak occurs:

$$k_p = k_0 \Omega_c^2$$

The minimum phase speed c_m at wavenumber k_m associated with a gravity-capillary peak in the spectrum:

$$c_m = \sqrt{\frac{2g}{k_m}} = 0.23\ ms^{-1}$$

The phase speed $c(k)$, and the phase speed c_p at k_p are given by the dispersion relation:

$$c(k) = \sqrt{\frac{g\left[1 + \left(\frac{k}{k_m}\right)^2\right]}{k}}, \qquad c_p = c(k_p)$$

The dimensionless inverse-wave-age parameter Ω:

$$\Omega = \frac{u_{10}}{c_p}$$

The air friction velocity at the water surface u^*:

$$u^* = \frac{u_{10}}{25}$$

Note: u^* is the only place where the implementation deviates from the Elfouhaily *et al.* (1997) parameterisation. Alternative, more complicated parameterisations of u^* are presented in the paper, but the approximation above taken from Plant (1982) was preferred for its simplicity without degrading the fit to observations for SEVIRI.

The low frequency contribution to the wave spectrum B_l is computed as follows:

$$B_l = \frac{1}{2}\alpha_p \frac{c_p}{c} F_p$$

The generalised Phillips-Kitaigorodskii equilibrium range parameter for long waves α_p:

$$\alpha_p = 6 \times 10^{-3}\sqrt{\Omega}$$

The long-wave side effect function F_p is given by:

$$F_p = L_{PM} J_p exp\left\{-\frac{\Omega}{\sqrt{10}}\left[\sqrt{\frac{k}{k_p}} - 1\right]\right\}$$

The Pierson-Moskowitz shape spectrum L_{PM} is given by:

$$L_{PM} = exp\left\{-\frac{5}{4}\left(\frac{k_p}{k}\right)^2\right\}$$

The JONSWAP peak enhancement factor J_p is given by the following:

$$J_p = \gamma^{\Gamma}$$

$$\gamma = \begin{cases} 1.7 & 0.84 < \Omega_c < 1 \\ 1.7 + 6\log(\Omega_c) & 1 \leq \Omega_c < 5 \end{cases}$$

$$\Gamma = exp\ exp\left\{-\frac{\left(\sqrt{\frac{k}{k_p}} - 1\right)^2}{2\sigma^2}\right\}, \qquad \sigma = 0.08(1 + 4\Omega_c^{-3})$$

The high frequency contribution to the wave spectrum B_h is computed as follows:

$$B_h = \frac{1}{2}\alpha_m \frac{c_m}{c} F_m$$

The generalised Phillips-Kitaigorodskii equilibrium range parameter for short waves α_m:

$$\alpha_m = \begin{cases} 10^{-2}\left[1 + \ln\left(\frac{u^*}{c_m}\right)\right] & u^* < c_m \\ 10^{-2}\left[1 + 3\ln\left(\frac{u^*}{c_m}\right)\right] & u^* \geq c_m \end{cases}$$

The short-wave side effect function F_m is as follows:

$$F_m = exp\left\{-\frac{1}{4}\left[\frac{k}{k_m} - 1\right]^2\right\}$$

Finally, the spreading term is given by the following:

$$\Delta(k) = tanh\left\{a_0 + a_p\left(\frac{c}{c_p}\right)^{2.5} + a_m\left(\frac{c_m}{c}\right)^{2.5}\right\}$$

where

$$a_0 = \frac{\ln(2)}{4} \qquad a_p = 4 \qquad a_m = \frac{0.13u^*}{c_m}$$

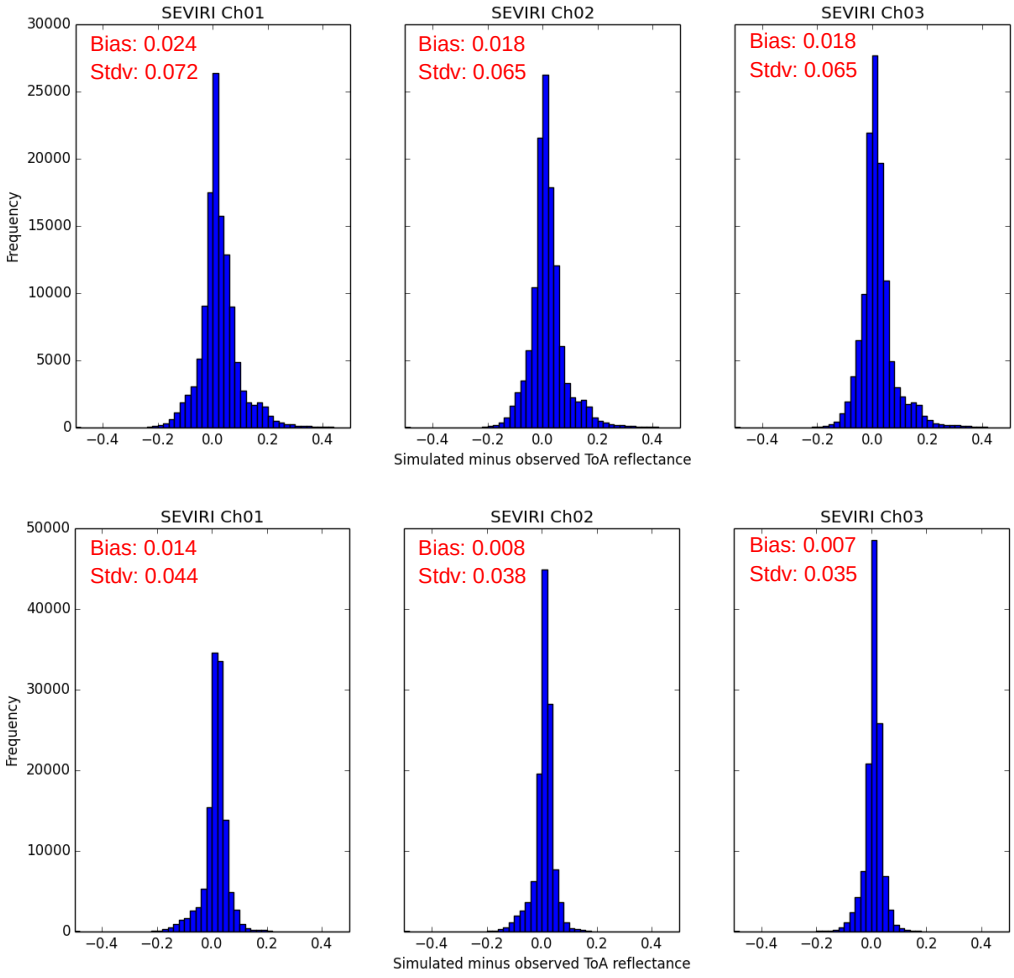

Figure 3.7.1: Histograms of simulated minus observed ToA reflectance for SEVIRI channels 1-3 for cloud-cleared pixels in sun-glint-affected regions. The top panel shows results using the JONSWAP parameterisation and the bottom panel shows results using the Elfouhaily et al (1997) parameterisation. Bias and standard deviation are given for each histogram.

3.8 Updates to treatment of Rayleigh scattering

3.8.1 Rayleigh extinction

The LBLRTM transmittances used for training the gas optical depth coefficients for visible and near-IR channels include Rayleigh extinction. The predicted gas optical depths for visible channels therefore include both the absorption due to the gases and the Rayleigh scattering extinction together for the v9 predictors. Users have requested the capability to

separate the Rayleigh scattering from the gas absorption, and indeed this is desirable for various reasons: for example, it would allow Rayleigh-cloud multiple scattering to be simulated in the RTTOV Discrete Ordinates Method (DOM) solver (Hocking, 2016) which would improve the accuracy of the simulations used for training the look-up tables for the MFASIS fast visible cloud parameterisation (Scheck, 2016), and it allows more sophisticated parameterisation of Rayleigh scattering which may be beneficial when RTTOV is extended to UV wavelengths in the future.

To meet this requirement, Rayleigh extinction is not included in the LBLRTM simulations used for training the new v13 predictor coefficients and is instead modelled using a fast parameterisation computed within RTTOV at run-time. This follows Bucholtz (1995) who provides a parameterisation of the Rayleigh volume scattering coefficient β_s at a standard temperature T_s and pressure p_s as a function of wavelength, and gives the scattering coefficient β at arbitrary temperature T and pressure p as

$$\beta = \beta_s \frac{T_s}{p_s}\frac{p}{T} \qquad (3.8.1)$$

To compute the layer optical depth due to Rayleigh extinction, β_s is averaged over the channel spectral response (this is done off-line), and the ideal gas law and hydrostatic equation are applied to equation 3.8.1 to obtain the layer nadir scattering optical depth:

$$\mathrm{OD}_{\mathrm{ray}} = \beta_s \frac{T_s}{p_s}\frac{R}{gM_{air}}\Delta p \qquad (3.8.2)$$

where R is the gas constant, g is acceleration due to gravity (assumed constant), M_{air} is the molar mass of dry air and Δp is the difference in pressure across the layer.

RTTOV provides an option to allow users to control the maximum channel central wavelength for which Rayleigh scattering effects are computed: this allows users to exclude the effects of Rayleigh scattering entirely if desired when using the new v13 predictor coefficients.

Figure 3.8.1 shows the difference between the v9 predictors and v13 predictors (variable O_3+CO_2) for the GOES-16 ABI visible/near-IR channels in RTTOV v13 over the 83 profiles used to train the RTTOV optical coefficients. The v9 predictors include Rayleigh extinction in the LBLRTM training simulations and employ the RTTOV v12 Rayleigh single-scattering calculation, while the v13 predictors use the new Rayleigh extinction parameterisation and modified single-scattering calculation (see below). The differences in channels 1-3 (at 0.47, 0.64, 0.86 microns respectively i.e. those significantly affected by Rayleigh scattering) are very small indicating the new treatment of Rayleigh scattering yields very similar results to that in RTTOV v12. There is a tendency for the differences to increase slightly as the

wavelength decreases which is expected since the impact of Rayleigh scattering increases at shorter wavelengths. The differences in channels 4-6 (at 1.37, 1.61 and 2.26 microns) are due only to the differences in the optical depth prediction since the impact of Rayleigh scattering is minimal in these channels.

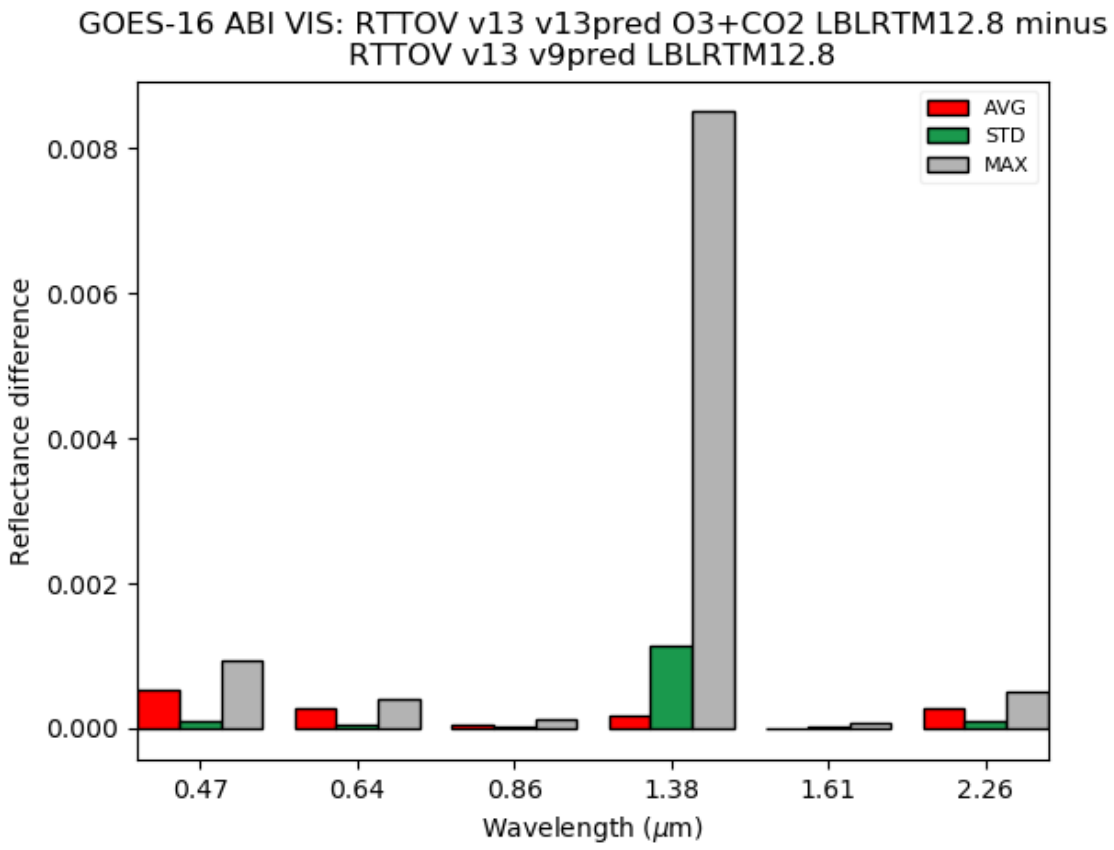

Figure 3.8.1: Differences in RTTOV v13 simulated reflectances for GOES-16 ABI visible/near-IR channels using v13 predictors (variable O_3+CO_2) and v9 predictors over the 83 profiles used for training RTTOV optical depth coefficients. Zenith angle is 50°, solar zenith angle is 30°, relative azimuth angle is 180°, and surface BRDF is 0.1.

3.8.2 Rayleigh single scattering

RTTOV v11 introduced a basic parameterisation to account for Rayleigh single scattering towards the sensor (R11REP2013). This is intended as a fast approximation which avoids the need for full multiple-scattering calculations. The implementation uses the parameterisation of the Rayleigh scattering cross-section from Bucholtz (1995) computed at the channel central wavelength and computes the Rayleigh source term by integrating the particle number density over each layer. An expression is obtained for this integral using the hydrostatic equation (equations 2.1.5, 2.1.7, 2.1.8 in R11REP2013). In addition, this

implementation included a water vapour dependence when computing the molar mass of the air in the layer.

The single scattering parameterisation used with the v13 predictor coefficients has been simplified: the parameterisation of the volume scattering coefficient is used directly instead of the scattering cross-section. This allows the pre-computed channel-average value to be used (as for the Rayleigh extinction described above), rather than the value computed at the channel central wavelength. The impact of the variability in water vapour was so small that this has been removed in the interests of simplicity and a fixed value for the molar mass of dry air is used instead.

The upwelling and downwelling Rayleigh source terms $J_i^{\uparrow}$ and $J_i^{\downarrow}$ respectively for layer *i* (bounded by levels *i* and *i*+1) for a given channel then becomes (cf equations 2.1.7 and 2.1.8 in R11REP2013):

$$J_i^{\uparrow/\downarrow}(\theta_{sat,i}, \theta_{sun,i}) = F_{sun}\tau_{sun,i}\frac{P\left(\Theta_i^{\uparrow/\downarrow}\right)}{4\pi}\frac{\mathrm{OD}_{\mathrm{ray}}}{\cos(\theta_{sat,i})} \quad (3.8.3)$$

where $\theta_{sat,i}$ and $\theta_{sun,i}$ are the local satellite and solar zenith angles in layer *i*, $\Theta_i^{\uparrow/\downarrow}$ are the local scattering angles for the upwelling and downwelling radiation, F_{sun} is the top-of-atmosphere solar irradiance, $\tau_{sun,i}$ is the transmittance from space to level *i*, $\mathrm{OD}_{\mathrm{ray}}$ is given in equation 3.8.2, and P is the azimuthally-averaged phase function:

$$P(\Theta) = \frac{3}{4}(1 + \cos^2\Theta) \quad (3.8.4)$$

for scattering angle Θ.

As noted above, the impact of the modified single-scattering calculation is included in Figure 3.8.1: the very small differences in ABI channels 1-3 demonstrate that the modified calculation is giving very similar results to the RTTOV v12 parameterisation.

3.8.3 Rayleigh multiple scattering

Rayleigh multiple scattering may now optionally be included in visible/near-IR cloud/aerosol scattering simulations when using RTTOV-DOM, the Discrete Ordinates Method solver (Hocking, 2016). The scattering optical depth is obtained as in equation 3.8.2 following Bucholtz (1995) and the phase function is the same as for the single scattering (equation 3.8.4).

Although the DOM solver is implemented for aerosol and/or cloud scattering, it is possible to run clear-sky Rayleigh multiple scattering calculations by setting up a cloud/aerosol simulation (it does not matter which) with input cloud/aerosol concentrations set to zero and

activating the Rayleigh multiple scattering option. It should be noted that the DOM solver is computationally expensive compared to other solvers in RTTOV and enabling the Rayleigh multiple scattering increases the run-time even further. As such this is intended primarily for off-line or research applications rather than operational processing.

This new capability has been used to generate new look-up tables (LUTs) for the MFASIS fast visible cloud solver (see Section 3.9) which yield top of atmosphere reflectances much closer to those generated using the libRadtran/DISORT model which includes Rayleigh multiple scattering as demonstrated in Figures 3.9.7 to 3.9.9. These plots show comparisons of the "old" RTTOV-DOM (no Rayleigh multiple scattering), updated RTTOV-DOM, and libRadtran/DISORT top of atmosphere reflectances: the new RTTOV-DOM calculations match those from libRadtran much more closely.

3.9 MFASIS for fast visible simulations in the presence of clouds

For the simulation of visible and infrared channels in the presence of clouds and aerosols, the Discrete Ordinates Method (DOM) has been introduced in RTTOV v12 to account for multiple scattering effects. DOM can provide accurate 1D radiative transfer solutions, but may be too slow for some operational applications like data assimilation. For this reason, the Method for Fast Satellite Image Synthesis (MFASIS) has been added as an additional fast model for visible channels in the presence of clouds with a first implementation in RTTOV v12.2 and further updates in RTTOV v12.3 and RTTOV v13. MFASIS is based on a compressed Look-Up-Table (LUT) approach and was initially developed using the DISORT implementation in the software package libradtran (Mayer and Kylling, 2005; Emde *et al.*, 2016). The following describes the MFASIS implementation within RTTOV. More details on the MFASIS approach can be found in Scheck *et al.* (2016).

3.9.1 General approach and implementation in RTTOV-12.2

MFASIS is intended for the fast simulation of satellite images in the visible spectral range in the presence of clouds. The focus is on non-absorbing or very weakly absorbing channels, for which atmosphere has only little influence on the top of atmosphere reflectance so that the clouds can be approximated by two layers: one water cloud layer and potentially an overlaying ice cloud layer. The reflectances are approximated by a function that depends on the eight parameters which have the strongest influence on the reflectance: vertically integrated optical depths and effective particle radii describing the cloud properties, the surface albedo and the viewing geometry characterized by the cloud top height, sun and satellite zenith angles and the scattering angle (see Fig. 3.9.1).

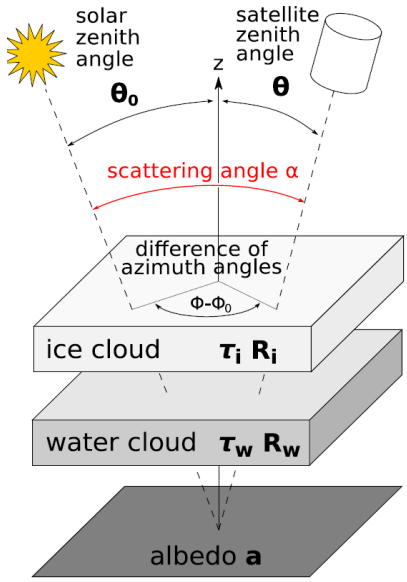

Fig. 3.9.1: Schematic view of the 8 parameters (three angles Θ_0, Θ, and α; four cloud related parameters τ_i, τ_w, R_i, R_w, and surface albedo a) used in the MFASIS LUT method.

Using these parameters an eight-dimensional reflectance LUT could be computed using DOM and interpolating in this LUT would already be a fast replacement for a DOM call. However, to keep the interpolation error in the reflectance below e.g. 0.01, the LUT would need to be about 8 GB in size, which will in general exceed the acceptable memory use for online operators. To reduce the LUT size significantly, a form of lossy compression is applied. The reflectance can be approximated well by a few terms of a 2D Fourier series in the zenith angle dimensions (see Scheck *et al*., 2016 for details). Instead of storing many reflectance values it is thus sufficient to store only a few Fourier coefficients in a LUT, which is only about 20 MB in size. The Fourier coefficients are computed by means of a least-squares fit to results calculated with RTTOV-DOM, so that the RTTOV implementation of MFASIS is a fast approximation to the more accurate, but significantly slower RTTOV-DOM model implementation.

Cloud parameters: The necessary cloud related parameters τ_i, τ_w, R_i, R_w are derived using the cloud water and cloud ice profiles from the input to RTTOV as well as the chosen settings in the options for cloud optical properties.

For cloud liquid water, either cloud liquid water properties and effective particle radii according to the OPAC cloud classification can be used or else the cloud liquid water properties are parameterised in terms of effective particle radii (D_{eff} option). In the case of the OPAC choice, the effective particle radii have fixed values for each of the five possible OPAC cloud (and cloud particle) types (Hess et al, 1998): Stratus Continental (7.33 µm), Stratus Maritime (11.30 µm), Cumulus Continental Clean (5.77 µm), Cumulus Continental

Polluted (4.00 µm), Cumulus Maritime (12.68 µm). In the D_{eff} scheme, the particle radii can be provided by the user or taken from the Martin *et al.* (1994) effective radii parameterisation (available from RTTOV v13, see section 3.4.1).

For cloud ice, the Baum ice properties (Baum *et al.* 2011), a parameterisation in terms of ice effective radii, are used. The Baran optical properties are not currently applicable to the MFASIS parameterisation as particle size is currently a fundamental input to MFASIS while there is no explicit size parameter for the Baran properties.

Surface albedo: The surface albedo is calculated as (π*BRDF), and values are capped at one to prevent unphysical albedo values being used. The BRDF values are taken from the input to RTTOV, which can in turn be from an RTTOV-internal sea BRDF model and a land surface BRDF atlas provided by RTTOV (Vidot and Borbas, 2014).

Limitations and flagging of situations: The current implementation simulates channels in the wavelength range of 0.47 – 0.86 µm with LUTs being available e.g. for SEVIRI, ABI and AHI channels in that range and LUTs are available corresponding to the different cloud optical property options described above. Currently, no trace gases or aerosols are considered and the simulations assume a plane-parallel geometry of the atmosphere. Also, being a 1D approach, the cloud geometry and a possible inclination of the cloud top is not taken into account, which results in the simulated images not having the typical bright and dark contours, especially at lower sun elevation. However, an approach for an inclusion of the cloud top inclination effect has been developed (Scheck *et al*., 2018) and will be added in later RTTOV versions.

It should be noted that since the LUTs for MFASIS in RTTOV are trained using RTTOV-DOM, the implementation in RTTOV v12.2 and RTTOV v12.3 does not explicitly treat atmospheric Rayleigh scattering, so that the interaction between Rayleigh scattered radiation and clouds is not taken into account by either RTTOV-DOM or MFASIS. This is different in RTTOV v13 (see below).

Despite MFASIS being able to simulate a vast range of conditions and viewing geometries, including the rainbow, to a good degree of accuracy, some situations are known to be less accurate and are indicated through output flags. Flags are set for situations outside of the LUT bounds and challenging viewing geometry situations, such as the satellite or solar zenith angles or the total optical depth or effective radius (for water and ice cloud) exceeding the LUT limits (see also RTTOV v13 User Guide). Note that the flags have been updated in RTTOV v13 (see below).

TL/AD/K: As for the other RTTOV components, MFASIS is available as a direct forward model as well as TL/AD/K models. Here the most computation-time consuming quantities (related to the LUT calls) are saved during the non-linear computations which makes the

subsequent use of the linear routines particularly efficient (see section 3.9.5 and Table 3.9.1). Note that due to the LUT approach, the linearized schemes are only piecewise continuous.

Treatment of mixed phase clouds: In order to keep the LUT size as small as possible, the atmospheric cloud column is described with the simplified two superimposed cloud layers. This approach achieves a good agreement between MFASIS and DOM when the ice cloud is located above the water cloud, but deviations are visible when ice and water clouds are at the same height. To cater for these mixed phase cloud situations without introducing additional LUT dimensions, the following preliminary approach has been implemented: Before the LUT call, it is checked whether and to which extent mixed phase clouds are present and, under certain conditions, the optical depth of ice cloud in the mixed layer ($\tau_{\text{mixed ice}}$) is added to the liquid water optical depth τ_{liquid} (and subtracted from the total ice optical depth τ_{ice}). More precisely, tests performed so far indicate that adding $\tau_{\text{mixed ice}}$ to τ_{liquid} is beneficial if (i) $\tau_{\text{mixed ice}} < \tau_{\text{mixed liquid}}$ and (ii) $\tau_{\text{ice}} < 0.3\ \tau_{\text{liquid}}$. However, to avoid strong discontinuities in the linearized code (TL/AD), the steps corresponding to conditions (i) and (ii) have been smoothed using a continuous function ((1+tanh)/2) which changes the portion of $\tau_{\text{mixed ice}}$ that is added to τ_{liquid} continuously from zero to one as the ratio $\tau_{\text{mixed ice}} / \tau_{\text{mixed liquid}}$ (and similarly $\tau_{\text{ice}}/(0.3\ \tau_{\text{liquid}})$) passes through the interval $[1-\Delta,1+\Delta]$. The choice of the transition (including the parameter Δ) can be tuned and will be adjusted further in the future based on more detailed global evaluations using different model outputs and observations.

3.9.2 Treatment of water vapour absorption (implemented in RTTOV v12.3)

For channels having weak, but non-negligible, water vapour absorption, like the 0.8 µm channel on SEVIRI, simulated reflectances are sensitive to the water vapour content in the atmosphere. In these cases, a linear correction is applied that accounts for different water vapour profiles and cloud top heights in the standard atmosphere (used for the LUT training) and model atmospheres. Note that in the future a non-linear dependency on water vapour contents will be implemented in order to be able to simulate channels with a stronger water vapour dependency of the reflectances with good accuracy.

Figure 3.9.2 illustrates the linear correction concept and shows the impact of adding water vapour above or below a water cloud for the SEVIRI 0.8 µm channel for relatively large zenith angles (solid lines). Adding 30 mm of water vapour above the cloud reduces the reflectance from 0.65 to about 0.5. Adding water vapour below the cloud has much less impact, but the reflectance still varies with the amount, as the water cloud considered here has an optical depth of 10 and is thus not completely opaque. Most of the water vapour dependency of the reflectance can be accounted for by a linear approximation (dashed

lines, see Eq. 3.9.1). Only for values larger than 40 mm, which occur only in the tropics, the reflectance error can become larger than a few 10^{-2}. It should be noted that the impact of the water vapour is significantly smaller for smaller zenith angles.

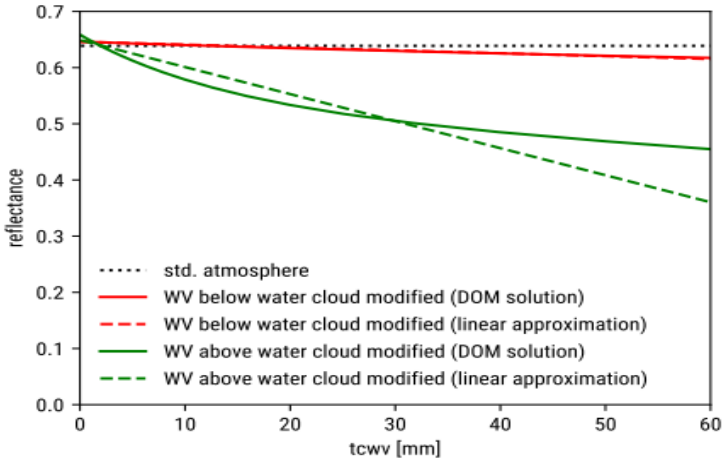

Fig. 3.9.2: Reflectance in the 0.8 µm SEVIRI channel for a water cloud with optical depth 10 computed with DOM for a solar zenith angle of 80° and a satellite zenith angle of 60° for different atmospheric water vapour contents. Dotted line: water vapour contents according to the standard atmosphere. Solid lines: variation of reflectance when the total amount of water vapour below (red) or above (green) the cloud is set to the value on the x-axis. Dashed lines: linear approximation according to Eq. 3.9.1.

The linear correction is applied by interpolating the reflectances between values from the standard LUT and two additional LUTs (technically combined in the same file) which have been computed for different water vapour contents (see Fig 3.9.3 for illustration):

$$r = r_{lut} + \frac{CWV_{gnd}^{mdl} - CWV_{gnd}^{lut}}{CWV_{high} - CWV_{gnd}^{lut}} \left(r_{gnd-high} - r_{lut}\right) + \frac{CWV_{wi}^{mdl} - CWV_{wi}^{lut}}{CWV_{high} - CWV_{wi}^{lut}} \left(r_{wi-high} - r_{lut}\right) \quad \text{(Eq. 3.9.1)}$$

$$CWV_{gnd}^{mdl} = \int_{gnd}^{ctw} N_{H_2O}\, m_{H_2O}\, dz \quad \text{(Eq. 3.9.2)}$$

$$CWV_{wi}^{mdl} = \int_{ctw}^{cti} N_{H_2O}\, m_{H_2O}\, dz \quad \text{(Eq. 3.9.3)}$$

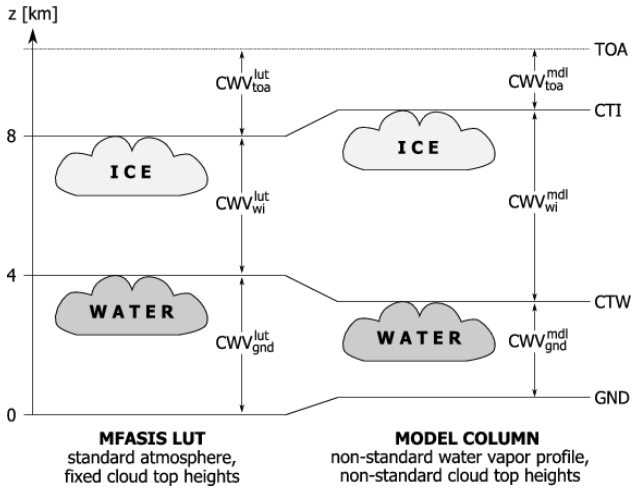

Fig 3.9.3; Schematic diagram illustrating the implementation of the linear water vapour correction (´gnd´ indicates the layer below the water cloud, ´wi´ between water and ice cloud and ´toa´ above ice cloud at top of atmosphere; 'lut' are values corresponding to the standard atmosphere used in the LUT and 'mdl' the values of the considered model atmosphere).

The standard reflectance r_{lut} is computed using a standard atmosphere for which column water vapour values of CWV^{lut}_{gnd} = 12.87 mm and CWV^{lut}_{wi} = 5.94 mm are present below the water cloud top and between water and ice cloud top heights, respectively. The water vapour content above the ice cloud,CWV^{lut}_{toa}, is assumed to be small enough to be neglected. $r_{gnd-high}$ and $r_{wi-high}$ are the reflectances computed using the high water vapour contents value $CWV_{high} = 30$ mm for the water vapour values below the water cloud (close to the ground) and between water and ice cloud which are pre-calculated in the additional two LUTs for the various cloud parameters, surface albedo and viewing conditions. The model water vapour contents CWV^{mdl}_{gnd} and CWV^{mdl}_{wi} are computed using not the standard MFASIS cloud top heights, but the actual cloud top heights detected in the model column. Therefore, not only deviations of the water vapour distribution from the standard atmosphere but also cloud top heights differing from the MFASIS standard values lead to a correction.

3.9.3 Comparison of MFASIS and RTTOV – DOM (RTTOV v12.3)

The following plots show the fit of the MFASIS reflectances to the RTTOV-DOM ones (used for training the MFASIS LUTs) using a set of atmospheric model profiles covering the whole SEVIRI disk.

Fig 3.9.4 shows histograms for the SEVIRI 0.6 µm and 0.8 µm channels as a function of the reflectance differences between MFASIS and RTTOV-DOM. For the 0.8 µm channel the top panels show the differences without the water vapour correction at the top and including the water vapour correction in the middle. With the water vapour correction, the large

differences are visibly reduced and the results for the 0.8 µm channel achieve similar quality to the 0.6 µm channel. Absolute reflectance differences remain mostly below 0.01, meaning that for clouds (i.e. not too low reflectances) the relative error is in the same range or smaller than the calibration uncertainty of imagers, which is typically a few percent.

Fig 3.9.5 shows results for the four AHI channels at 0.47 µm, 0.51 µm, 0.64 µm, and 0.86 µm for Himawari-8. The accuracy is comparable to the SEVIRI channels and results are similar for the corresponding channels on GOES/ABI. Note that AHI and ABI 0.86 µm channels are not corrected for variable water vapour. Their spectral interval is slightly different to the 0.8 µm SEVIRI channel which is relatively wide (0.74 – 0.88 µm) and the AHI and ABI 0.86 µm channels exhibit only negligible water vapour sensitivity.

Fig. 3.9.6 shows reflectance histograms simulated with MFASIS for the 0.6 µm channel of SEVIRI together with the reflectance distribution of the corresponding SEVIRI observations. The overall shape of the reflectances is reproduced well (in both RTTOV versions) despite noticeably fewer cases with low reflectances (below ~ 0.1) and somewhat larger numbers of reflectances above ~0.1. Note that this comparison of course not only includes inaccuracies of the MFASIS approach itself (i.e. in the fit to RTTOV-DOM), but also errors of RTTOV-DOM itself, errors in the assumed cloud properties (compared to properties of the real water and ice particles) and a potential mismatch between the cloud representation in the used ICON model and the real clouds. Also, the inhomogeneity of clouds was not taken into account, which could be important for radiation at global model resolutions (see e.g. Ahlgrimm & Forbes, 2016). For convective-scale models cloud inhomogeneity should have much less impact and a first case study (Scheck *et al.* 2020) indicates that systematic errors are sufficiently small for data assimilation. The differences between results obtained with RTTOV v12.3 and RTTOV v13 are due to the improved treatment of Rayleigh scattering in RTTOV v13 which results in an increase in reflectance in the latter case (see also discussion below).

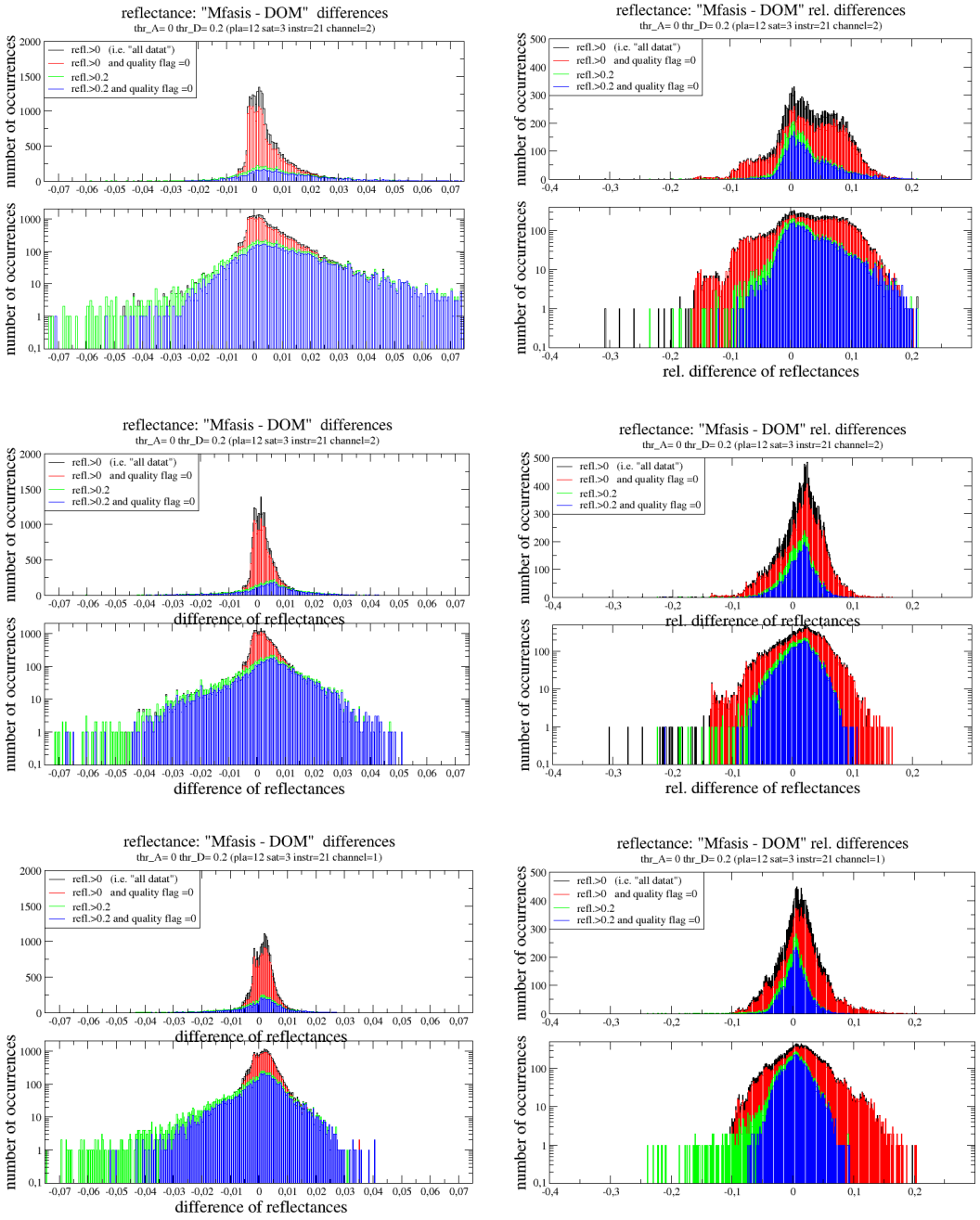

Fig 3.9.4: Top/middle: Histograms of differences between MFASIS and RTTOV-DOM reflectance simulations for SEVIRI channel 2 (0.8 µm) without (top) and with (middle) water vapour correction. Absolute and relative differences in left and right hand sub-panels, and with linear and log-scales in top and bottom sub-panels. Bottom four panels: Similar to top panels but for SEVIRI channel 1 (0.6 µm). Black curves: all data, green and blue: DOM reflectance > 0.2, red and blue: data with quality flag raised excluded.

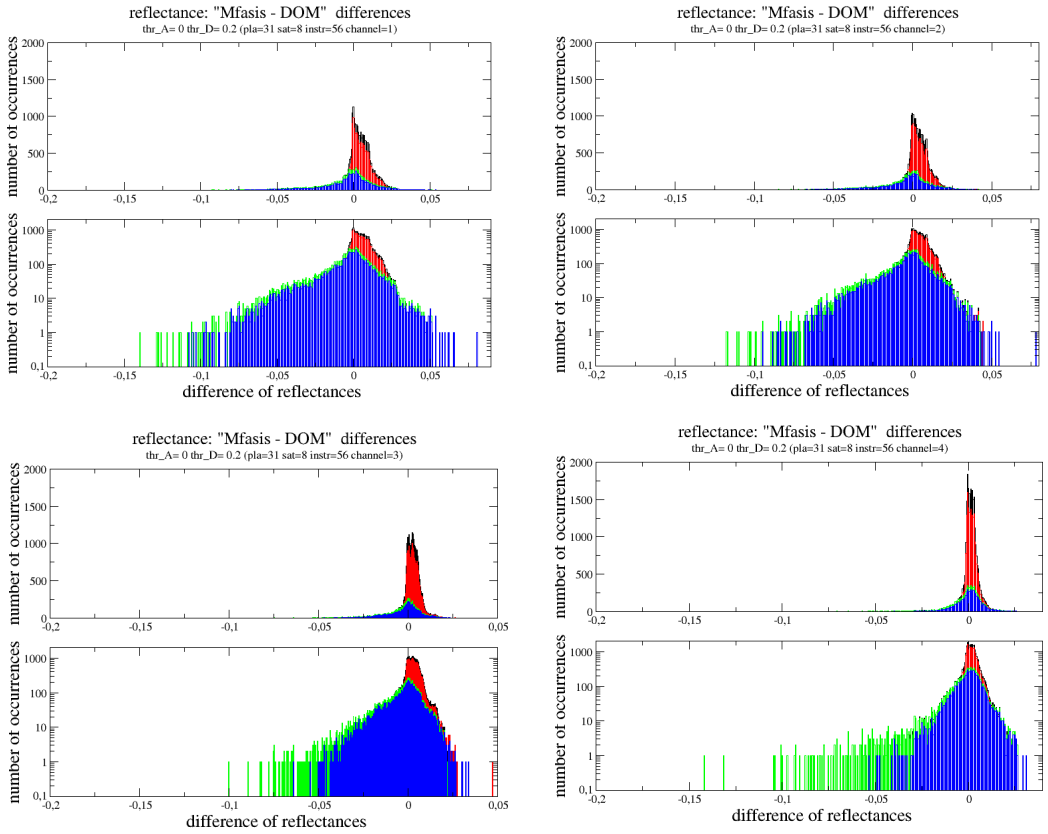

Fig 3.9.5: Like Fig 3.9.4, but for channels 0.47 µm (top left panels), 0.51 µm (top right panels), 0.64 µm (bottom left panels), 0.86 µm (bottom right panels) of Himarawi-8 AHI.

3.9.4 MFASIS updates in RTTOV v13

RTTOV v13 improves the treatment of Rayleigh scattering in RTTOV-DOM by including multiple scattering processes (see also section 3.8). This leads to visible improvements also for MFASIS based on LUTs trained using the updated RTTOV-DOM model. Improvements can be seen both in comparison to RTTOV-DOM and to an independent implementation of the discrete ordinates method in the radiative transfer library libradtran (DISORT or LR-DOM in the figures below; Emde *et al*., 2016). Note that whilst the full Rayleigh scattering increases the computational cost for RTTOV-DOM significantly, the computational cost for RTTOV-MFASIS remains unchanged.

Figures 3.9.7 to 3.9.9 show the dependence of simulated reflectances for the SEVIRI 0.6 µm channel on the scattering angle, the total column water and ice content, and the surface albedo for idealised atmospheric profiles under two viewing geometries. In all cases, the deviations between MFASIS and DOM are reduced for RTTOV-13 in comparison to RTTOV-12.

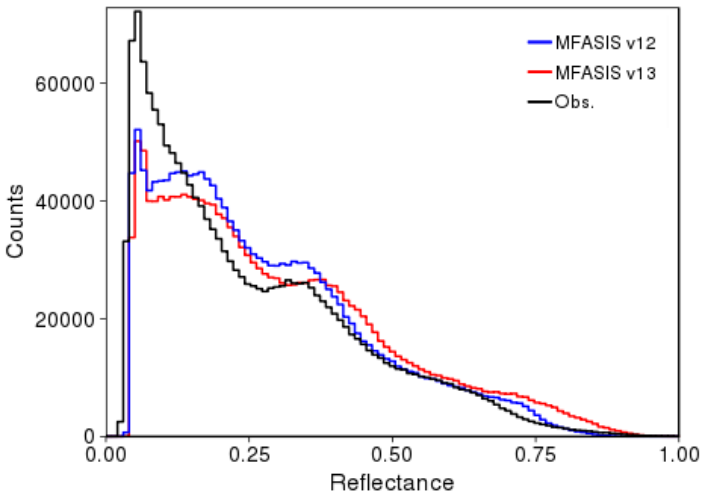

Fig. 3.9.6: Reflectance histogram for the 0.6 µm SEVIRI channel simulated using MFASIS (RTTOV v12.3: blue line; RTTOV v13: red line) and global ICON profiles (DWD) in comparison to observed reflectances (black line). Statistics are based on observations of Meteosat-11 between 24-30 September 2018 at 9, 12 and 15 UTC.

At the same time the agreement of both MFASIS and RTTOV-DOM with libradtran reflectances are noticeably improved due to the inclusion of Rayleigh multiple scattering in RTTOV-DOM v13 (see Section 3.8.3).

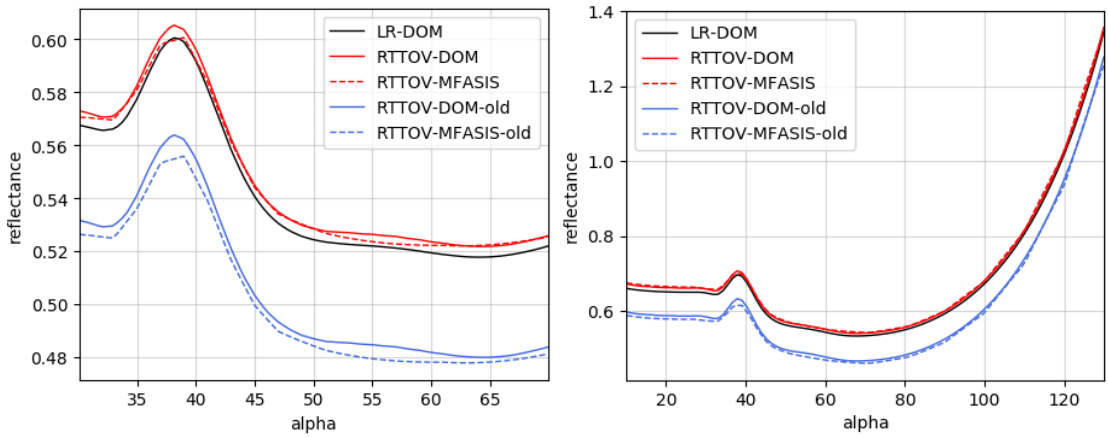

Fig. 3.9.7: Reflectance as a function of the scattering angle for a medium thick water cloud (tcwc = 0.1 kg/m^2, R_w = 10 µm) over a surface with a=0.1 for SEVIRI 0.6 µm for two viewing geometries (left: Θ=50°, $Θ_o$=20°; right: Θ=60°, $Θ_o$=70°). Black line: DISORT in libradtran, Solid lines: RTTOV-DOM, dashed lines: MFASIS; with red lines for RTTOV v13, blue lines for RTTOV v12.3 implementations.

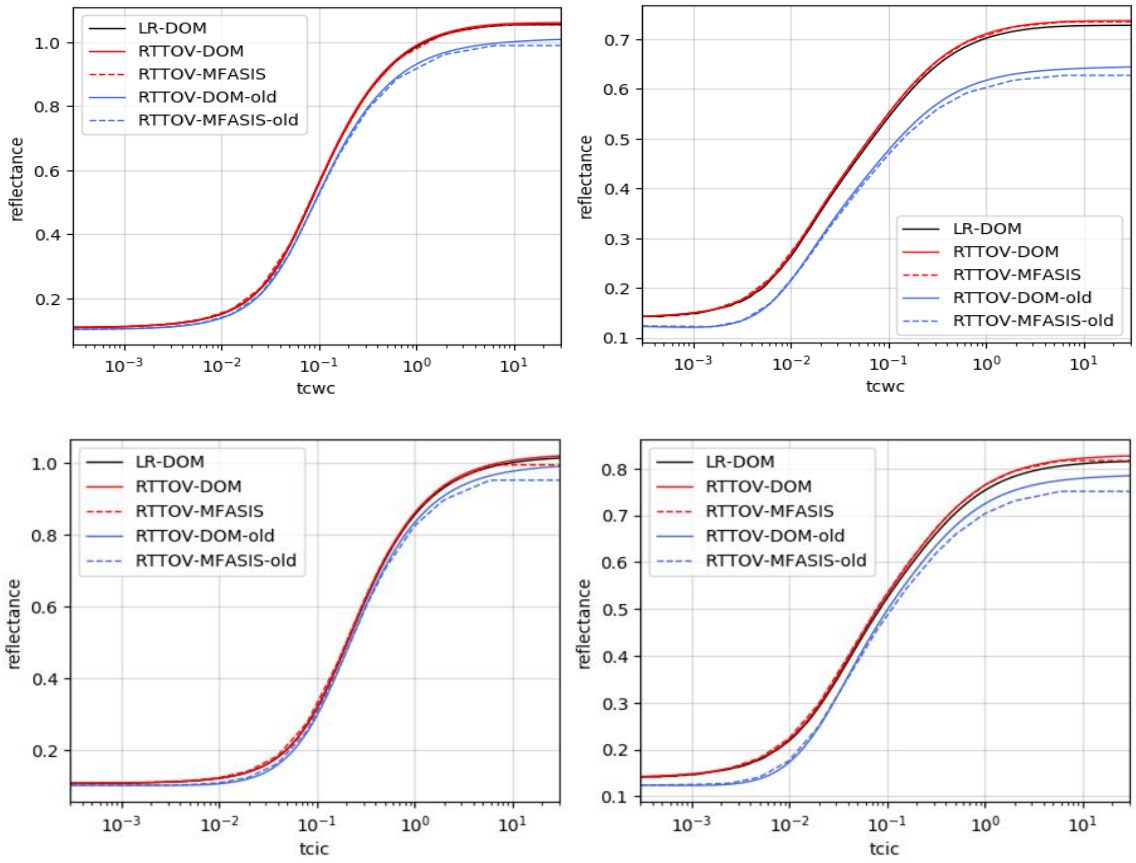

Fig. 3.9.8: As Fig 3.9.7, but for reflectance as a function of total cloud water content (top, Rw = 10 μm) and total ice water content (bottom, Ri = 30um) for two viewing geometries Θ=10°, Θo=20°, α=15° (left) and Θ=60°, Θo=70°, α=45° (right).

The improvements are most prominent in challenging situations, e.g., for atmospheric profiles with thick clouds (large tcwc or tcic in fig. 3.9.8), for viewing geometries with large zenith angles (as in the right plots of figs. 3.9.7 to 3.9.9), or in regions with large surface albedos (in fig. 3.9.9). In these cases, the interaction of Rayleigh scattered photons with cloud particles is particularly important.

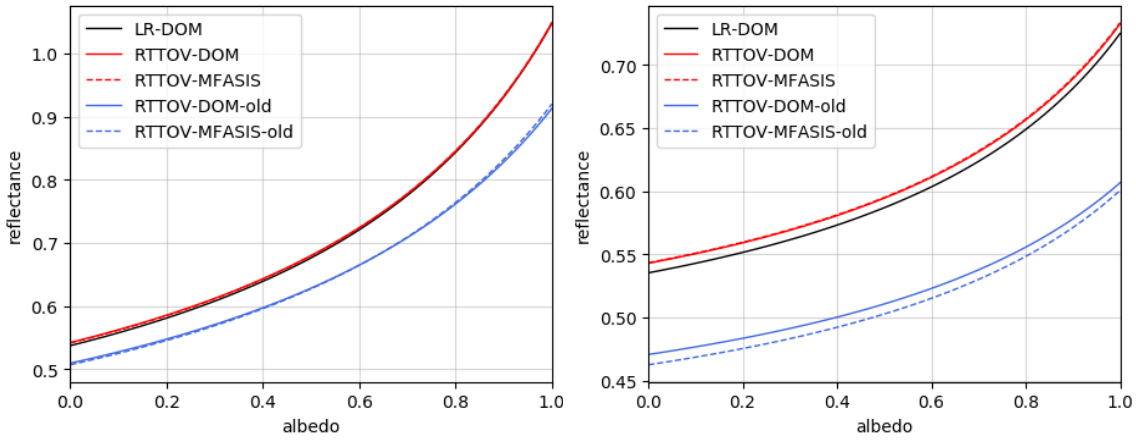

Fig. 3.9.9: As Fig 3.9.8 but for reflectance as a function of surface albedo for a medium thick water cloud (tcwc=0.1kg/m^2, R_w = 10µm).

Fig. 3.9.10 shows an MFASIS simulation of SEVIRI 0.6 µm channel reflectances for a full Meteosat disc for RTTOV-DOM and MFASIS (top) and the reflectance differences (bottom). Generally, the differences are small and hardly exceed 0.01 over most of the disc, apart from the disc edges with more extreme viewing geometries. This is consistent with the validation displayed in Fig. 3.9.4 (bottom, for RTTOV v12 and v12.3) and generally deemed small enough for quantitative applications of MFASIS given the large uncertainty in simulated cloud fields (and their parameters) themselves.

Note that many observations with larger MFASIS deviations are flagged (marked blue in bottom right plot) due to table limits being exceeded. Also, larger deviations very close to the disc edge are in most cases not a practical issue, because those observations are unlikely to be quantitatively used due to the drop in real pixel resolution and the extreme slant viewing conditions. The visible ring like structure with varying near zero and slightly positive deviations is linked to the Fourier series decomposition in zenith angles describing the viewing geometry, but overall the deviations are very small. Some cloud situation dependency of deviations can also be seen in this image simulation, e.g. occasionally low stratus display slightly more positive biases and small negative deviations occur for some high ice clouds. Such dependencies of the accuracy of simulated reflectances on atmospheric and cloud situations are the subject of ongoing studies with the aim to further improve the MFASIS approach where possible.

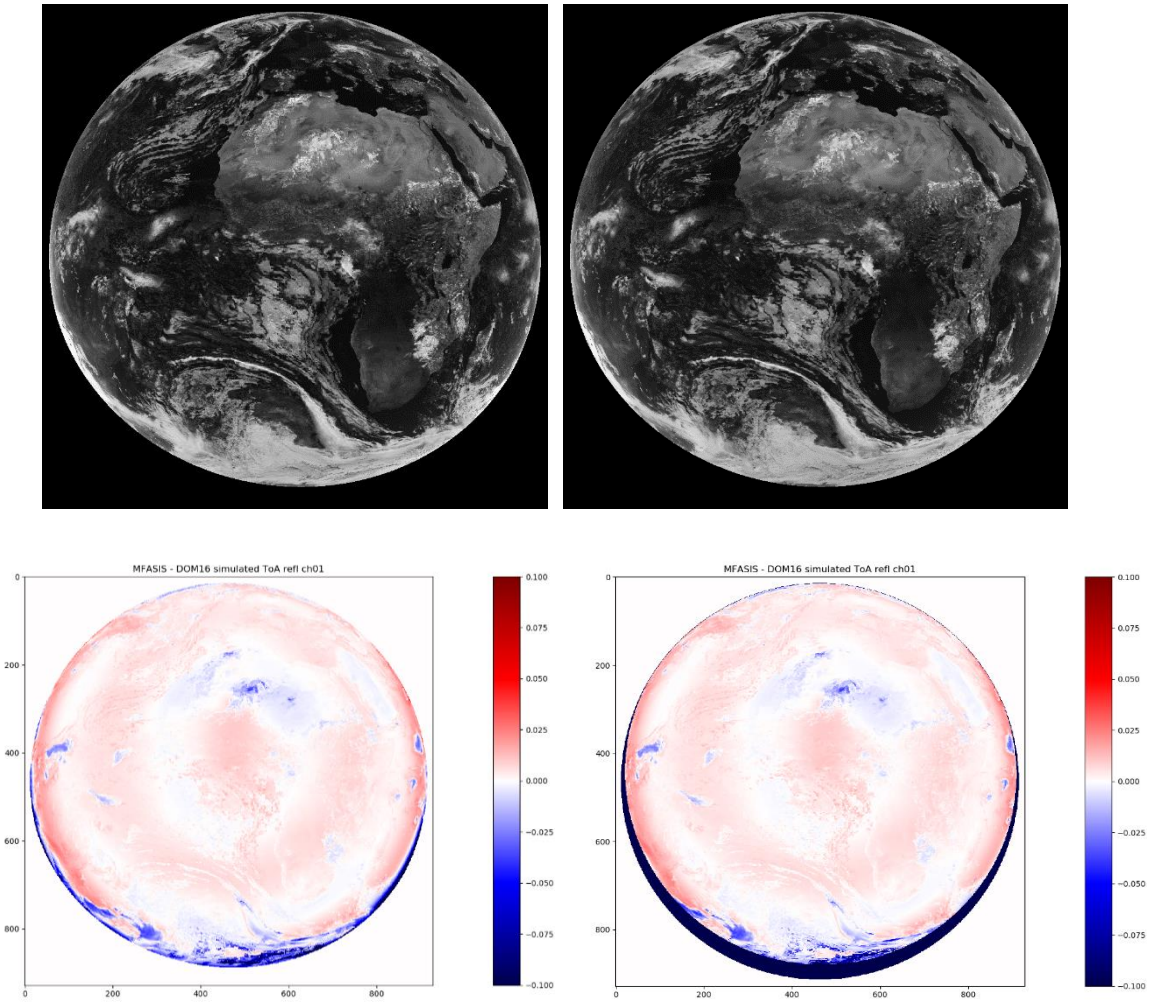

Fig. 3.9.10: Top: Simulation of SEVIRI 0.6 µm reflectances with RTTOV-DOM (16 streams with full Rayleigh scattering, left) and MFASIS (right) for 24 June 2020 12 UTC based on Met Office UM model fields. Bottom: Reflectance difference (bottom left) and differences showing pixels flagged by RTTOV-MFASIS (marked dark blue, bottom right). In this case flags result from the allowed viewing geometry limits being exceeded.

Technical improvements: The situation flagging has been updated so that the profile viewing geometry is checked against the actual limits applied in the LUTs (i.e. the training limits), in contrast to previous RTTOV versions where fixed minimum and maximum values were used. This allows for more flexibility for expanding MFASIS to new instruments, where the current standard LUT limits need modification, e.g., if the range of scattering angles needs to be extended further into the backscatter region. The implemented quality flags include checks for the viewing satellite or solar zenith angle exceeding the LUT limits, the sum of zenith angles exceeding a maximum value (the minimum of twice the zenith angle

LUT limit and 150 degrees) and the scattering angle exceeding the LUT limits. Additionally, the situation flagging has been relaxed for the profile optical properties (optical depths and effective particle radii of both water and ice clouds) so that the flagging is rather a test for an expected reduced accuracy of the results than a test for the LUT limits. Since the LUTs always cover an extensive range of optical depths up to a maximum value where reflectances are saturated (with consequently negligible effects on the accuracy when the LUT limits are exceeded), no flags are set for optical depths in RTTOV v13. The effective particle radii are checked against the minimum value in the LUT (as in previous versions) and the RTTOV maximum water and ice particle sizes (new in RTTOV v13). These may exceed the LUT limits but no visible reduction in the quality of the results could be found in this case.

The MFASIS fast visible cloud parameterisation can now be run in the same call as IR cloud simulations (previously thermal radiation was turned off in all channels for MFASIS simulations). In this case, solar radiation is only included for those channels supported by the MFASIS look-up table (LUT). Therefore, any non-thermal channels not supported by the MFASIS LUT will have zero radiances on output and solar radiation will not be included for SWIR channels. MFASIS runs no longer set the *plane_parallel* output flag in the *rttov_radiance* structure.

3.9.5 MFASIS speed

The simulation times using MFASIS and RTTOV-DOM have been compared for both RTTOV v12 and RTTOV v13 in a standardised setup running RTTOV single-threaded on an Intel Xeon @ 2.6 GHz processor for a single artificial profile for both SEVIRI channels (0.6 µm and 0.8 µm), repeating the computations many times to average out random fluctuations (compilation used ifort-openmp flags). This results in ~25s for 100000 profiles simulating both channels with MFASIS (and 39s for the AD code) to give an impression of run times.

	MFASIS relative to RTTOV-DOM	
	RTTOV - 12	RTTOV - 13 (with multiple Rayleigh scat)
DIRECT	11 times faster	244 times faster
TL	22 times faster	444 times faster
AD	174 times faster	25641 times faster
K	174 times faster	23902 times faster

Table 3.9.1: Speed-up factor of MFASIS relative to comparable RTTOV-DOM runs (i.e. 16 streams; full Rayleigh scattering for RTTOV-v13, no Rayleigh multiple scattering for RTTOV v12). The RTTOV v12 (RTTOV v13) runs use v9 (v13) optical depth predictors; MFASIS and RTTOV-DOM here with OPAC CLW properties.

Table 3.9.1 summarizes the speed-up factors of MFASIS calculations w.r.t comparable RTTOV-DOM runs (including full Rayleigh scattering for RTTOV v13, i.e. the setup used to train MFASIS). RTTOV v13 MFASIS direct calculations are ~240 times faster than the corresponding RTTOV-DOM runs (~11 times faster for RTTOV v12 which does not include Rayleigh multiple scattering). A broadly similar magnitude of speed gain was noted in the

full disc calculations done for Fig 3.9.10 for a realistic range of atmospheric profiles (using a single thread on the same hardware as above). There, a speed gain factor of ~390 could be achieved, the whole disc simulation taking ~2 min. with MFASIS and ~13 hours with RTTOV-DOM.

The difference for the adjoint or K-code runs is even significantly higher, the AD of MFASIS being ~25600 times faster than the AD of RTTOV-DOM. This results from the added complexity of the full Rayleigh computations in DOM, but also from a further speed-up achieved in MFASIS itself for RTTOV v13 (see below). TL/AD/K runs for MFASIS now take ~ 36s/39s/41s for 100000 profiles

When comparing MFASIS for the SEVIRI 0.6 µm and 0.8 µm calculations to RTTOV v13-DOM without Rayleigh scattering switched on, MFASIS direct is ~ 30 times faster compared to the ~11 times for RTTOV v12. This provides a further MFASIS speed-up in RTTOV v13 compared to RTTOV v12 which was achieved by optimising the LUT calls, so that each interpolation in one LUT takes of the order of 10^{-6} s. This results in a speed-up by a factor of four for channels without water vapour correction (e.g. SEVIRI 0.6 µm) to a factor of two for channels with water vapour correction (e.g. SEVIRI 0.8 µm). Since parts of the computations for the TL/AD/K models are already carried out and stored in the direct model (which is called within the TL/AD/K call), this optimisation also results in a speed-up of the TL/AD/K models in the RTTOV v13 implementation.

3.10 CAMEL Climatology Surface Emissivity Atlas

RTTOV v13 now includes a third choice for IR land surface emissivity atlases. The previous, University of Wisconsin UWIRemis atlas (first included in RTTOV v10, Borbas and Ruston (2010), Borbas *et al.*, (2018), Feltz *et al*., (2018), and the CAMEL 2007 atlas (first included in RTTOV v12.1, R12REP2017) are based on data from the selected year of 2007. This single year was chosen due to its high quality and more representative of the CAMEL emissivity climatology mean than other individual years; however, it is advantageous to update the module so that it is based on the actual, full CAMEL climatology.

This third choice for IR land surface emissivity atlas is called CAMEL CLIM atlas and is based on CAMEL V002 PC coefficient data (Hook, 2017) with an advanced snow correction. It was calculated for the 16+ year time period 2000 to 2016 on a spatial grid of 0.05 degrees (about 5 km x 5 km). Additionally, the mean and the variance of the IR emissivity has been updated based on the CAMEL V002 data and provided with a higher spatial resolution (0.25x0.25 degree vs. 0.5x0.5 degree). This climatology can be degraded to NWP model resolutions to make it suitable for a first guess to the land surface emissivity for 1D-Var data assimilation of infrared sensor data. The updates in the “CAMEL CLIM” V002 IR emissivity module of RTTOV v12.3 are summarized in Table 3.10.1. In general, the main updates include the use of CAMEL V002 which includes an improved representation of fractional

snow cover by introducing two additional laboratory datasets in the PCA regression and the use of the climatological mean over the 2000-2016 time period in place of the single year 2007 used previously.

To obtain the climatological PC coefficients, the multi-year average of the CAMEL PC coefficients is computed for each calendar month (January-December). In computing the average, however, the coefficients corresponding to unique combinations of number of PCs used and lab dataset version need to be kept separate. From each unique set of coefficients an HSR emissivity spectrum can then be computed.

	RTTOV12	***RTTOV12.3***
EmisDB:	2007 CAMEL V001	2000-2016 CAMEL V002 CLIMATOLOGY
Spatial Res:	0.05°x0.05°	0.05°x0.05°
Inputs:	UWIREMIS BF (10) ASTER-GED (5) MODIS-ASTER Lab Data	CAMEL V002 2000-2016
Method:	Conceptual hinge-points Method PCA regression	Conceptual hinge-points Method PCA regression
Lab data:	Three sets of MODIS/ASTER: 55 general set 82 general+carbonates 4 ice/snow	Five sets of MODIS/ASTER: 55 general set 55 general set + 4 ice/snow 82 general+carbonates 82 general+carbonates+ 4 ice/snow 4 ice/snow
Covariances	Mean and Stdev of the Uwiremis Database 0.5x0.5deg 2003-2006	Mean and Stdev of the CAMEL V002 Database 0.25x0.25deg 2000-2016
Outputs	Emissivity and error covariance matrix on instrument spectral grid	Emissivity and error covariance matrix on instrument spectral grid

Table 3.10.1: Summary of the status of the CAMEL CLIM emissivity module as incorporated into RTTOV.

The HSR emissivity spectra from each unique set are then combined by a weighting based on the number of years of each type to obtain the multi-year climatological mean. Figure 3.10.1 demonstrates how the CAMEL climatological emissivity spectra are derived for the month of January over a selected location in Northern Wisconsin. It is located within the sub-boreal forest zone with the most common winter land cover (lab version 9). In January, three types of lab versions are identified during the 16 years of time period: V12-snow/ice only, V8-general vegetation cases, and V9–combined snow/ice plus general vegetation

cases. Figure 3.10.1 shows the average HSR spectra for each lab version and the corresponding weighting in the multi-year average which occurred over the 16+ years of the CAMEL record. The weighted average of the corresponding HSR spectra is used to calculate the final climatological emissivity spectra.

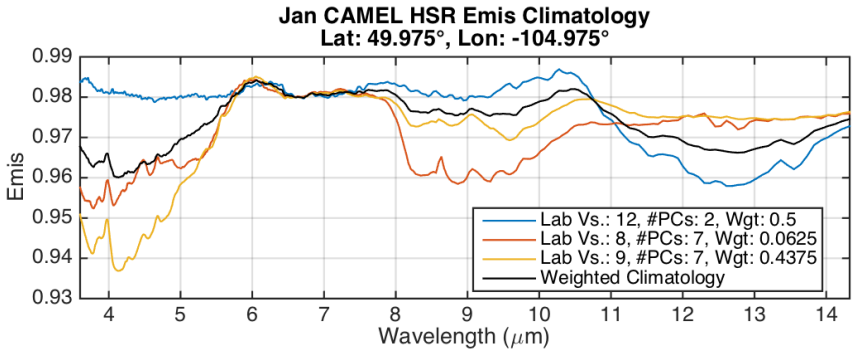

Figure 3.10.1: CAMEL climatological emissivity spectra (black) for the month of Jan over a selected location in Northern Wisconsin. The three HSR spectra are also shown for the three types of lab versions (V12-snow/ice only (blue), the V8-so called general vegetation case (red), and the V9–combined snow/ice and general cases (orange)), which occurred over the 16 years and used to calculate the climatological spectra. Their weights (Wgt) and number of PCs (#PCs) used are also shown in the legend.

The differences between the CAMEL and the CAMEL climatology is presented on the timeseries of Figure 3.10.2 over a Rocky Mountain test location at Mt. Massive, Colorado. The CAMEL monthly climatology is repeated for each year. MODIS Snow Fraction, ASTER NDVI, and lab version with the number of PCs used are also presented. Large seasonal variations can be seen in certain channels, which are due to the sensitivity to basalt mineral exposed by melting snow in Spring and Summer. Emissivities reflect snow/ice signatures (lab V12) during Winter and Fall, while in the Spring and Summer they reflect bare soil/rocks (lab V8) and mixed with snow (V9), showing the dynamics of annual snow cover and snow-melt over basalt minerals across the region. The artificial decrease/increase and jump at January 2007 due to the prepossessing settings, safe hold mode and cross talk error of MODIS bands, in addition to the four case day simulation evaluation reported in (Borbas and Feltz, 2019), demonstrates that the CAMEL CLIM emissivity module is preferable and advantageous in comparison to the previous two modules (UWIREMIS and CAMEL), which are based on one selected year (2007) of the database.

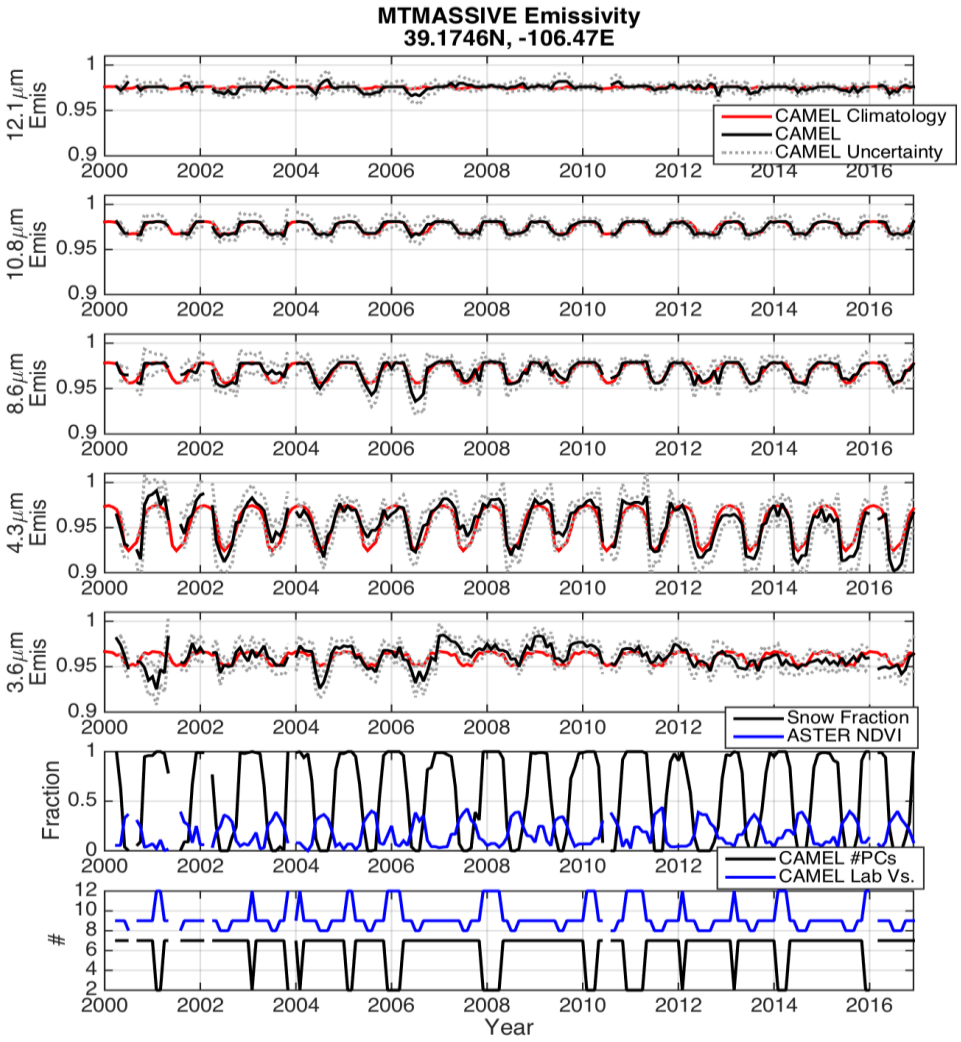

***Figure 3.10.2**: Timeseries of CAMEL (black) and CAMEL climatology(red) with uncertainty (dotted line) over Mt Massive, Colorado between 2000 and 2016. The CAMEL monthly climatology is repeated for each year. MODIS Snow Fraction, ASTER NDVI, and lab version (Vs) with number of PCs (#PCs) used is also plotted on the bottom two panels.*

3.11 Updates to RTTOV-SCATT

3.11.1 Scientific bugfix to downward scattering terms

RTTOV-SCATT uses a delta-Eddington solver to compute the scattering source terms in the radiative transfer equation. This is then integrated along the ray path downwards to the surface, the surface interaction is computed, and the ray path is then integrated up to the sensor. Since it was first coded (Bauer *et al*., 2006, see also RTTOV v8 SVR, R8REP2006) there has been a scientific error in the downward source terms. The error was spotted by

Hejun Xie (personal communication, 2020). It originates in an incorrect treatment of the source function (Bauer eq. A5) for downward angles, where the cosine of the zenith angle μ becomes negative. This error only impacts the source terms in the ray integration (Bauer eq. A17):

$$J^+ = J_a^+\alpha^+ + J_b^+\beta^+ + J_c^+\gamma^+ + J_d^+\delta^+$$

$$J^- = J_a^-\alpha^- + J_b^+\beta^- + J_c^+\gamma^- + J_d^+\delta^-$$

Here the index *i* has been dropped for clarity. The $J_a^{+/-}$ to $J_d^{+/-}$ terms were correct in the code, as were α^+ to δ^+. However for the downward source term J^-, the values of α^- ,$\gamma^-$and δ^- were incorrectly set to the values of α^+, γ^+ and δ^+. In the new code, replacing Bauer's equation A18:

$$\alpha^+ = B_0 - \frac{3\ g\ \omega_0 \mu B_1}{2h}$$

$$\beta^+ = B_1$$

$$\gamma^+ = D^+\omega_0\left(1 - \frac{3g\mu\Lambda}{2h}\right)$$

$$\delta^+ = D^-\omega_0\left(1 + \frac{3g\mu\Lambda}{2h}\right)$$

$$\alpha^- = B_0 + \frac{3\ g\ \omega_0 \mu B_1}{2h}$$

$$\beta^- = B_1$$

$$\gamma^- = D^+\omega_0\left(1 + \frac{3g\mu\Lambda}{2h}\right)$$

$$\delta^- = D^-\omega_0\left(1 - \frac{3g\mu\Lambda}{2h}\right)$$

Bauer *et al.* (2006) explains the meaning of the symbols in these equations. Note that eq. A18 of that paper has an additional typo: the equations for γ and δ are missing the factor 3. However there was no corresponding mistake in the code (there are many other typos in the Bauer (2006) equations, but the code has always been correct in these other cases). What the error amounts to is a reversal of the plus and minus signs in α^- ,$\gamma^-$and δ^- as compared to α^+, γ^+ and δ^+. The error is likely to be important in areas where the bulk single scattering albedo ω_0 is significant and where the bulk asymmetry parameter g is non-zero, in other words where forward and backscattering is balanced. Outside of scattering, $\omega_0 \rightarrow$

0, term $\frac{3\,g\,\omega_0\mu B_1}{2h}$ should become small relative to B_0 and $\alpha^+ \rightarrow \alpha^-$. Similarly the $\gamma^+, \delta^+, \gamma^-$ and δ^- terms should likely become small, although due to the complexity of the source functions this is hard to analyse analytically. Finally the error is likely to be most important where the reflected downward beam has a significant impact on the measured brightness temperature, in surface-sensitive channels rather than sounding channels, and where the hydrometeor optical depth is low enough to provide surface visibility. Generally these expectations are backed up by the practical results in the next paragraphs.

Channel	Frequency [GHz] and polarisation (v=vertical, h=horizontal)	Maximum change in simulated brightness temperature [K]
1	50.3 h	-0.17
2	52.8 h	-0.03
3	53.6 h	-0.03
8	150 h	-1.11
9	183+/-6.6 h	-0.23
10	183+/-3 h	-0.05
11	183+/-1 h	-0.005
12	19 h	-0.06
13	19 v	-0.04
14	22 v	-0.05
15	37 h	-0.22
16	37 v	-0.13
17	92 v	-0.39
18	92 h	-0.69

Table 3.11.1: Maximum difference in simulated brightness temperatures with the downward source term bugfix minus the control, for a representative global sample of all-sky SSMIS observations.

The effect of the scientific bugfix is shown in Table 3.11.1 for the SSMIS observations simulated by the IFS for two data assimilation cycles on 13th June 2019 (the background model state remains fixed in both the control and the experiment). The table shows the maximum change in the brightness temperature in each channel, and does not include those channels where there was no significant change, e.g. less than $1e^{-3}$ K. As expected theoretically, the bug fix has a larger effect in surface sensitive channels than in sounding channels (e.g. channel 1 vs 2, or 8 vs. 9) and has a larger effect in h-polarised channels compared to v-polarised, due to the ocean surface being considerably more reflective (e.g. channel 18 vs. 17). The effect is also larger at higher frequencies where scattering is a more important aspect of the radiative transfer.

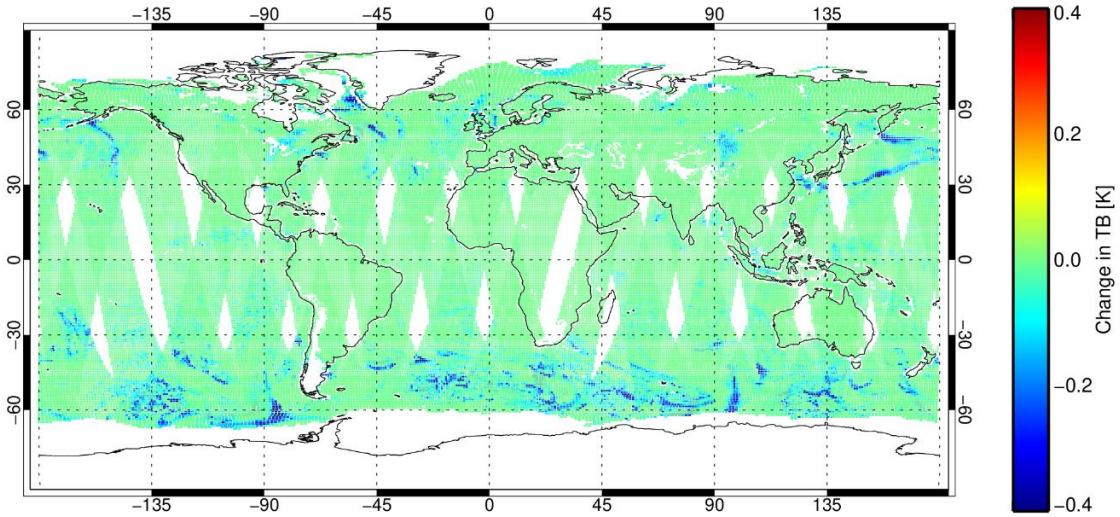

Figure 3.11.1: Difference in simulated 92 GHz h-polarised brightness temperatures with the downward source term bugfix minus the control, for all-sky SSMIS observations from 21 UTC on 12th June 2019 to 21 UTC on 13th June 2019. Sea-ice and some snow-affected areas are excluded.

Figure 3.11.1 shows a map of the changes in channel 18 (92h) which is the second most strongly affected channel and has been chosen over 150h because it has surface sensitivity globally, whereas 150h does not see the surface in the tropics. The effect is generally much smaller than the maximum and is largest at high latitudes in frontal systems where snow particles are expected to generate a significant amount of scattering. There are smaller effects in some subtropical areas, in clouds that are unlikely to be deep or glaciated, suggesting the problem has a minor effect in situations of scattering from rain (this may change in future if scattering models for rain are chosen that have significant asymmetry; currently the Mie sphere is used). However, there is no effect in the deep convection of the ITCZ, because strong extinction in these areas blocks visibility of the surface.

An 80-day cycled data assimilation experiment was run with the IFS and showed no discernible impact of the change on the verification (e.g. no statistically significant changes to the fits to other observations, or changes to forecast scores).

3.11.2 Reduced minimum cloud fraction threshold

In previous versions of RTTOV-SCATT, for any effective cloud fraction less than 0.05, the effect of cloud and precipitation on the brightness temperatures was ignored: RTTOV-SCATT returned the clear-sky brightness temperature. This approach likely had two origins: as a performance optimisation intended for data assimilation; and because of historical concerns over the widespread trace cloud amounts that can be generated by forecast models. In v13, the minimum cloud fraction has been set to 0.001 the performance

optimisation is no longer needed, and the decision on whether trace cloud amounts are realistic should be left to the user.

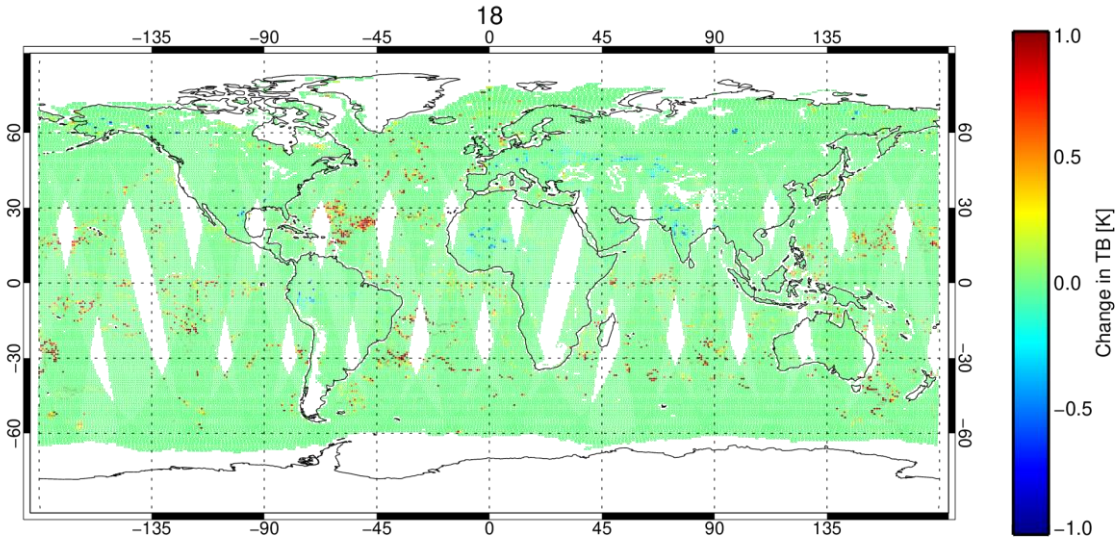

Figure 3.11.2: Difference in simulated 92 GHz h-polarised brightness temperatures with min_frac=0.001 as in RTTOV-SCATT v13, minus a control with min_cfrac=0.05. This is based on all-sky SSMIS observations from 21 UTC on 12th June 2019 to 21 UTC on 13th June 2019. Sea-ice and some snow-affected areas are excluded.

Figure 3.11.2 shows the effect on simulated SSMIS 92 GHz h-polarised TBs. The effect is mostly contained within +/- 1K and is mostly found in scattered areas of the subtropics, away from any of the intense cloudy regions such as the ITCZ convection or midlatitude frontal systems (such as those highlighted in Fig. 3.11.1). These all must be areas with effective cloud fractions less than 0.05, which could occur in maritime cumulus or on the edges of more extensive cloud systems. Around 8% of observations are affected. Within the sample that has changed, around 50% are barely affected (absolute changes < 0.1K) and only 0.1% of scenes are changed by more than 2K. The maximum change was -8.4K in one deep convective scene over the central U.S., where the effective cloud fraction was 0.0499. All other cloud-sensitive channels are affected in corresponding ways, but the effect is greatest at 92 GHz.

Full cycling data assimilation tests have not been carried out, but there are promising indications in the passive monitoring fits over a 21-day period. The standard deviation of O-B for cloud-sensitive channels from 19 to 166 GHz (e.g. GMI, AMSR2, SSMIS) was typically reduced by around 0.05%; in 183 GHz channels (SSMIS, MHS, MWHS2) the standard deviation was increased, but only by 0.005% (in most cases these changes are statistically significant). Given the double penalty effect usually penalises the addition of cloud in the

simulations, the reduction of O-B in imaging channels suggests this is a genuine small improvement to the realism of the simulation. The effect in models other than the IFS is likely to depend on the typical sub-grid cloud structures that they generate.

3.11.3 Approximate treatment of polarised scattering from oriented ice particles

The preferential orientation of hydrometeors in the atmosphere leads to differences in scattering properties as a function of polarisation and viewing angle. This effect is thought to come from frozen hydrometeors rather than rain, and it leads to brightness temperature differences of up to around 10 K between the vertically and horizontally polarised channels of GMI at 166 GHz, particularly in the anvil regions of convection (Gong and Wu, 2017). Although RTTOV-SCATT does not do fully polarised radiative transfer, a simple way to approximate the effect is to increase extinction from ice species in horizontally polarised channels and to reduce it in vertically polarised channels (Barlakas *et al*., 2020). This is quantified by the ratio of extinction in the *h* channel over that in the *v* channel. By optimising measures of fit between GMI observations and IFS-simulated brightness temperatures, Barlakas *et al*. found a polarisation ratio of 1.4 was appropriate at 166 GHz and 1.5 at 89 GHz. With this approach, RTTOV-SCATT was able to do a reasonable job of simulating the polarisation characteristics observed in GMI data. A novel implication is that scattering effects will be observed differently by sensors with mostly *v*-polarised 150 – 183 GHz channels (such as GMI) compared to sensors with mostly *h*-polarised channels (such as SSMIS).

For implementation in RTTOV-SCATT v13, a default polarisation ratio of 1.4 is applied to all ice species at all channels. If required, users can adjust this by species, but not yet by frequency (see the user guide). The polarised scattering applies only to conical sounders (e.g. AMSR2, GMI, SSMIS) and not yet to cross-track sounders (e.g. MHS). This is because the variation of the polarisation ratio as a function of incidence angle is not currently observable (there is no cross-track sounder with a high-frequency dual-polarisation channel) so it will be the subject of future simulation-based studies.

For more complete details of the polarisation upgrade to RTTOV-SCATT, see Barlakas *et al*. (2020)

3.11.4 Hydrometeor optical properties (hydrotables)

The optical property generation has been thoroughly revised for v13 including:

- New options for particle size distributions, such as a flexible modified gamma, McFarquhar and Heymsfield (1997) and Heymsfield *et al.* (2013)

- Inclusion of the ARTS optical property database (Eriksson, 2018) with a broader range of frozen particle shapes including hail and aggregates, and broader frequency range compared to the existing Liu (2008) database.
- A revised and more accurate integration over particle size
- Liquid water permittivity calculations use the Rosenkranz (2015) parametrisation, chosen by model to observation closure studies described in Lonitz and Geer (2018). Further details are also given in section 3.3 above.

The hydrotable generation package for RTTOV-SCATT at v13 is fully documented by Geer *et al.* (2020). Some of the new features have been used in the revised microphysical configuration described in the next section.

3.11.5 New default microphysical configuration

The microphysical configuration used to generate the default hydrometeor optical property lookup tables has changed at v13. The configuration was last updated by optimising the fits between SSMIS observations and simulated brightness temperatures using IFS model fields (Geer and Baordo, 2014). The configuration has been updated again at v13 for these reasons:

- To make use of frozen particle shapes from the new ARTS optical property database (Eriksson *et al*., 2018) which offers potentially more realistic aggregate and hail particle types, and provides optical properties up to 886 GHz, which will enable support of ICI when it launches in 2023.
- Again largely in support of ICI, to replace the Mie sphere assumption for cloud ice particles by a more realistic 3D shape, and also to make use of an alternative particle size distribution (in order to be less affected by the probe-shattering effect that gave excessive small particles in earlier PSDs).
- To add an additional hydrometeor category for ‘graupel’, intended to represent frozen precipitation in deep convection, keeping the ‘snow’ hydrometeor to represent large-scale (stratiform) snow particles.
- To adjust the tuning to take into account the effects of the source terms bugfix, the change in cloud fraction, and the new treatment of polarised ice scattering (all described above).
- Where possible, to make use of other new features of the optical property generation such as the improved integration over particle sizes.

An initial configuration was found by a multi-dimensional parameter search documented in Geer (2020), again based on optimising a cost function of the fit between SSMIS observations and simulations from the IFS. This initial configuration was used to find the optimal treatment of polarised scattering by Barlakas *et al.* (2020) and was also used as the baseline configuration for testing the bugfix to the downward source terms and the revision

to the minimum effective cloud fraction (described earlier). These three updates made significant changes to the simulated brightness temperatures. Hence the cost function was further optimised to give the final configuration in Table 3.11.2. This final configuration is also intended to be used in the IFS assimilation system from cycle 38r1.

This complex optimisation process is necessary because it is difficult or impossible to rely on physical first principles or field measurements to globally specify the microphysical parameters of cloud and precipitation. Choices that have been optimised in the context of one model configuration may have to be revised as the surrounding model is improved (perhaps removing a competing bias) or if additional sources of data become available (for example the availability of ICI data may lead to further revisions). In any case, many users of RTTOV-SCATT will make further adjustments to the microphysical configuration to suit the characteristics of their own forecast model.

Hydrometeor type	Pre-v13 configuration	Initial v13 configuration	Final v13 configuration
Rain	Mie sphere Marshall-Palmer PSD	Mie sphere Marshall-Palmer PSD	Mie sphere Marshall-Palmer PSD
Snow	Liu (2008) sector snowflake Field et al. (2007) tropical PSD	ARTS sector snowflake Field et al. (2007) tropical PSD	ARTS large plate aggregate Field et al. (2007) tropical PSD
Graupel	N/A	Liu (2008) 3-bullet Field et al. (2007) tropical PSD	ARTS column Field et al. (2007) tropical PSD
Cloud water	Mie sphere Gamma PSD	Mie sphere Gamma PSD	Mie sphere Gamma PSD
Cloud ice	Mie Sphere Gamma PSD	ARTS large column aggregate Heymsfield et al. (2013) stratiform PSD	ARTS large column aggregate Gamma PSD with generalised modified gamma parameters mu = 0, lambda = $1e^4$, gamma = 1 and N0 free.

Table 3.11.2: Configurations of microphysical assumptions used in hydrometeor optical property tables for RTTOV-SCATT.

Further details of the microphysical optimisation and its effects on the simulated brightness temperatures are given in Geer (2020).

3.12 RTTOV-SCATT new active sensor capability

From Version 13, the RTTOV-SCATT software supports the simulation of cloud and precipitation radar reflectivity profiles for several microwave active sensors. This includes the simulation of attenuated and non-attenuated reflectivity profiles on the model vertical grid for the Dual frequency Precipitation Radar (DPR) onboard the Global Precipitation Measurement Core Observatory (GPM-Core) and for the Cloudsat Precipitation Radar (CPR) on board the Cloudsat satellite.

As for passive microwave observation RTTOV-SCATT simulations, two coefficient files need to be specified. The clear sky coefficient file contributes to the computation of the attenuation effects by gases. The hydrotable includes the backscatter coefficients for each category of hydrometeor which are used for the radar reflectivity computation. The same options of radiative properties as for passive instruments are available for the computation of radar reflectivities.

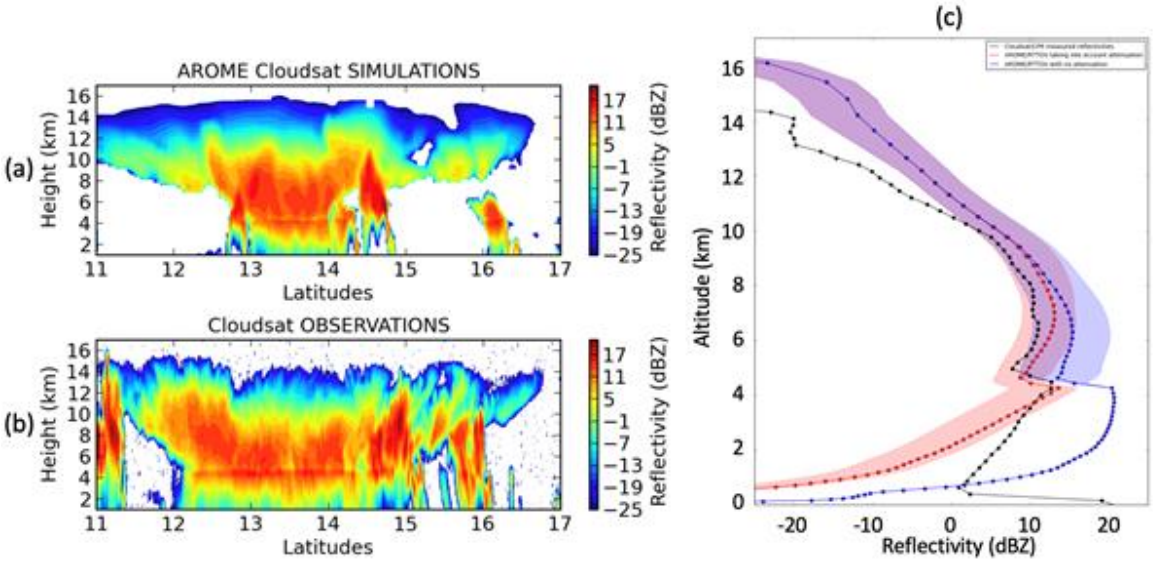

Figure 3.12.1: Example of cross-section of reflectivity profiles (a) simulated with RTTOV-SCATT from an AROME 3h forecast (Faure et al., 2020), (b) observed by Cloudsat on August 3rd, 2017 in the Caribbean's at 18h UTC. (c) One profile of the cross-section at 13.5° of latitude as observed in black and simulated without attenuation in blue, and with attenuation in red. The shaded areas correspond to the spread of several simulations with different particle shapes from the Liu tables as available in RTTOV-SCATT from the hydrotable generation.

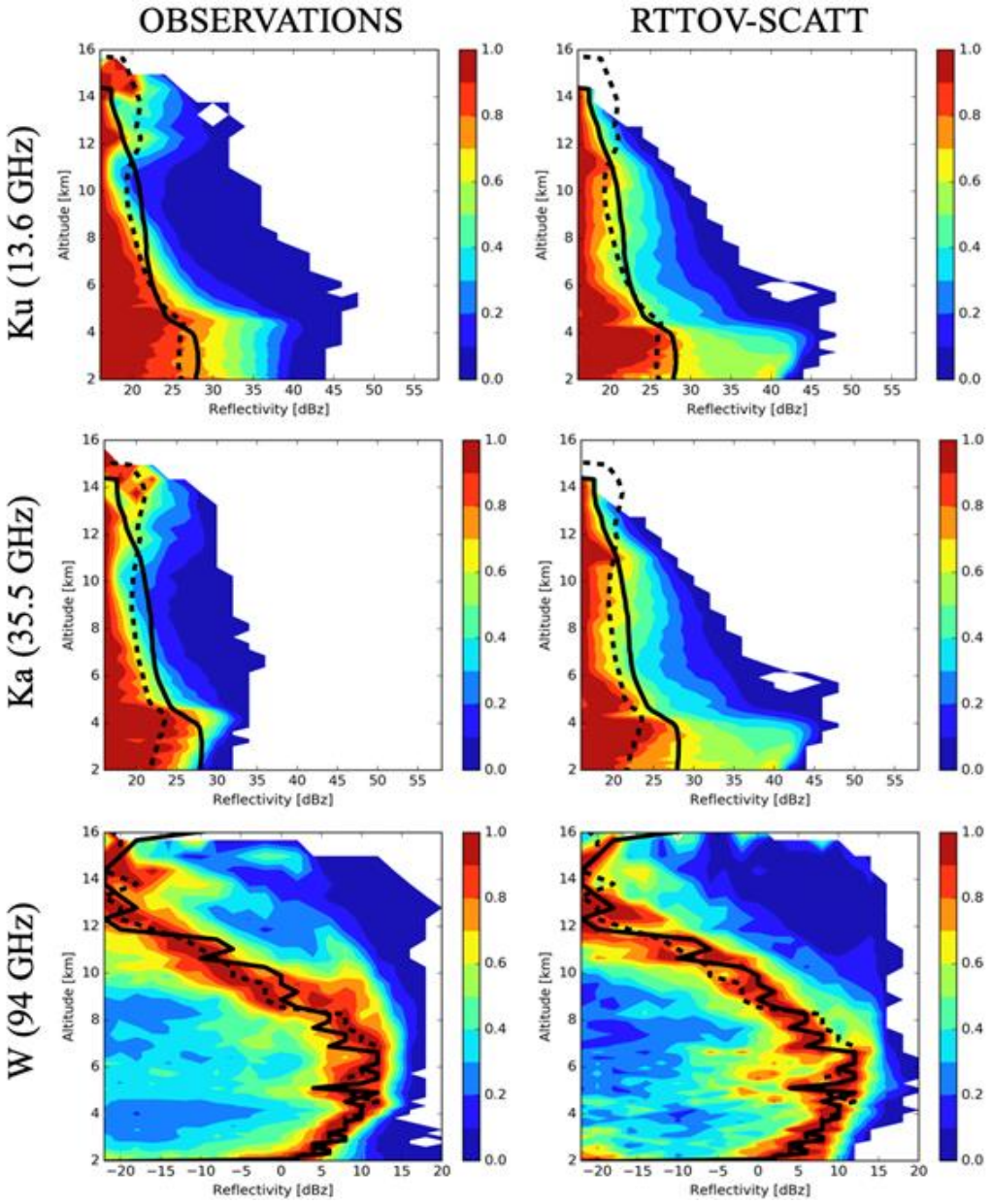

Figure 3.12.2: Normalized histograms of observed (left column), simulated (right column) attenuated reflectivities. The normalization is performed for each elevation separately by the maximum of occurrence at each elevation. The comparison covers a one-month period in August 2017 over the Antilles AROME domain. Simulations with attenuation are performed considering the IconCloudIce as particle shape for the single scattering properties for snowfall for the 3 frequencies: Ku-13 GHz (first row), Ku-35 GHz (second row) and W-94 GHz (third row). Black solid lines on histograms represent the simulations mean for Ku and Ka band and the simulations mode for the W band. The same information is shown for observations with dotted lines (Duruisseau et al., 2018).

Figure 3.12.1 shows an example of reflectivity profiles simulations at 94 GHz for the CPR instrument; it illustrates that for a certain range of altitudes between 3 km and 10 km of altitudes the model forecast and the observations agree with each other. The simulator has been further validated against observations from both the DPR and the CPR instruments. A statistical comparison between observations and RTTOV-SCATT simulations is shown on Figure 3.12.2.

3.13 PC-RTTOV updates

The only change to the PC-RTTOV implementation outlined in Matricardi (2010) and the updates in R11REP2013 and R12REP2017 is the inclusion of all trace gas (except SO_2) and aerosol simulation capabilities using the OPAC aerosol optical properties over land and water in the available options.

3.14 HT-FRTC updates

RTTOV v12 saw the incorporation of a version of HT-FRTC into RTTOV. Like PC-RTTOV, the HT-FRTC is a Principal Component radiative transfer code, but there are some differences in the implementation. HT-FRTC only performs monochromatic (typically about 300) radiative transfer calculations per profile at selected frequencies, which are found during the code training phase by k-means clustering of the radiances across all frequencies. The Principal Components are also derived during the training phase as well as regression coefficients which allow the prediction of the Principal Component Scores from the centroid radiances for every independent profile. The Principal Components themselves are sensor independent, which means no extra training is required to include additional sensors.

The implementation uses two types of coefficient files: One static file which contains all the properties required for the monochromatic calculations at the centroids as well as the sensor independent regression parameters for the prediction of the Principal Component Scores. And one file per sensor with the version of the Principal Components that is appropriate for that sensor and can be used to calculate channel radiances. In addition the netCDF versions of these coefficient files there is now also an ASCII version which negates the requirement for a netCDF library.

For HT-FRTC in RTTOV v13 a new parametrization of the gaseous absorption at the centroid frequencies has been developed. While the previous versions in RTTOV v12 were based on look-up tables, the new parametrization uses low order (up to quadratic) fits in temperature to the mass absorption at each centroid and for each of 100 pressure levels for each variable/mixed gas. The mass absorption is then interpolated onto user levels. The (self and foreign) water vapour continua are treated separately. The basis for the new coefficients was LBLRTM12.8.

As in the previous version, grey clouds and simple clouds are supported. There are some additions and changes to the treatment of surfaces by HT-FRTC in RTTOV v13. In addition to SSEM the IREMIS sea surface emissivity model is now supported. The major change is to define surface properties like emissivity and specularity now at the centroids rather than channels. The reason for this is that HT-FRTC is a PC model and does therefore not provide emissivity Jacobians at all the channels. The emissivity Jacobians at the centroids does however provide sufficient information for surface emissivity retrievals. To be consistent, for HT-FRTC, the emissivity atlases provide emissivities at centroids.

A number of improvements have been implemented in HT-FRTC in RTTOV v13 which aim to make the code more efficient. The fact that not all variable gases contribute at all monochromatic centroid frequencies or contribute to all sensor channel radiances has been exploited by adding arrays to the coefficient files which contain the relevant information. As a result some optical depths and Jacobian calculations at the centroids as well as some Jacobian calculations at certain sensor channels are now skipped.

3.15 Additional changes to RTTOV inputs, outputs and internal calculations

Some additional changes have been made within RTTOV which have a small impact on RTTOV radiances. These have been implemented to keep RTTOV up to date with new science and to eliminate minor historical inconsistencies in the code. They are described here.

Changes to values of physical constants

The values for several physical constants used in RTTOV have been updated with the latest values from NIST (Tiesinga *et al*, 2019). The impact of this change is extremely small (below 1mK). It is possible to compile RTTOV v13 with the v12 values of the constants by supplying a macro at compile time. Note that the updated values used for these constants are now considered “exact” according to NIST and as such they should not change in the future.

Changes to RTTOV options (new options/changes to default behaviour)

The 2m temperature has long been a mandatory input to RTTOV and is used in the calculation of the Planck radiance in the near-surface layer. However, it was not previously used in the calculation of the optical depth predictors for the layer containing the surface, even though the 2m water vapour is used if the *use_q2m* option is set to true. RTTOV v13 addresses this minor inconsistency by using the 2m temperature in the optical depth regression predictor calculations by default, but this can be disabled (to replicate the RTTOV v12 behaviour) by setting the new *use_t2m_opdep* option to false. The impact on direct model radiances is up to order 0.01K. Note also that this generates an additional sensitivity

to the 2m temperature in the Jacobian model based on its influence over the near surface atmospheric optical depth.

Two aspects of the direct model calculations were identified as causing small discontinuities in the direct model which caused problems for some users. Mitigations for these have been put on switches in the options structure:

In earlier versions of RTTOV, the surface elevation was associated with the nearest level above (or equal) to the surface pressure. This impacts the calculations of the geometry of the radiation path and could lead to discontinuities with respect to the 2m pressure as the surface pressure passes through a pressure level. By default, RTTOV v13 instead associates the elevation with the 2m pressure which addresses this problem. The impact on forward model radiances is up to order 1mK. An experiment at the Met Office indicated this has neutral impact in NWP data assimilation. The prior behaviour can be selected by setting the *fix_hgpl* option to false. This switch is deprecated and may be removed in a future release leaving only the new behaviour.

In earlier versions of RTTOV, the integration of the radiative transfer equation included a check for small layer delta-transmittance in the near-surface partial layer (i.e. the difference in the level-to-space transmittances for the level above the surface and the surface itself). If this delta-transmittance was below a threshold, the contribution of Planck emission from the near-surface partial layer was omitted. This check leads to discontinuities in cases where small changes in the input variables lead to the delta-transmittance crossing this threshold. RTTOV v13 excludes this check and always includes the contribution from the near-surface layer, which mitigates the direct model discontinuities with small impact (up to order 0.01K) on radiances. Experiments at ECMWF and the Met Office indicate this has neutral impact in NWP data assimilation. The prior behaviour can be selected by setting the *dtau_test* option to true. This switch is deprecated and may be removed in a future release leaving only the new behaviour.

Some RTTOV options have new default values representing the recommended settings:

- *opts%rt_all%addrefrac* – enables atmospheric refraction in the local radiation path geometry calculations, true by default.
- *opts%rt_mw%clw_scheme* – selects the MW cloud liquid water absorption parameterisation, the default is 2. Rosenkranz (2015) (see section 3.3.1).
- *opts%rt_ir%solar_sea_brdf_model* – selects the ocean BRDF model, default is 2. Elfouhaily *et al* (1997) (see section 3.7).
- *opts%rt_ir%grid_box_avg_cloud* – if true, RTTOV expects grid box average cloud amounts as input for VIS/IR simulations. This is consistent with the cloud fields from many NWP models. If false, RTTOV expects the cloud concentration in the cloudy

fraction of the layer, which is obtained by dividing the grid box average cloud by the cloud fraction. The default is true.

- *opts%interpolation%reg_limit_extrap* – if true, this option uses the optical depth regression training profile limits to extrapolate the user input profiles at the top of the atmosphere if necessary. This is now the default and recommended option. If false it uses constant value extrapolation. Since the latter is unlikely to generate realistic profiles this option is deprecated and may be removed in a future release.

CMBR for MW simulations

RTTOV has for a long time included the contribution of the Cosmic Microwave Background Radiation (CMBR) to the top of atmosphere radiance in MW simulations. RTTOV also optionally outputs “secondary” radiance outputs comprising, for example, downwelling radiances at each level, and the at-surface reflected radiation. These secondary radiances are used, for example, for all-sky dynamic emissivity retrievals (e.g. Baordo and Geer, 2016). The CMBR calculation has historically been done as a separate radiance contribution to the top-of-atmosphere radiance, and as such it was not included in the secondary radiance outputs. RTTOV v13 now includes the CMBR contribution in the downwelling radiances so that it is included in all output radiances.

Polarisation for TROPICS

The TROPICS cubesat MW sensor has a novel (for RTTOV) polarisation whereby each channel is a particular (uneven) combination of H- and V-pol radiances. This necessitated creating a new category for sensor polarisation and for sensors in this new category the H-/V-pol ratio for each channel is now included in RTTOV v13-format optical depth coefficient files. For this reason the true TROPICS polarisation is only supported by v13 predictor optical depth coefficient files and is not supported by RTTOV v12 or with the older v7 predictor-based coefficient files.

Updates for VIS/IR scattering

Aerosol simulations using aerosol concentration units of kg/kg and ASCII aerosol optical property files give very slightly different results to RTTOV v12. The aerosol mass concentration is converted to a particle number density internally by RTTOV. The conversion factor stored in the files in v13 is the reciprocal of that in v12 to make them consistent with the corresponding values for certain cloud optical properties, and the limited precision (compared to the double precision used within RTTOV) in the ASCII coefficient files leads to differences which are negligible compared to other simulation errors: the radiances are identical up to at least 6 significant figures.

For direct model solar aerosol simulations, the output level-to-space transmittances for solar channels in the *tausun_levels** output arrays in the *rttov_transmission* structure now contain gas and aerosol transmittances (rather than gas-only) to make them consistent with the *tausun_total** arrays (the total atmospheric transmittance for solar channels) and the IR output transmittance arrays.

Cloud extinction transmittances (excluding gas absorption and disregarding cloud fraction) are now output in the *rttov_transmission* structure for VIS/IR cloudy simulations.

For VIS/IR cloud simulations using the cloud liquid water "Deff" optical properties, user input Deff (effective diameter) values used in the simulations are now clipped to the minimum/maximum values supported by the optical properties.

Updates for IR emissivity atlases

The CAMEL 2007 atlas is now interfaced with the new CAMEL standard deviations from climatology rather than the old UWIRemis standard deviation datasets. The UWIRemis and CAMEL 2007 IR emissivity atlases now optionally output the atlas PC eigenvalues and eigenvectors.

Other new inputs/outputs

The diffuse reflectances (used for downwelling/downward-scattered radiation) are output for all channels and may be user-specified for visible/near-IR channels separately from the BRDF.

The geometric heights corresponding to the input pressure levels computed internally by RTTOV as part of the local radiation path geometry calculations are now available as an output in the *rttov_radiance* structure.

4. Testing and Validation of RTTOV-13

4.1 Comparison of simulations between RTTOV v12 and RTTOV v13

The primary outputs from RTTOV are the top of atmosphere radiance for each channel and so this is the main parameter for which the RTTOV v13 simulations are checked and compared with the corresponding RTTOV v12 values. The reason for differences between RTTOV v12 and RTTOV v13 computed radiances are due to the changes listed in the previous section. Comparisons between RTTOV v12.3 and RTTOV v13.0 were made according to the parameters listed in Table 4.1 for calculations using the 83 diverse profile

set from the ECMWF model (Chevallier *et. al.* 2006). The mean differences were then plotted in the following figures.

For the Jacobians for each channel the mean averaged over the Jacobians computed from the 83 diverse profiles are plotted here for both RTTOV v12 and v13 for temperature and water vapour.

Parameters	**RTTOV v12.3**	**RTTOV v13.0**
Number of layers for optical depth calculation	54 (0.005-1050hPa) except for IASI: 101 (0.005-1100hPa)	54 (0.005-1050hPa) except for IASI: 101 (0.005-1100hPa)
Input Profile set	83 Profiles on 101L	83 Profiles on 101L
Visible & Infrared Simulations		
Spectroscopic data	LBLRTMv12.2/ AER 3.2, MTCKD2.5.2	LBLRTMv12.8/ AER 3.6, MTCKD3.2
Surface emissivity	0.98	0.98
Optical depth predictors	Version 7 ABI IR-only O_3 only Version 9 ABI VIS, IR O_3+CO_2 Version 9 IASI 7 gases	Version 7 ABI IR-only O_3 only Version 9 ABI VIS, IR O_3+CO_2 Version 9 IASI 7 gases Version 13 AHI IR-only O_3-only Version 13 AHI VIS, IR O_3+CO_2 Version 13 IASI 7 gases
Microwave Simulations		
Spectroscopic data	Liebe 89 update/Tretyakov 05	Liebe 89 update/Tretyakov 05
Surface emissivity	0.6	0.6
Optical depth predictors	Version 7	Version 7 / Version 13

Table 4.1 The parameters assumed for the RTTOV v12 and RTTOV v13 comparisons

The comparisons shown here were for a visible and infrared radiometer, GOES-16 ABI, a hyperspectral sounder, MetOp IASI, and a microwave radiometer ATMS. These instruments cover the full spectral domain supported by RTTOV and the various spectral resolutions of

the channels. They are also important instruments used in the NWP data assimilation systems and so documenting the differences between the different versions of RTTOV is necessary. For all the RTTOV v12 and RTTOV v13 difference plots shown below the mean bias (AVG), the standard deviation of the difference (STD) and the maximum difference (MAX) are plotted for the 83 diverse profiles.

4.1.1 GOES ABI Comparisons

The GOES ABI has a range of visible and infrared channels which have spectral response functions that cover many absorption lines and should be representative of the many imagers on geostationary and polar orbiting satellites. Figure 4.1.1 shows the differences between the RTTOV v12 and RTTOV v13 computed brightness temperatures the latter using the new v13 predictors and updated spectroscopy. The mean biases are all less than 0.1 K except for channels 9+10 which are the lower peaking water vapour channels and just exceed 0.1 K which is due to the new spectroscopy used. The standard deviations are around 0.1K except for the window channels which are lower. The mean differences due to the change of predictors are all less than 0.1K in bias and standard deviation. Channels 7, 9 & 10 all have mean biases around 0.1K due to the change in spectroscopy. The ABI instrument noise is 0.1 K for the infrared channels. These differences should be similar for other imagers and sounders (e.g. HIRS, SEVIRI).

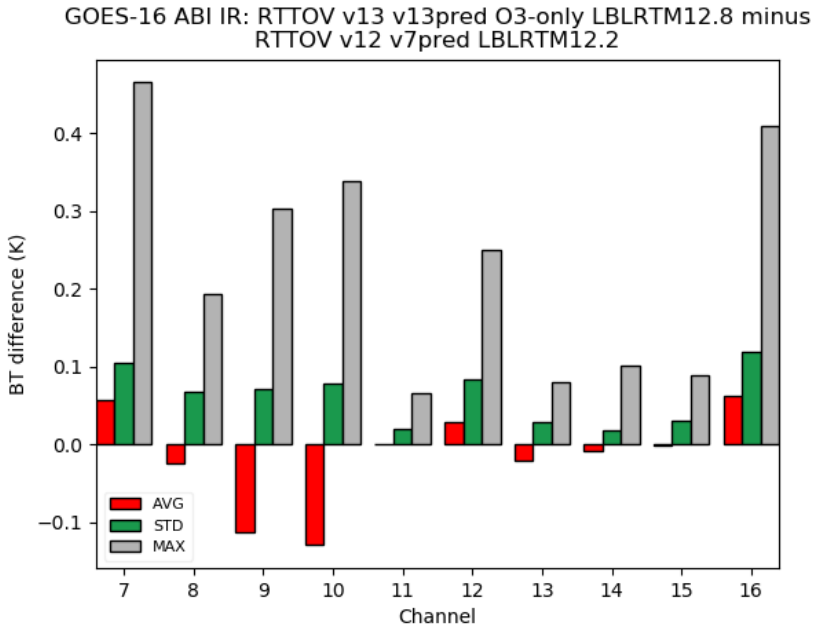

Figure 4.1.1 Brightness Temperature differences for ABI infrared channels between RTTOV v12 and RTTOV v13 with new predictors and spectroscopy computed for the 83 diverse profile dataset.

For the visible and near infrared channels of ABI (channels 1-6) a comparison of the reflectances computed for both the new spectroscopy and the new predictors is shown in Figure 4.1.2. For channel 6 at 2.26 microns the differences are dominated by the change in the water vapour continuum in this region from MTCKD 2.5.2 (RTTOV v12) to MTCKD 3.2 (RTTOV v13) (see Figure 3.1.2) which gives a mean bias of -0.004 in reflectance. For channel 4 at 1.38 microns the larger differences are from the new v13 predictors. Overall with the exception of channel 6 the differences are all below 0.001 in reflectance.

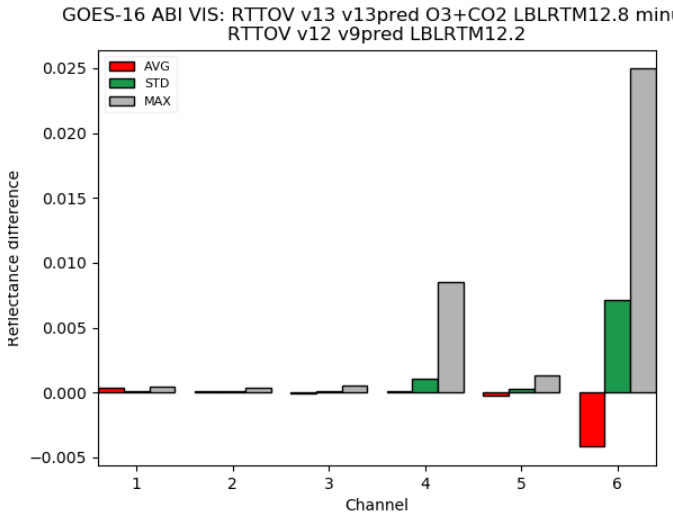

Figure 4.1.2. Reflectance differences for ABI visible/near infrared channels between RTTOV v12 and RTTOV v13 for new predictors and spectroscopy computed for the 83 diverse profile dataset.

For the temperature and water vapour Jacobians for the infrared channels any differences are dominated by the change in spectroscopy. Figure 4.1.3 shows the Jacobians for temperature and water vapour for all the infrared channels and the only channel with a significant difference for both the temperature and water vapour Jacobians is channel 7 (3.9 microns wavelength).

The temperature and water vapour Jacobians for the ABI visible and near infrared channels are plotted in Figure 4.1.4. Channel 4 (1.38 microns) has significant differences due to the change from v9 to v13 predictors. In contrast the large differences seen for channel 6 (2.26 microns) in both Jacobians is due to the different spectroscopy assumed in LBLRTM12.2 and LBLRTM12.8 described in section 3.1.

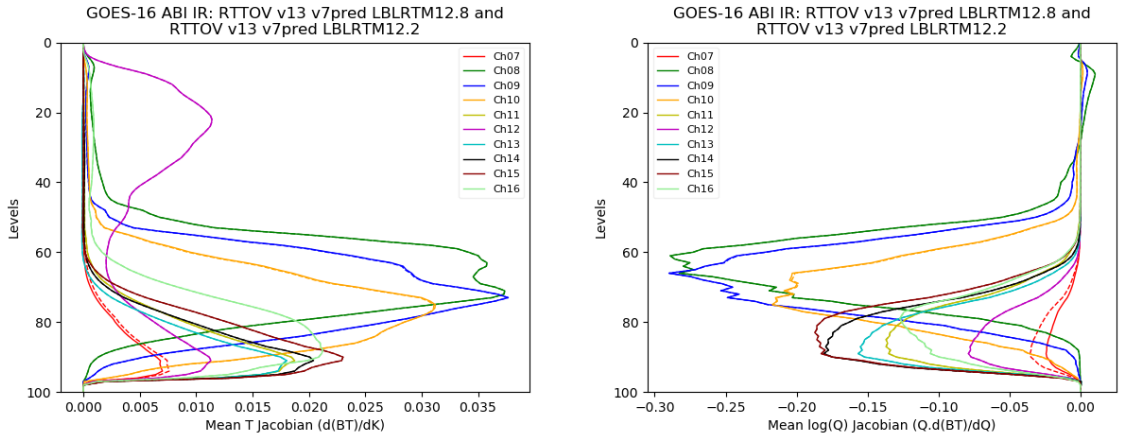

Figure 4.1.3 Temperature (left panel) and water vapour (right panel) Jacobians for the ABI infrared channels for LBLRTM12.8 (solid line) and LBLRTM12.2 (dashed line) with v7 predictors.

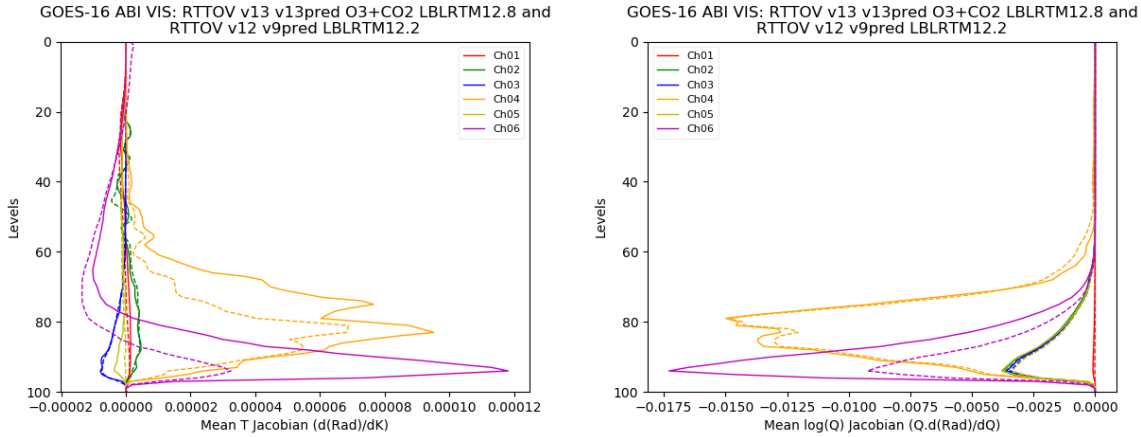

Figure 4.1.4 Temperature (left panel) and water vapour (right panel) Jacobians for the ABI visible/near infrared channels for RTTOV v13 with LBLRTM12.8/V13 predictors (solid line) and RTTOV v12 with LBLRTM12.2/v9 predictors (dashed line).

4.1.2 MetOp IASI differences

The hyperspectral sounder IASI covers a wide range of the infrared spectrum with no gaps so is a good test of the simulations in the infrared. Figure 4.1.5 shows the differences between v12 and v13 with the impact of both the updated spectroscopy and new predictors included where SO_2 is taken as a fixed gas. Some discussion of the performance where SO_2 is included as a variable gas is given in section 3.2.3. The updated spectroscopy in LBLRTM12.8 dominates the differences with biases up to -0.8 K in the mid infrared band (1250-2200 cm^{-1}) although much less in the rest of the infrared. The impact of the new v13 predictors is small across the spectrum (<0.1 K) with the only exception being the band at

2100 cm^{-1} where differences up to 0.2 K are seen. Beyond 2300 cm^{-1} there is a consistent small negative bias (-0.1 K) introduced by errors in LBLRTM12.8 (see section 3.1). The maximum differences are much higher than the means at the shorter wavelengths peaking at around 2 K in bands at 2500 cm^{-1} and close to 1 K in a few other parts of the spectrum in the mid-infrared (1750-2250 cm^{-1}). To put this in context the instrument noise for IASI is around 0.25 K below 2300 cm^{-1} and then increases to above 1K at shorter wavelengths.

For the IASI Jacobians a selection of 6 channels were selected to represent different regions of the infrared spectrum covered by IASI. Figure 4.1.6 shows the temperature and water vapour Jacobians for the selected channels for the old and newer spectroscopy in LBLRTM and for RTTOV v13 using the new predictors. The differences between the temperature Jacobians are due to both the new predictors and the updated spectroscopy in equal measure. For the water vapour Jacobians the differences are mainly due to the new spectroscopy affecting the two shorter wavelength channels at low levels.

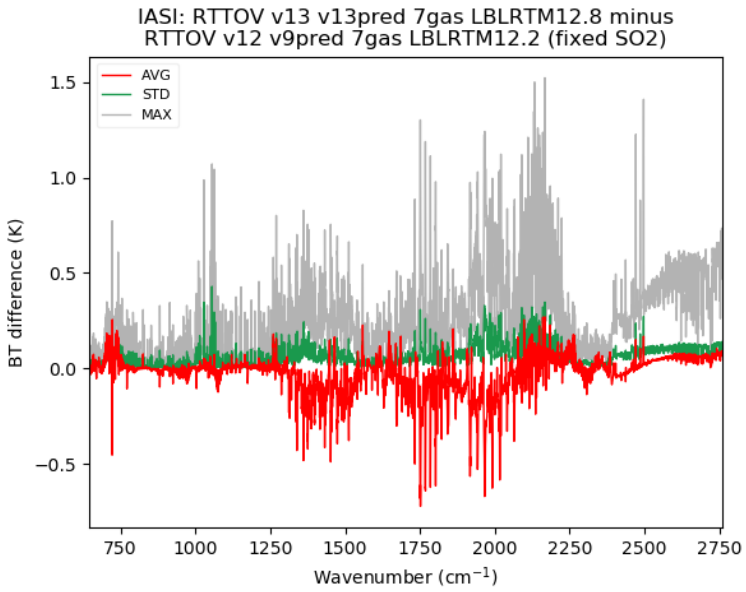

Figure 4.1.5 Brightness Temperature differences for IASI channels between RTTOV v12 and RTTOV v13 for new predictors and spectroscopy computed for the 83 diverse profile dataset for fixed SO_2.

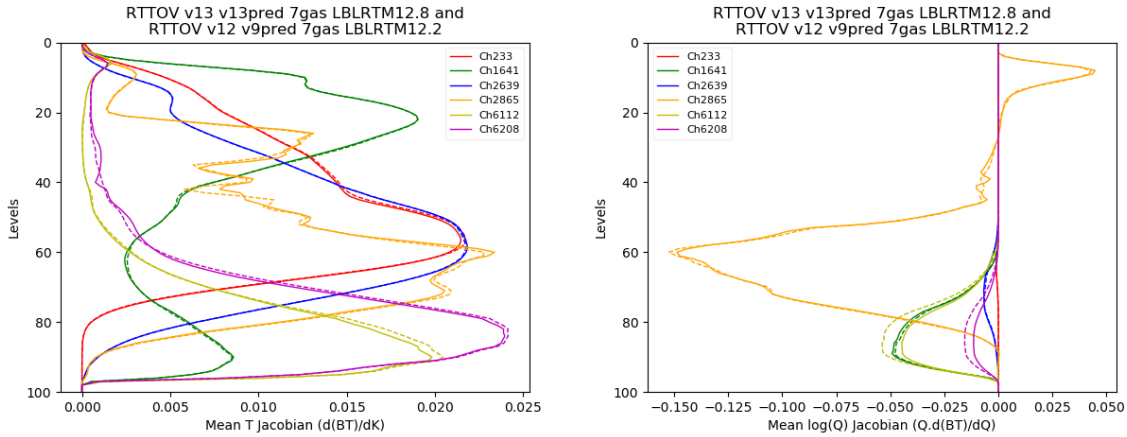

Figure 4.1.6 Temperature (left panel) and water vapour (right panel) Jacobians for a selection of infrared channels for RTTOV v13 with LBLRTM12.8/v13 predictors (solid line) and RTTOV v12 with LBLRTM12.2/v9 predictors (dashed line).

4.1.3 Suomi-NPP ATMS Comparisons

For the microwave sensors ATMS was used to show the differences between RTTOV v12 and RTTOV v13 as it spans all the frequencies used in operational systems. Figure 4.1.7 summarises the results for all the ATMS channels. There are no spectroscopic differences in AMSUTRAN between RTTOV v12 and RTTOV v13 and this plot also uses the same v7 predictors and hence the same coefficient file. The cause of the small differences (means <0.005 K) is that there are different default options recommended for RTTOV-13 as documented in section 3.15. The impact of using the new v13 predictors for microwave sounders is documented in Figure 3.2.1 in section 3.2. Mean biases are less than 0.01 K but for some profiles maximum differences can be up to 0.7 K for the 183 GHz water vapour

channels. The instrument noise for ATMS channels are typically >0.6 K much larger than the fast model errors.

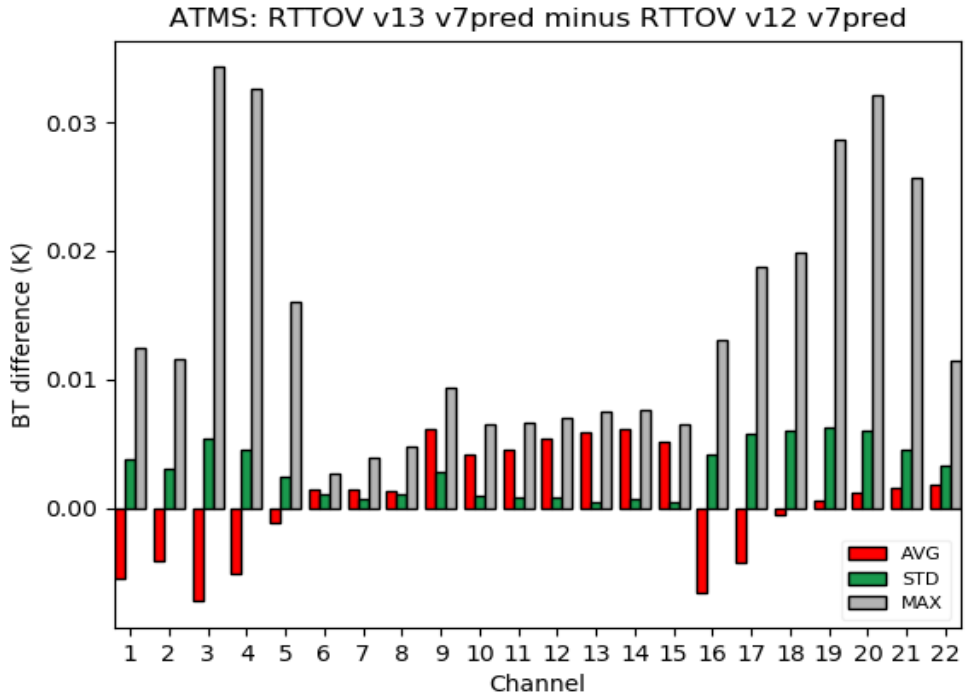

Figure 4.1.7 Comparison of simulated ATMS brightness temperatures computed with RTTOV v13 and v12 using the same coefficient file but with the new default values for v13.

Figure 4.1.8 shows plots of the ATMS temperature and water vapour Jacobians for the default options for RTTOV-v12 and RTTOV v13 and the differences are so small it is not possible to see them except for channel 16 (89.5 GHz) which is a window channel with some sensitivity to water vapour. Comparisons between v7 and v13 predictors also show very small differences in the ATMS Jacobians (see sect 3.2). Similar results are seen for the AMSU-A/MHS and MWTS/MWHS sounders and conical scanning microwave imagers.

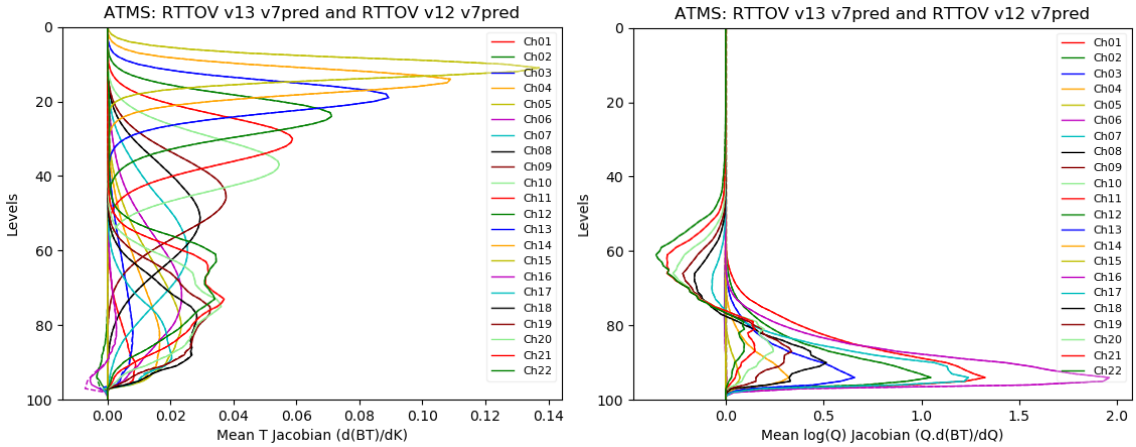

Figure 4.1.8. Temperature (left panel) and water vapour (right panel) jacobians for the ATMS channels for RTTOV v13 (solid line) and RTTOV v12 (dashed line) for the default options. Note that nearly all dashed lines are indistinguishable from solid lines.

4.2 Comparisons with observations

In the following a comparison of RTTOV v12.3 and RTTOV v13 simulated radiances with coincident observations from a variety of sensors is made using the ECMWF IFS model fields.

Monitoring experiments (i.e., monitor a change in first-guess (FG) departure without generating a new analysis and forecast) were conducted with ECMWF's 4D-Var assimilation system from 1st December to 31st December 2019 with RTTOV v12.3 (control) and with RTTOV v13 (experiment) and the corresponding observation minus FG statistics were collected for several different instruments. All experiments are based on cycle 47R1 of the ECMWF operational system and use the same parent experiment but, have been run at the lower spatial model resolution of T_{CO} 399 (approximately 25 km), with 137 levels in the vertical.

FG-departure plots for ATMS, geostationary radiances and IASI are shown in figures 4.2.1 – 4.2.3 with RTTOV v12.3 and RTTOV v13.0, respectively. In RTTOV v13, the RTTOV-SCATT science updates and new scattering properties are taken explicitly into account, but with the same ECMWF operational infrared and microwave coefficient files. The mean and standard deviation statistics of FG-departures before bias correction show generally small differences between the runs with either version of RTTOV. As an example, for ATMS channel 8 the standard deviation of differences between RTTOV v13 and RTTOV v12.3 can reach up to 0.001K and RTTOV v13 produce brightness temperature that are up to 0.01K colder. These differences are very similar for geostationary and hyperspectral infrared radiances.

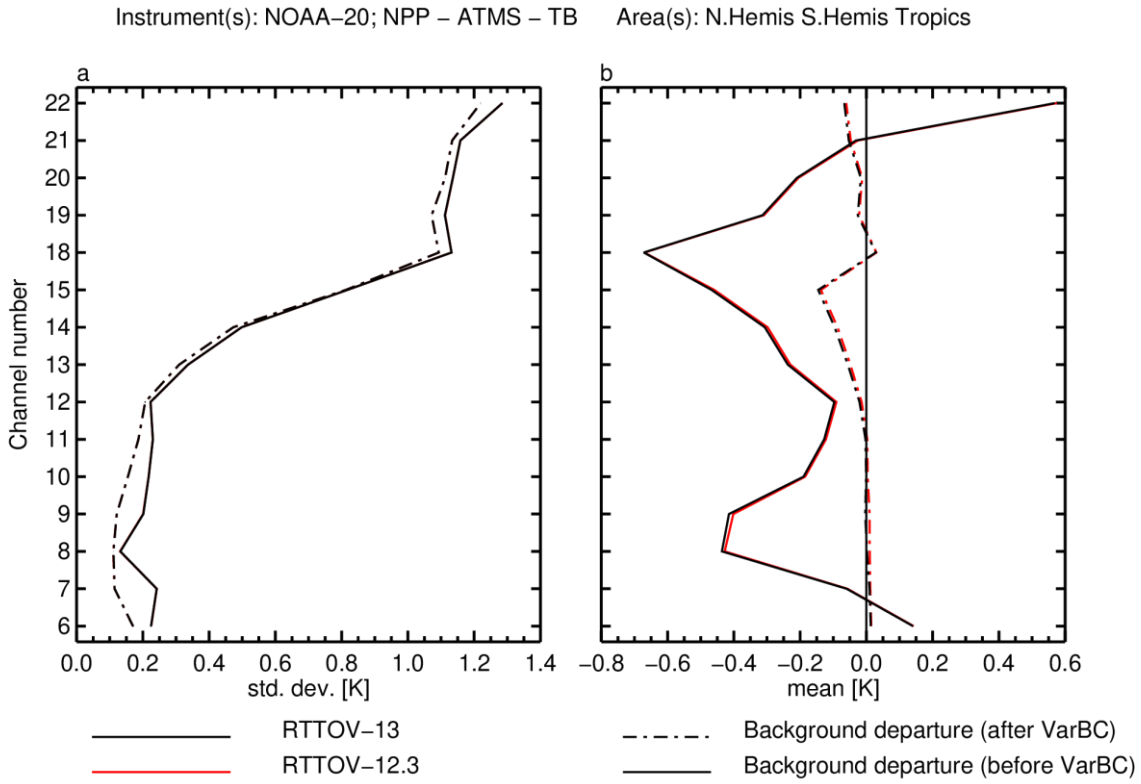

Figure 4.2.1 First guess departure statistics for ATMS (on S-NPP and NOAA-20) for December 2019 in the ECMWF system. Global statistics (bias and standard deviation) for RTTOV v13 experiment are shown in black, whereas statistics for the RTTOV v12.3 experiment are shown in red, with solid (dotted) lines showing FG-departure statistics before (after) bias correction.

The impact of using RTTOV v13 with the new v13 predictors for microwave sounders was studied and comparisons against v7 predictors performed. Figure 4.2.4 shows FG-departures comparisons between v7 and v13 predictors for ATMS. As expected, using the v13 predictors has a rather small impact on the ATMS brightness temperatures simulated by RTTOV v13. Mean biases are less than 0.01K for most of the channels and the largest effect can be seen for the 183 GHz ATMS water vapour channels where the standard deviation of differences between v13 and v7 predictors can reach up to 0.02K (i.e., in channel 22).

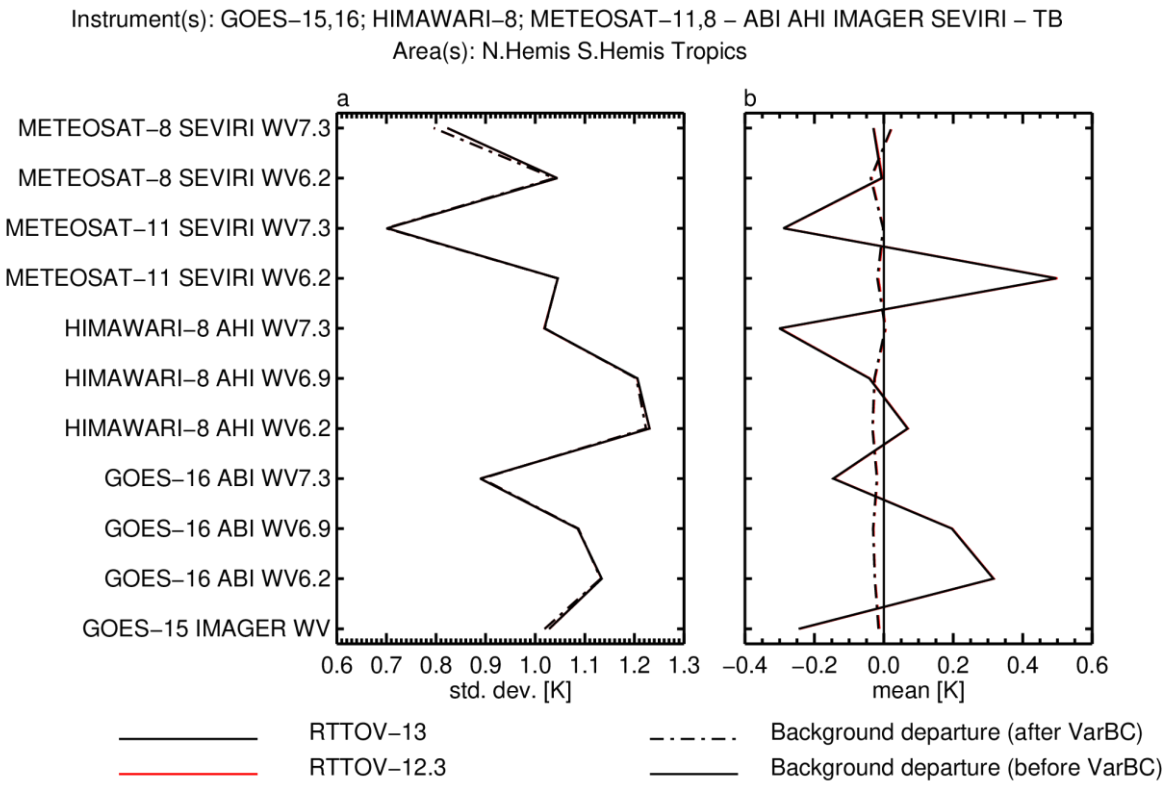

Figure 4.2.2 As Fig. 4.2.1, but for geostationary radiances around the globe.

New coefficient files based on LBLRTM 12.8 calculations have also become available for infrared sensors. Figure 4.2.5 shows the comparisons between the RTTOV v13 computed brightness temperatures for geostationary radiances using the updated spectroscopy based on LBLRTM 12.8 and with O_3 only, v7 and v13 predictors, respectively. The mean differences due to the change of predictors are all less than 0.1K in bias and the standard deviation of differences between v13 and v7, O_3 only predictors is less than 0.01K. The impact of the new v13 predictors is comparable with v7 predictors across the IASI spectrum (Figure 4.2.6) with the only exception being the ozone band at 1050 cm^{-1} where some large differences were seen, in particular using v9 predictors with the new LBLRTM 12.8 spectroscopy.

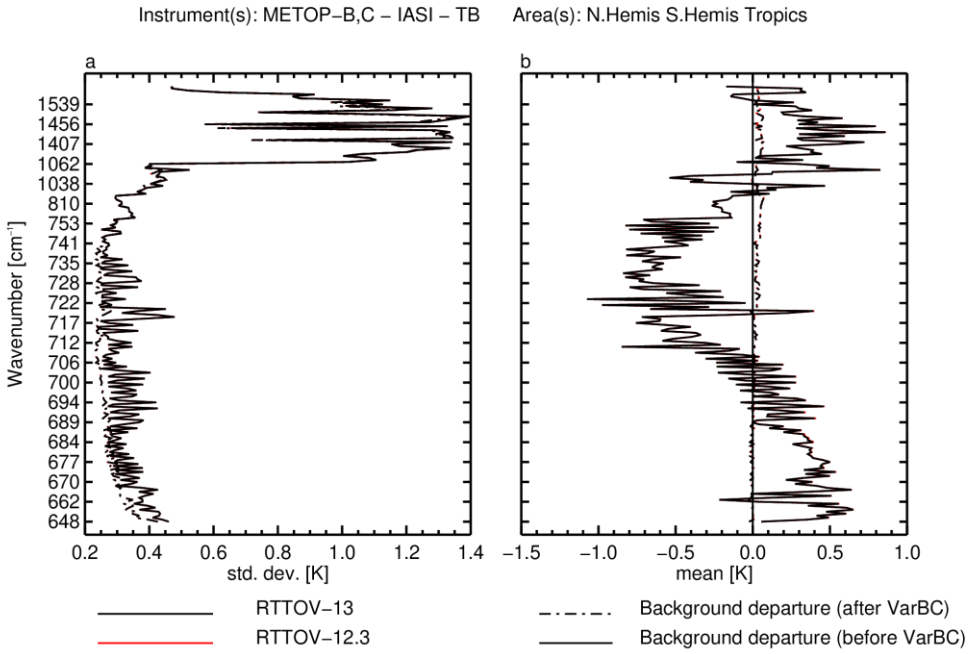

Figure 4.2.3 As Fig. 4.2.1, but for IASI on MetOp-A/B/C over the globe.

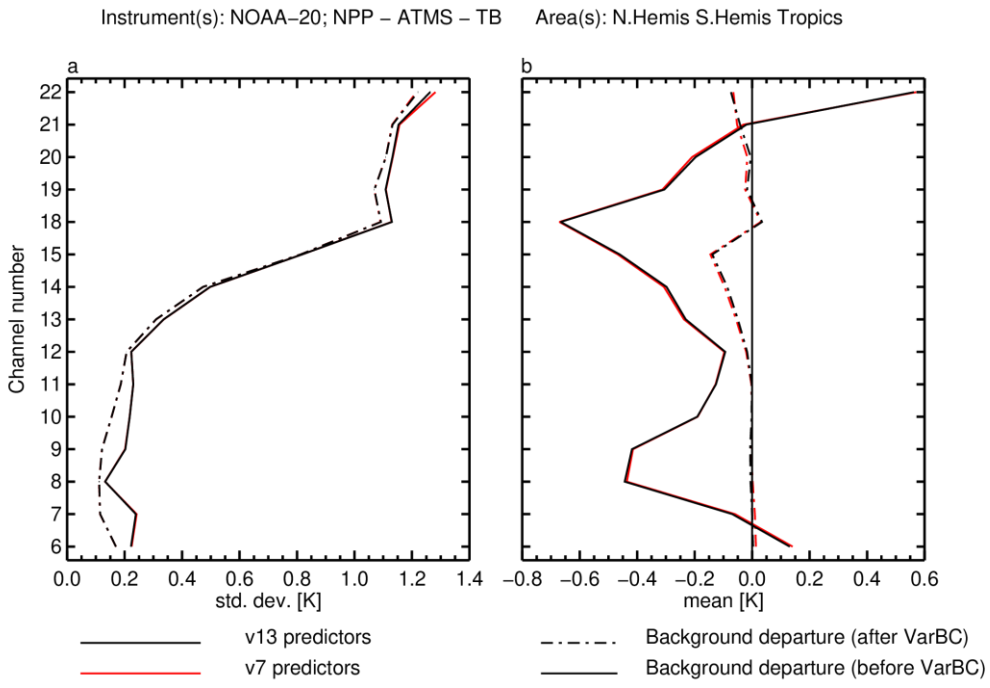

Figure 4.2.4 Comparison of ATMS - observed minus simulated brightness temperatures computed with RTTOV-13 using v7 (red line) and v13 predictors (black line).

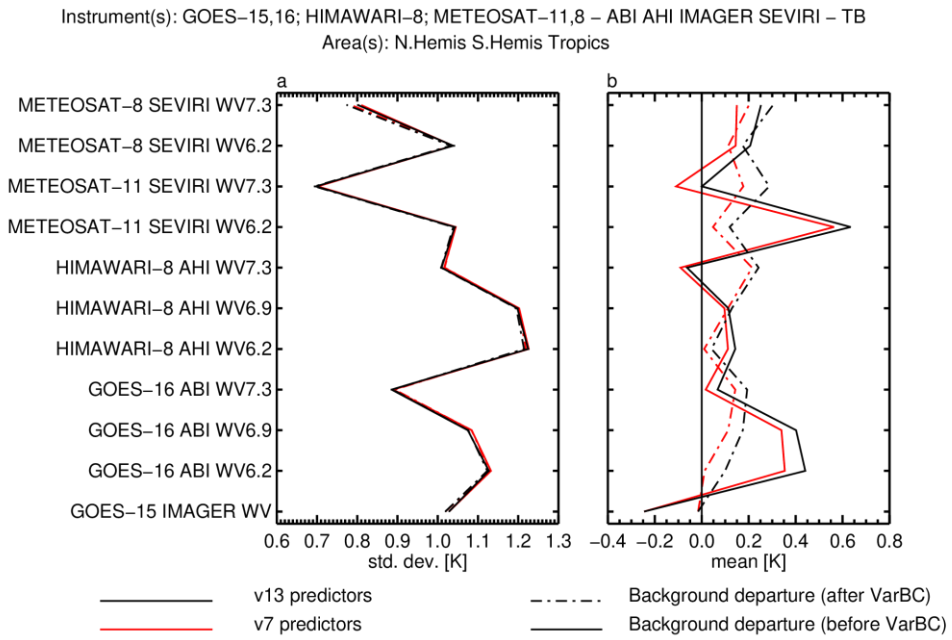

Figure 4.2.5 Comparison of geostationary radiances - observed minus simulated brightness temperatures computed with RTTOV v13 using mixed gases, water vapour and O_3 only coefficients, LBLRTM 12.8 v7 (red line) and LBLRTM 12.8 v13 predictors (black line).

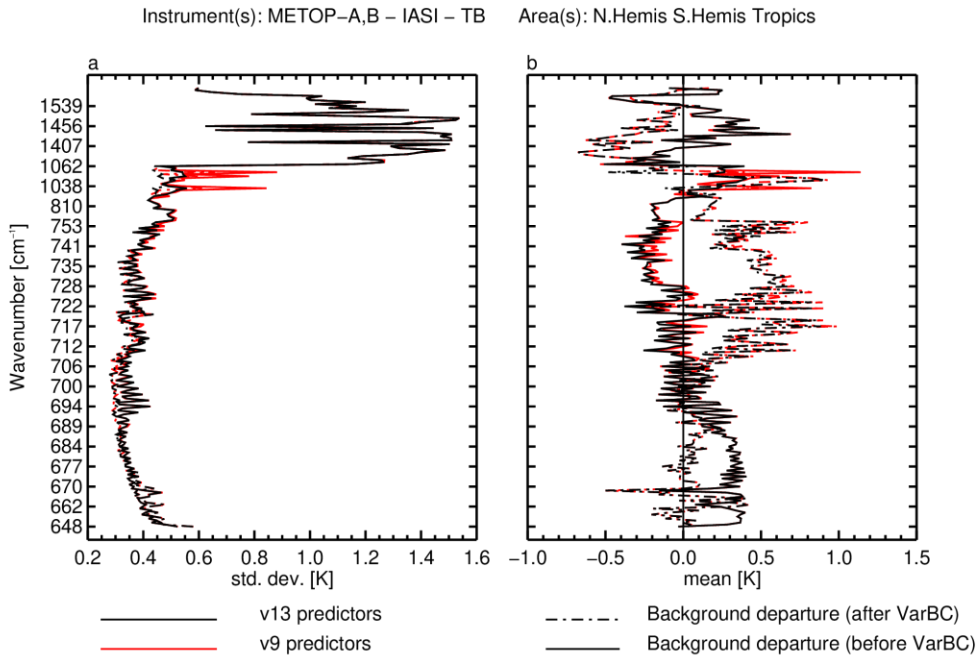

Figure 4.2.6 As Fig. 4.2.5, but for IASI on MetOp-A/B over the globe. Observed minus simulated brightness temperatures computed with RTTOV v13 using all gas coefficients, LBLRTM 12.8 v9 (red line) and LBLRTM 12.8 v13 predictors (black line).

5 Summary

The latest version of RTTOV, RTTOV v13 has been validated in several ways to show the same or improved performance for the prediction of satellite top of atmosphere radiances both for clear air, cloudy and aerosol profiles. It builds on previous versions of RTTOV. The changes have been validated as described in this document and further references to the new science implemented given. Referring to the list of changes made between RTTOV v12 and RTTOV v13 given in section 3 the following comments can be made:

- Improvements to infrared and microwave line-by-line models and associated spectroscopic datasets from which the RTTOV coefficients are computed

  The change from HITRAN2008 to HITRAN2012 has resulted in some significant differences due to changes in the water vapour lines and continuum in a few spectral regions.

- New predictors of layer optical depth allowing more accurate simulations and easier addition of new gases

  The new predictors of optical depth developed are more accurate and with similar computation speed as shown in the validation results presented here. It also makes adding new variable gases much easier.

- Extension of spectrum to cover far infrared and higher frequency microwave to support new instruments such as ICI and FORUM

  The spectral range has been extended to the far infrared ($100cm^{-1}$) and up to 800 GHz for the microwave to support future new instruments.

- Improved treatment of cloud absorption for microwave radiance simulations

  The cloud absorption option for microwave radiances is now computed on user defined levels not the fixed RTTOV coefficient levels which should be more accurate and updated options are available for the water permittivity parameterisation.

- Improved treatment of scattering from water, ice clouds and aerosols in visible and infrared radiances

  For the visible/infrared, updates to the cloud optical properties (refractive indices) have been adopted along with an option of using a parametrisation of cloud drop effective radius from the liquid water concentration. An updated version of the Baran ice scattering database has also been introduced which provides more consistent results across all wavelengths. Cloud transmittances are a new output from RTTOV.

A new set of aerosol optical properties based on the CAMS aerosol species has been introduced and a new tool is available to enable users to generate their own aerosol optical property files for use with RTTOV.

- New infrared surface emissivity atlas

  A new infrared surface emissivity atlas has been provided based on a much longer period and better treatment of snow surfaces. There is now an optional output of emissivity atlas PC scores and eigenvectors for the UWIRemis and CAMEL 2007 IR atlases.

- Treatment of scattering from surfaces

  The specular vs lambertian scattering from the surface has been modified to allow a mix of both types to be included in the calculation and it can now be specified per channel. The sunglint model has been updated to use a better wave spectrum parameterisation.

- Updates to MFASIS visible/near infrared scattering

  For the visible and near infrared the MFASIS model has been significantly improved in several aspects (e.g. separate treatment of Rayleigh scattering) and speeded up making it now feasible for data assimilation applications.

- Improved treatment of Rayleigh scattering

  Rayleigh scattering is now treated separately from the line-by-line calculation with a parameterised model in RTTOV which allows for a better treatment of multiple scattering with clouds and aerosols.

- Updates to simulations of principal components (HT-FRTC & PC-RTTOV)

  The HT-FRTC model has been updated to enable calculation of "simple cloudy" and overcast radiances, to have more flexibility in specifying surface emissivity, and be more efficient in compute resources. PC-RTTOV now has the option of using all trace gases and aerosols over land and sea.

- Updated version of RTTOV-SCATT

  A number of updates to RTTOV-SCATT which include the following:

  i. *Fixing a bug in the downward scattered radiation .*
  ii. *New interface allows for an arbitrary number of hydrometeors, determined by the "hydrotable" optical property files (replaces old Mietable files).*

iii. *Can optionally specify per hydrometeor cloud fractions, instead of a single cloud fraction for all hydrometeors in a level.*
iv. *New option to approximate V-/H-pol differences due to oriented particles.*
v. *It can now support active microwave sensors (e.g. CLOUDSAT)*

This report refers to the version 13.0 of RTTOV. Higher number versions of RTTOV v13 will contain updated science and technical developments issued approximately once a year. These will be documented in the RTTOV v14 science and validation report but the interim release notes will include some details of any changes. There may be updates to this document which will be posted on the NWP SAF web site so check the version number in the header.

6. Acknowledgements

The RTTOV-13 developments and validation described here were carried out as part of the EUMETSAT funded NWP-SAF activities by the Met Office, ECMWF, DWD and MétéoFrance. In addition contributions from several scientists, visiting and associate scientists are gratefully acknowledged.

7 References

Baordo, F. and Geer, A.J., 2016. Assimilation of SSMIS humidity-sounding channels in all-sky conditions over land using a dynamic emissivity retrieval. *Q.J.R. Meteorol. Soc*., **142**, 2854-2866.

Baran, A. J., Cotton, R., Furtado, K., Havemann, S., Labonnote, L.-C., Marenco, F., Smith, A. and Thelen, J.-C. 2014 A self-consistent scattering model for cirrus. II: The high and low frequencies. *Q.J.Roy. Meteorol. Soc.,* **140**: 1039–1057. doi:10.1002/qj.2193

Barbosa-Silveira, B., Turner, E., Vidot, J., Roquet, P., Guidard, V., Saunders, R., 2020 D311c_Lot1.4.3.2: Evaluation of fast model parametrization: Validation of the RTTOV coefficients, *ECMWF Copernicus Report, C3S*.

Barlakas, V., Geer A. J., Eriksson, P., 2020 Introducing hydrometeor orientation into all-sky millimeter/sub-millimeter assimilation. *To be submitted to Atmospheric Measurement Techniques*

Bauer, P., Moreau, E., Chevallier, F. and O'keeffe, U., 2006. Multiple-scattering microwave radiative transfer for data assimilation applications. *Q.J.R. Meteorol. Soc*., **132**(617) 1259-1281.

Baum, B. A., P. Yang, A. J. Heymsfield, C. Schmitt, Y. Xie, A. Bansemer, Y. X. Hu, and Z. Zhang, 2011. Improvements to shortwave bulk scattering and absorption models for the remote sensing of ice clouds. *J. Appl. Meteor. Clim.,* **50**, 1037-1056.

Borbas, E. E. and B. C. Ruston, 2010 The RTTOV UWiremis IR land surface emissivity module. *NWP SAF report. https://nwp-saf.eumetsat.int/publications/vs_reports/nwpsaf-mo-vs-042.pdf*

Borbas, E.E.; Hulley, G.; Feltz, M.; Knuteson, R.; Hook, S. 2018 The Combined ASTER MODIS Emissivity over Land (CAMEL) Part 1: Methodology and High Spectral Resolution Application. *Remote Sens*., **10**, 643 https://doi.org/10.3390/rs10040643

Borbas E. and M Feltz 2019 Updating the CAMEL surface emissivity atlas for RTTOV. *Report of Visiting Scientist mission NWP_AS18_01, Document NWPSAF-MO-VS-058, Version 1.0, 18-01-19, https://nwp-saf.eumetsat.int/publications/vs_reports/nwpsaf-mo-vs-058.pdf*

Bozzo, A., Benedetti, A., Flemming, J., Kipling, Z., Remy, S., 2020: An aerosol climatology for global models based on the tropospheric aerosol scheme in the Integrated Forecasting System of ECMWF, *Geosci. Model Dev*., **13**(3), 1007–1034 doi:10.5194/gmd-13-1007-2020

Bucholtz, A., 1995: Rayleigh-scattering calculations for the terrestrial atmosphere, *Appl. Optics*, **34**, 2765–2773.

Chevallier, F. Di Michele, S. McNally, A.P. 2006 Diverse profile datasets from the ECMWF 91-level short-range forecasts, *NWP SAF Technical Report* https://www.ecmwf.int/node/8685

Duncan, D.I., Turner, E., Weston, P., Bormann, N., Faulwetter, R., Kopken-Watts, C. 2019 Evaluation of using measured SRFs in the radiative transfer for microwave sounders at ECMWF, UK Met Office, and DWD, *Poster at the 22nd International TOVS Study Conference (ITSC-22), Saint.Sauveur, Canada* http://cimss.ssec.wisc.edu/itwg/itsc/itsc22/posters/2p.09.duncan.pdf

Duruisseau F., Chambon P., Faure G., and Geer A. 2018 Development of an active sensor module for the RTTOV/SCATT radiative transfer simulator. *8th International Precipitation Working Group meeting, Séoul, Corée du Sud*. 5-10 November 2018

Elfouhaily, T., Chapron, B., Katsaros, K., and Vandemark, D., 1997 A unified directional spectrum for long and short wind-driven waves, *J. Geophys. Res.,* **102**(C7), 15781-15796, doi:10.1029/97JC00467.

Emde C., R. Buras-Schnell, A. Kylling, B. Mayer, J. Gasteiger, U. Hamann, J. Kylling, B. Richter, C. Pause, T. Dowling, and L. Bugliaro, 2016 The libradtran software package for radiative transfer calculations (version 2.0.1). *Geoscientific Model Development*, **9**(5):1647-1672.

Eresmaa, R. and McNally, A. P. 2014 Diverse profile datasets from the ECMWF 137-level short-range forecasts, *NWP SAF Tech. Report* https://nwp-saf.eumetsat.int/oldsite/reports/nwpsaf-ec-tr-017.pdf

Eriksson, P., Ekelund, R., Mendrok, J., Brath, M., Lemke, O. and Buehler, S.A., 2018 A general database of hydrometeor single scattering properties at microwave and sub-millimetre wavelengths. *Earth System Science Data*, **10**(3), 1301-1326.

Eyre J.R. and H.M. Woolf 1988 Transmittance of atmospheric gases in the microwave region: a fast model. *Applied Optics* **27** 3244-3249.

Eyre J.R. 1991 A fast radiative transfer model for satellite sounding systems. *ECMWF Research Dept. Tech. Memo.* 176 Available at http://www.ecmwf.int/publications/library/ecpublications/_pdf/tm/001-300/tm176.pdf

Faure, G., Chambon, P., Brousseau, P. 2020 Operational implementation of the AROME model in the Tropics: multiscale validation of rainfall forecasts. Weather and Forecasting. https://doi.org/10.1175/WAF-D-19-0204.1

Feltz, M., Borbas, E., Knuteson, R., Hulley, G. and Hook, S. 2018 The Combined ASTER MODIS Emissivity over Land (CAMEL) Part 2: Uncertainty and Validation. *Remote Sens*., **10**, 664. https://doi.org/10.3390/rs10050664

Field, P.R., Heymsfield, A.J. and Bansemer, A., 2007 Snow size distribution parameterization for midlatitude and tropical ice clouds. *J. Atmos. Sci*., **64**(12), 4346-4365.

Geer, A.J. and Baordo, F., 2014 Improved scattering radiative transfer for frozen hydrometeors at microwave frequencies. *Atmos. Meas. Tech*., **7**(6), 1839-1860.

Geer, A.J. and co-authors, 2020 Hydrometeor optical properties for RTTOV v13.1. *To be submitted to Geophysical Model Development*

Geer, A.J., 2020 Physical characteristics of frozen hydrometeors inferred with parameter estimation. *To be submitted to Atmos. Meas. Tech.*

Gong, J. and Wu, D.L., 2017 Microphysical properties of frozen particles inferred from Global Precipitation Measurement (GPM) Microwave Imager (GMI) polarimetric measurements. *Atmospheric Chemistry and Physics*, **17**(4), 2741-2757.

Guedj, S., F. Karbou, F. Rabier and A. Bouchard, 2010 Toward a Better Modeling of Surface Emissivity to Improve AMSU Data Assimilation Over Antarctica. *IEEE Transactions on Geoscience and Remote Sensing*, **48**, no. 4, 1976-1985, doi: 10.1109/TGRS.2009.2036254.

Hale, G. M. and M. R. Querry, 1973 Optical constants of water in the 200nm to 200µm wavelength region, *Appl. Opt.* **12**, 555-563.

Hasselmann, K. et al. 1973 Measurements of wind-wave growth and swell during the Joint North Sea Wave Project (JONSWAP) *Deutsch. Hydrogr. Z*., **12**, 95 pp.

Hess, M., P. Koepke, and I. Schult 1998 Optical Properties of Aerosols and Clouds: The Software Package OPAC. *Bull. Amer. Meteor. Soc.,* **79**, 831–844, doi:10.1175/1520-0477(1998)079<0831:OPOAAC>2.0.CO;2

Heymsfield, A.J., Schmitt, C. and Bansemer, A., 2013 Ice cloud particle size distributions and pressure-dependent terminal velocities from in situ observations at temperatures from 0° to− 86° C. *J. Atmos. Sci*., **70**(12), 4123-4154.

Hocking, J., 2016: A visible/infrared multiple scattering model for RTTOV, *NWP SAF Tech Report*, available at: https://nwp-saf.eumetsat.int/publications/tech_reports/nwpsaf-mo-tr-031.pdf (last access: 28 May 2020).

Hocking, J. 2021: A new gas absorption optical depth parameterisation for RTTOV v13. *To be submitted to Geoscientific Model Development.*

Liebe, H. J. 1989 MPM—an atmospheric millimetre wave propagation model. *Int. J. Infrared and Millimetre Waves.*, **10**, 631–650.

Liu, G., 2008 A database of microwave single-scattering properties for non-spherical ice particles. *Bulletin of the American Meteorological Society*, **89**(10), 1563-1570.

Lonitz, K., and A. Geer, 2018 Assessing the impact of different liquid water permittivity models on the fit between model and observations. *Atmos. Meas. Tech*., **12**, 405–429. https://doi.org/10.5194/amt-12-405-2019

Martin, G.M., D.W. Johnson, and A. Spice, 1994 The Measurement and Parameterization of Effective Radius of Droplets in Warm Stratocumulus Clouds. *J. Atmos. Sci*., **51**, 13, 1823-1842, https://doi.org/10.1175/1520-0469(1994)051<1823:TMAPOE>2.0.CO;2

Matricardi, M. 2003 RTIASI-4 A new version of the ECMWF fast radiative transfer model for the infrared atmospheric sounding interferometer. *ECMWF Research Dept. Tech. Memo. 425. https://www.ecmwf.int/sites/default/files/elibrary/2003/11039-rtiasi-4-new-version-ecmwf-fast-radiative-transfer-model-infrared-atmospheric-sounding.pdf*

Matricardi, M., Chevallier F, Kelly G, Thepaut J-N 2004 An improved general fast radiative transfer model for the assimilation of radiance observations. *Q. J. Roy. Meteorol. Soc.* **130** 153-173

Matricardi M. 2008 The generation of RTTOV regression coefficients for IASI and AIRS using a new profile training set and a new line-by-line database. *ECMWF Research Dept Tech. Memo. 564. https://www.ecmwf.int/sites/default/files/elibrary/2008/11040-generation-rttov-regression-coefficients-iasi-and-airs-using-new-profile-training-set-and-new.pdf*

Matricardi M. 2010 A principal component based version of the RTTOV fast radiative transfer model. *Q. J. Roy. Meteorol. Soc.* **136** 1823-1835.

Matzler, C. 2005 On the determination of surface emissivity from satellite observations. *Geoscience and Remote Sensing Letters*, **2**, 160-163.

Mayer, B. and Kylling, A., 2005 Technical note: the libRadtran software package for radiative transfer calculations — description and examples of use. *Atmos. Chem. Phys*., **5**, 1855–77.

McFarquhar, G.M. and Heymsfield, A.J., 1997 Parameterization of tropical cirrus ice crystal size distributions and implications for radiative transfer: Results from CEPEX. *J. Atmos. Sci*. **54**(17), 2187-2200.

McMillin, L. M. and Fleming, H. E., 1976 Atmospheric transmittance of an absorbing gas: a computationally fast and accurate transmittance model for absorbing gases with constant mixing ratios in inhomogeneous atmospheres, *Appl. Optics*, **15**, 358–363.

McMillin, L. M., Crone, L. J., and Kleespies, T. J., 1995 Atmospheric transmittance of an absorbing gas. 5. Improvements to the OPTRAN approach, *Appl. Optics*, **34**, 8396–8399.

McMillin, L. M., Xiong, X., Han, Y., Kleespies, T. J., and Delst, P. V., 2006 Atmospheric transmittance of an absorbing gas. 7. Further improvements to the OPTRAN 6 approach, *Appl. Optics,* **45**, 2028–2034, https://doi.org/10.1364/AO.45.002028.

Plant, W., 1982: A relationship between wind stress and wave slope. *J. Geophys. Res*., **87**(C3), 1961-1967.

R10REP2010 RTTOV-10 science and validation report available at:
http://nwpsaf.eu/oldsite/deliverables/rtm/docs_rttov10/rttov10_svr_1.11.pdf

R11REP2013 RTTOV-11 science and validation report available at:
https://nwpsaf.eu/oldsite/deliverables/rtm/docs_rttov11/rttov11_svr.pdf

R12REP2017 RTTOV-12 science and validation report available at:
https://nwpsaf.eu/oldsite/deliverables/rtm/docs_rttov12/rttov12_svr.pdf

R7REP2002 RTTOV-7 science and validation report available at:
http://nwpsaf.eu/oldsite/deliverables/rtm/rttov7_svr.pdf

R8REP2006 RTTOV-8 science and validation report available at:
http://nwpsaf.eu/oldsite/deliverables/rtm/rttov8_svr.pdf

R9REP2008 RTTOV-9 science and validation report available at:
http://nwpsaf.eu/oldsite/deliverables/rtm/rttov9_files/rttov9_svr.pdf

Rosenkranz, P.W., 2015 A Model for the Complex Dielectric Constant of Supercooled Liquid Water at Microwave Frequencies*. IEEE Trans. on Geosci. and Remote Sensing*, **53**, 3, 1387-1393.

Saunders R.W., M. Matricardi and P. Brunel 1999a A fast radiative transfer model for assimilation of satellite radiance observations - RTTOV-5. *ECMWF Research Dept. Tech. Memo. 282* (available from https://www.ecmwf.int/sites/default/files/elibrary/1999/12107-fast-radiative-transfer-model-assimilation-satellite-radiance-observations-rttov-5.pdf).

Saunders R.W., M. Matricardi and P. Brunel 1999b An Improved Fast Radiative Transfer Model for Assimilation of Satellite Radiance Observations. *Q. J. Roy. Meteorol. Soc.* , **125**, 1407-1425.

Saunders, R., Hocking, J., Turner, E., Rayer, P., Rundle, D., Brunel, P., Vidot, J., Roquet, P., Matricardi, M., Geer, A., Bormann, N., and Lupu, C. 2018 An update on the RTTOV fast radiative transfer model (currently at version 12), *Geosci. Model Dev*., **11**, 2717–2737, https://doi.org/10.5194/gmd-11-2717-2018.

Scheck, L., 2016 Comparison of MFASIS and RTTOV-DOM, *NWP SAF Report*, available at: https://nwp-saf.eumetsat.int/publications/vs_reports/nwpsaf-mo-vs-054.pdf (last access: 28 May 2020).

Scheck, L., Frerebeau, P., Buras-Schnell-R., Mayer, B., 2016 A fast radiative transfer method for the simulation of visible satellite imagery, *J. Quant. Spec. Rad. Transfer*, **175**, 54-67.

Scheck, L., M. Weissmann, and B. Mayer, 2018 Efficient Methods to Account for Cloud-Top Inclination and Cloud Overlap in Synthetic Visible Satellite Images. *J. Atmos. Oceanic Technol.*, **35**, 665–685, https://doi.org/10.1175/JTECH-D-17-0057.1.

Scheck, L, Weissmann, M, Bach, L. 2020 Assimilating visible satellite images for convective-scale numerical weather prediction: A case-study. *Q. J. Roy. Meteorol. Soc*. 1– 22. https://doi.org/10.1002/qj.3840

Segelstein, D., 1981 The Complex Refractive Index of Water. Masters Thesis, Dept Physics, U. Missouri-Kansas City.

Strow, L. L., Hannon, S. E., De Souza-Machado, S., Motteler, H. E., & Tobin, D. 2003 An overview of the AIRS radiative transfer model. *IEEE Transactions on Geoscience and Remote Sensing*, **41**(2), 303–313.

Tiesinga, E., Mohr, P. J., Newell, D. B., and Taylor, B. N., 2019 The 2018 CODATA Recommended Values of the Fundamental Physical Constants (Web Version 8.0). http://physics.nist.gov/constants [last accessed: 30/06/2020]

Tretyakov M. Yu., Koshelev M.A., Dorovskikh V.V., Makarov D.S. and Rosenkranz P.W. 2005 60 GHz oxygen band: precise broadening and central frequencies of fine structure lines, absolute absorption profile at atmospheric pressure, and revision of mixing coefficients. *J. Mol. Spectrosc*. **231**, 1-14.

Turner, D.D., Kneifel, S., and Cadeddu, M.P. 2016 An Improved Liquid Water Absorption Model at Microwave Frequencies for Supercooled Liquid Water Clouds*. J. Atmos. Oceanic Tech*., **33**, 33-44, doi: 10.1175/JTECH-D-15-0074.1

Turner, E., Rayer, P., Saunders, R., 2019a AMSUTRAN: A microwave transmittance code for satellite remote sensing*, J. Quant. Spectrosc. and Rad. Transfer*, **227**, 117-129, ISSN 0022-4073

Turner E. and Saunders, R., 2019b Sub-millimetre Spectroscopy for AMSUTRAN. Part One: The Theoretical Basis*, Technical Report NWPSAF-MO-TR-038*, https://nwp-saf.eumetsat.int/site/cdop3-reports-publications/

Vidot, J., & Borbás, É. 2014 Land surface VIS/NIR BRDF atlas for RTTOV-11: model and validation against SEVIRI land SAF albedo product. *Quart. J. Roy. Meteorol. Soc*. **140**. 10.1002/qj.2288.

Vidot, J., A. J. Baran, and P. Brunel 2015 A new ice cloud parameterization for infrared radiative transfer simulation of cloudy radiances: Evaluation and optimization with IIR observations and ice

cloud profile retrieval products. *J. Geophys. Res. Atmos*., **120**, 6937–6951. doi: 10.1002/2015JD023462.

Woodward, S., 2001 Modeling the atmospheric life cycle and radiative impact of mineral dust in the Hadley Centre climate model, *J. Geophys. Res.*, **106**(D16), 18155-18166, doi:10.1029/2000JD900795.Yoshimori, K., K. Itoh and Y. Ichioka, 1995 Optical characteristics of a wind-roughened water surface: a two-dimensional theory. *Applied Optics*, **34**, 27, 6236-6247.

End of Report